



ANALYSIS THROUGH EQE AND STM OF ORGANIC SOLAR CELLS, BASED ON PTB7, PTB7-Th AND PBDB-T DONORS



Thesis dissertation submitted to earn the degree:

DOCTOR OF SCIENCE (OPTICS)

Advisor: Dr. José-Luis Maldonado-Rivera

Student: M.Sc. Olivia Amargós-Reyes

December 2019

León, Guanajuato,

México

Abstract

In the present thesis, external quantum efficiency (EQE or IPCE) technique was implemented. This home-made set up was used as a complementary characterization to better understand solar cell performance and to find optimal fabrication conditions. Organic photovoltaic solar cells (OPVs) were fabricated using commercial electron-donor polymers PTB7, PTB7-Th and PBDB-T, and electron-acceptors PC₇₁BM, ITIC and FeS₂, and by means of scanning tunneling microscopy (STM), donor film molecular ordering was analyzed. These measurements indicate that PTB7-Th film chains are somewhat thicker and less spaced than those in PTB7 based OPVs, which could possibly provide better electrical charge transport. Besides, PBDB-T, with a shorter distance between polymer backbone chains, could facilitate a more efficient intramolecular charge separation, and thus improve charge transfer from the active layer to the OPV electrodes. For PTB7 based OPVs, non-toxic iron sulfide (FeS₂) nanocrystals (NCs) were added to the active layer at different weight ratios as a second electron-acceptor, achieving an increase in power conversion efficiency (PCE) of 21%. For PTB7-Th based OPVs (best achieved PCE was 7.65%), optical-electrical analyses were carried out using EQE and internal quantum efficiency (IQE), applying active layer thickness variation (from 40 to 165 nm) by means of the transfer matrix method (TMM). Our results show a significant reduction of IQE (when increasing the active layer thickness above 120 nm), and consequently, also of EQE and PCE, mainly due to the reduction in charge carrier collection probability. A comparison between the experimental measurements and theoretical simulations was discussed in order to have better understanding of the OPVs performance. Finally, PBDB-T:ITIC based OPVs were tested with different hole transport layers (HTLs): PEDOT:PSS, fluorinated reduced graphene oxide (F-rGO)/PEDOT:PSS and just F-rGO. With F-rGO/PEDOT:PSS and PEDOT:PSS as HTLs, average PCEs of 8.3% and 8.7% were achieved, respectively (the highest efficiency reached with PEDOT:PSS was 8.9%), and with F-rGO, efficiency decayed to 5.4%. Device stability maintained a similar trend with the use of either F-rGO/PEDOT:PSS or PEDOT:PSS; however, for the F-rGO case, stability showed a faster decay.

Acknowledgements

First, I want to express special thanks to my advisor, Dr. José Luis Maldonado, for his patience, guidance, help and support during my four years of doctoral studies; thank you for encouraging me to become a better professional.

I am also very grateful to my doctoral committee members, Dr. Oracio Barbosa, Dr. Norberto Arzate, Dr. Bernardo Frontana and Dra. Ma. Concepción Arenas, for all their comments, which contributed to the improvement of my work and to the earning of my PhD.

Additionally, I would like to thank Mexico for receiving me and making me feel part of the country, and Centro de Investigaciones en Óptica (CIO) and Grupo de Propiedades Ópticas de la Materia (GPOM) for giving me all that I needed to conduct my research work. I also want to thank CONACYT-SENER for granting me a doctoral scholarship, as well as express my appreciation for all the financial support received through CeMIE-Sol 207450/27 (Mexico), CONACyT-SENER Grant 245754 (Mexico), B-S-69369 (Mexico-England Bilateral Grant) and CONACyT Grants 2017 (281164), 2018 (293371) and 2019 (299124) “Laboratorio Nacional de Materiales Grafénicos (LNMG)”, which allowed me to participate in national and international conferences and to complete my work towards earning the PhD.

I acknowledge the help and technical assistance that Martin Olmos gave me, and the technical support that Christian Albor supplied in conducting SEM and XRD measurements.

I thank all the GPOM members, particularly my friends, with whom I shared most of the time these years: Irving, Luis, Álvaro, Nicasio, Denisse, Diana, Yaily and Wilson, as well as Mario Rodriguez, PhD, and Antonio Meneses, PhD; I thank them for being patient, as well as for teaching me lots of things and helping me understand many others. I am very proud to have worked with all of you as a team.

I want to thank my advisor, CIO and Helmholtz Institute at Friedrich-Alexander University Erlangen-Nuremberg (Germany) for giving me the opportunity to do an international research stay and to have a great professional and personal experience.

Finally, but not less important, I would like to thank my family with all my heart, specially my father Alberto and my mother Elena, who have always supported my decisions and helped me to

achieve the goals that I set for myself in life; my husband and my new family, for all their support, always giving me love and good words when I needed them, and encouraging me to move on and grow up; my Cuban and Mexican friends, especially Jeni, Lorena, Zoe and Luisa, who I thank for helping me to be a better version of myself, and for always being with me in good and bad times. Without all of you, this journey would have been much more complicated, and maybe not even possible.

Contents

<i>Abstract</i>	i
<i>Acknowledgements</i>	ii
1. Introduction	1
2. Organic solar cells	5
2.1. Organic semiconductors	5
2.2. Architecture	7
2.3. Working principle	9
2.4. Fabrication	13
2.5. Characterization techniques	15
2.5.1. Complementary characterization techniques	17
3. External Quantum Efficiency	19
3.1. Set up	20
3.2. Transfer Matrix Method (TMM)	24
3.3. Internal Quantum Efficiency (IQE)	28
4. Device fabrication and experimental results	30
4.1. Donor polymers comparisons: PTB7, PTB7-Th and PBDB-T	31
4.2. PTB7: Iron sulfide nanocrystals as second electron-acceptor	37
4.3. PTB7-Th: Active layer thickness variation analysis	51
4.4. PBDB-T: F-rGO as an alternative hole transport layer	66
5. Conclusions	74
Appendix A	76
Scientific publications	78
References	80

List of Figures

Figure 1.1: Estimated distribution of energy sources of total energy consumption in 2016 [1].	1
Figure 1.2: Global renewable power capacity from 2007 to 2017 [1].	2
Figure 1.3: Solar PV Global Capacity by Country from 2007 to 2017 [1].	3
Figure 1.4: Best research cell efficiencies from 1976 to 2019 [12].	4
Figure 2.1: OPV (a) direct and (b) inverse configuration.	8
Figure 2.2: Chemical structures of two of the materials used as HTL (PEDOT:PSS) and ETL (PFN).	8
Figure 2.3: OPV (a) bi-layer, (b) heterojunction and (c) tandem structure in direct configuration.	9
Figure 2.4: Light absorption and exciton generation.	10
Figure 2.5: Exciton dissociation.	11
Figure 2.6: Charges transport.	11
Figure 2.7: Charges collection.	12
Figure 2.8: J-V curve of a solar cell (with light->blue, in dark->green), with the main OPV parameters.	16
Figure 3.1: EQE experimental set up: (a) initial arrangement for light power measurements, (b) arrangement for OPV current determinations.	20
Figure 3.2: Light intensity measured from the monochromator output in order to observe the second diffraction order at different wavelengths (730, 750 and 760 nm).	22
Figure 3.3: EQE measurements (a) for the same OPV cell, (b) with standard deviation. Highest standard deviation is 2.3 %; measurements are 97.7 % reliable.	22
Figure 3.4: (a) J-V and (b) EQE measurements for five different OPVs, and (c) EQE measurements with standard deviation. Highest standard deviation (reproducibility error) is 6.6 %; reliable reproducibility is 93.4 %.	23
Figure 3.5: Bandwidth monochromator curve at 550 nm, FWHM of 4 nm.	24
Figure 3.6: EQE homemade arrangement images.	24
Figure 3.7: OPV cell stack consideration for TMM.	25
Figure 3.8: Refractive index (black line) and extinction coefficient (blue line) of PTB7-Th:PC ₇₁ BM blend film.	28
Figure 4.1: PTB7, PTB7-Th and PBDB-T absorption spectra in solution.	32
Figure 4.2: AFM topography (top, traditional color map) and phase contrast (bottom, spectral color map) images of (a) PTB7, (b) PTB7-Th, (c) PBDB-T, (d) PTB7:PC ₇₁ BM with DIO, (e) PTB7-Th:PC ₇₁ BM with DIO, (f) PBDB-T:ITIC with DIO. For all cases, bar scale = 1 μm. As surface is relatively smooth, spectral color map provides better details.	34
Figure 4.3: STM images showing worm-like chains of (a) PTB7 and (b) PTB7-Th with 6 nm × 6 nm scan size, (c) PBDB-T with 5 nm × 5 nm scan size, (d) PTB7 with 38 nm × 38 nm scan size, (e) PTB7-Th with 40 nm × 40 nm scan size and (f) PBDB-T with 20 nm × 20 nm scan size.	35
Figure 4.4: (a) XRD pattern of PTB7 (black line), PTB7-Th (red line) and PBDB-T (blue line) films, (b), (c) and (d) SEM images for PTB7:PC ₇₁ BM, PTB7-Th:PC ₇₁ BM and PBDB-T:ITIC films, respectively; surface is relatively smooth.	37
Figure 4.5: (a) OPV structure; (b) Chemical structure of PC ₇₁ BM.	38
Figure 4.6: (a) and (b) TEM morphology of FeS ₂ NCs at 50 and 100 nm scale bar, respectively and, (c) distribution of NCs sizes.	41
Figure 4.7: (a) STM image of FeS ₂ deposited on HOPG substrate (thickness ~ 20 nm) with 50 nm × 50 nm scan size and (b) SEM image of FeS ₂ NCs (scale bar = 100 nm).	41

Figure 4.8: (a) Cyclic voltammograms of ITO (reference, black) and FeS ₂ NCs in acetonitrile with TBAPF ₆ 0.1 M at 100 mV s ⁻¹ (Blue: Anodic zone, Red: Cathodic zone), (b) Flat energy levels diagram of the used organic materials as well as FeS ₂ for OPVs fabrication [16].....	43
Figure 4.9: UV-Vis absorption of the blend PTB7:PC ₇₁ BM with different FeS ₂ concentrations: 0.0 wt. %, 0.25 wt. %, 0.5 wt. %, 1.0 wt. %.....	43
Figure 4.10: (a) J-V curves and (b) EQE of PTB7:PC ₇₁ BM based devices with different concentrations of FeS ₂ : 0.0 wt. %, 0.25 wt. %, 0.5 wt. %, 1.0 wt. %.....	44
Figure 4.11: AFM images in non-contact mode in 2D (left) and 3D (right) of OPVs with different concentrations of FeS ₂ : (a) 0.0 wt. %, (b) 0.25 wt. %, (c) 0.5 wt. % and (d) 1.0 wt. %.....	46
Figure 4.12: SEM image of OPVs layers (ITO ~197 nm; PEDOT:PSS ~40 nm; PTB7:PC ₇₁ BM ~113 nm) and an active layer zoom with non-NCs.....	46
Figure 4.13: SEM images (at 15 kV) of OPVs active layer with different concentrations of FeS ₂ : (a) 0.0 wt. %, (b) 0.25 wt. %, (c) 0.5 wt. % and (d) 1.0 wt. %; (e) image of PEDOT:PSS at a lower SEM voltage (1kV). Scale bar = 1 μm.....	48
Figure 4.14: Impedance spectroscopy measurements (filled color squares) and simulations (black lines) of a) PTB7:PC ₇₁ BM and b) PTB7:PC ₇₁ BM:FeS ₂ (with 0.5 wt. % of FeS ₂); c) Equivalent circuit used for IS simulations; d) R _{rec} values vs bias voltage for PTB7:PC ₇₁ BM (blue) and PTB7:PC ₇₁ BM:FeS ₂ (with 0.5 wt. % of FeS ₂) (red).....	49
Figure 4.15: Electrical parameters of OPVs as a function of FeS ₂ NCs content. Three different sets and at least three devices for each concentration were tested.....	50
Figure 4.16: Architecture of the fabricated OPVs cells. See chemical structures in page x, before Introduction section.....	52
Figure 4.17: Best J-V curves and achieved efficiencies for PTB7:PC ₇₁ BM (blue curve) and PTB7-Th:PC ₇₁ BM (red curve) based OPVs devices by using the FM alternative top electrode vacuum-free deposited. OPVs performance is somewhat better for those based on PTB7-Th polymer.....	53
Figure 4.18: Current-density vs voltage (J-V) curves of PTB7-Th based OPVs devices with active layer thicknesses from (a) 40 to 92 nm, and (b) 100 to 165 nm. EQE vs wavelength of devices with active layer thicknesses from (c) 40 to 92 nm, and (d) 100 to 165 nm. For each thickness, at least three OPVs samples were fabricated and tested, they followed a similar trend.....	54
Figure 4.19: (a) PCE (filled squares), J _{sc} (filled circles), (b) V _{oc} (open squares), and FF (open circles) as a function of the active layer thickness.....	56
Figure 4.20: (a) EQE values at 500, 580 and 730 nm as a function of the active layer thickness, (b) J _{sc} determined from J-V curves (black squares) and J _{sc} estimated from EQE measurements (blue squares) versus active layer thickness.....	56
Figure 4.21: Absorbance of ITO, PEDOT:PSS and PTB7-Th:PC ₇₁ BM layers (a) experimentally determined (for each single layer), (b) calculated through TMM (for each single layer), and (c) determined through TMM (with all the cell structure, where light cross the films twice because of the reflection at the top electrode and also there are other reflections contributions because of the films interfaces). Film thicknesses: 165, 40 and 100 nm for ITO, PEDOT:PSS and PTB7-Th:PC ₇₁ BM layers, respectively.....	58
Figure 4.22: Optical electric field intensity (black color = zero intensity, yellow = maximum value estimated by TMM considering a unitary incoming intensity (light arriving from the bottom side)) passing through these layer thicknesses: 165 nm of ITO, 40 nm of PEDOT:PSS, 100 nm of PTB7-Th:PC ₇₁ BM and 5 nm of PFN.....	59

Figure 4.23: Optical electric field intensity calculated by TMM considering a unitary incoming intensity (incident from the left) for (a) 500 nm (blue line) and 730 nm (red line) light wave for an active layer thickness of 100 nm, (b) 500 nm light wave for all active layer thicknesses (from 40 to 165 nm, OPV position means from 205 nm to 370 nm for the thicker active layer). The showed electric field is the result from reflection and interference processes that occur inside the OPV cell stack.	60
Figure 4.24: PTB7-Th:PC ₇₁ BM absorbance for each active layer thickness determined by TMM: (a) when just the active film is deposited on glass substrate; (b) with the complete cell configuration.	62
Figure 4.25: Active layer absorbance (by taking into account all the OPV layers) vs thickness obtained with TMM for three different wavelengths: 500, 580 and 730 nm.....	62
Figure 4.26: Internal Quantum Efficiency (IQE) obtained from EQE and the PTB7-Th:PC ₇₁ BM absorbance (from TMM) (a) from 40 to 92 nm thickness; (b) from 100 to 165 nm thickness; (c) IQE versus active layer thickness for three different wavelengths: 500, 580 and 730 nm.	63
Figure 4.27: (a) UV-Vis absorption spectrum of PBDB-T:PC ₇₁ BM (blue) and PBDB-T:ITIC (red) and (b) J-V curves of ITO/PEDOT:PSS/PBDB-T:PC ₇₁ BM(blue) or PBDB-T:ITIC(red)/PFN/FM.	66
Figure 4.28: (a) chemical structures of ITIC and F-rGO, (b) architecture of OPV devices.	68
Figure 4.29: UV-Vis absorption spectra of (a) the HTLs used (PEDOT:PSS, F-rGO/PEDOT:PSS and F-rGO) and (b) PBDB-T:ITIC active layer over the different HTLs.	69
Figure 4.30: Best J-V curve (from series of at least five devices each) and achieved efficiency for PBDB-T:ITIC based OPVs devices using the FM alternative top electrode vacuum-free deposited.	70
Figure 4.31: (a) Best J-V curves and achieved efficiencies and (b) EQE curves for PBDB-T:ITIC based OPVs devices with the different HTLs (PEDOT:PSS, F-rGO/PEDOT:PSS and F-rGO).	71
Figure 4.32: SEM images (at 1 kV) of a) ITO, b) ITO/F-rGO, c) ITO/PEDOT:PSS and d) ITO/F-rGO/PEDOT:PSS. Scale bar = 100 nm.	72
Figure 4.33: Stability of OPVs normalized parameters: (a) power conversion efficiency, (b) voltage, (c) current density and (d) fill factor, for the three HTLs (PEDOT:PSS red, F-rGO/PEDOT:PSS blue and F-rGO black) under ISOS-D1 testing protocol. The average values and error bars were calculated from three devices for each case.....	73

List of Tables

Table 4.1: Comparative data of the PTB7, PTB7-Th and PBDB-T donor polymers	33
Table 4.2: Average PV parameters of OPVs sets (n=3) with different FeS ₂ content in the active layer. For PCE, numbers in parentheses are the best values and standard deviations are also shown.....	45
Table 4.3: Parameters of the equivalent circuit used to simulate experimental IS data for PTB7:PC ₇₁ BM and PTB7:PC ₇₁ BM:FeS ₂ (with 0.5 wt. % of FeS ₂) based solar cells.	50
Table 4.4: PV parameters at different active layer thicknesses. For each thickness, at least three OPVs samples were fabricated and tested, they followed a similar trend. OPVs configuration: glass/ITO/PEDOT:PSS/PTB7-Th:PC ₇₁ BM/PFN/FM. Standard deviation is included for the PCE values.	55
Table 4.5: Current density values from J-V curve vs the estimated ones from EQE. OPVs configuration: glass/ITO/PEDOT:PSS/PTB7-Th:PC ₇₁ BM/PFN/FM	57
Table 4.6: IQE values at 470 (around maximum IQE, for an active layer thickness in the range 92-120 nm), 500, 580 and 730 nm. OPVs configuration: glass/ITO/PEDOT:PSS/PTB7-Th:PC ₇₁ BM/PFN/FM ..	64
Table 4.7: PV average parameters of the fabricated devices. For PCE, numbers in parenthesis are the best values. OPVs configuration: glass/ITO/HTL/PBDB-T:ITIC/PFN/FM.	72

List of Abbreviations

PV Photovoltaics

OPVs Organic Photovoltaics solar cells

NREL National Renewable Energy Laboratory

HOMO High Occupied Molecular Orbital

LUMO Low Unoccupied Molecular Orbital

CCs Charge Carriers

BHJ Bulk Heterojunction

HTL Hole Transport Layer

ETL Electron Transport Layer

PCE Power Conversion Efficiency

AM1.5 AirMass 1.5

FF Fill Factor

FM Field's Metal

EQE External Quantum Efficiency

IPCE Incident Photon to Current Efficiency

IQE Internal Quantum Efficiency

TMM Transfer Matrix Method

AFM Atomic Force Microscopy

STM Scanning Tunneling Microscopy

SEM Scanning Electron Microscopy

XRD X-Ray Diffraction

NCs Nano-crystals

NPs Nanoparticles

J_{sc} Short-circuit current (mA/cm^2)

V_{oc} Open-circuit voltage (*V*)

PCE Power conversion efficiency (%)

EQE External quantum efficiency (%)

IQE Internal quantum efficiency (%)

λ Wavelength (*nm*)

R_s Series resistance (Ωcm^2)

R_p Shunt resistance (Ωcm^2)

List of Materials

PEDOT:PSS: Poly(3,4-ethyl-enedioxythiophene) polystyrene sulfonate.

PTB7 or PC9: Poly[[4,8-bis[(2-ethylhexyl)oxy]benzo[1,2-b:4,5-b']dithiophene-2,6-diyl][3-fluoro-2-[(2-ethylhexyl)carbonyl]thieno[3,4-b]thiophenediyl]].

PTB7-Th or PCE10 (PBDTTT-EFT): Poly[(ethylhexyl-thiophenyl)-benzodithiophene-(ethylhexyl)-thienothiophene].

PBDB-T or PCE12: Poly[[4,8-bis[5-(2-ethylhexyl)-2-thienyl]benzo[1,2-b:4,5-b']dithiophene-2,6-diyl]-2,5-thiophenediyl[5,7-bis(2-ethylhexyl)-4,8-dioxo-4H,8H-benzo[1,2-c:4,5-c']dithiophene-1,3-diyl]].

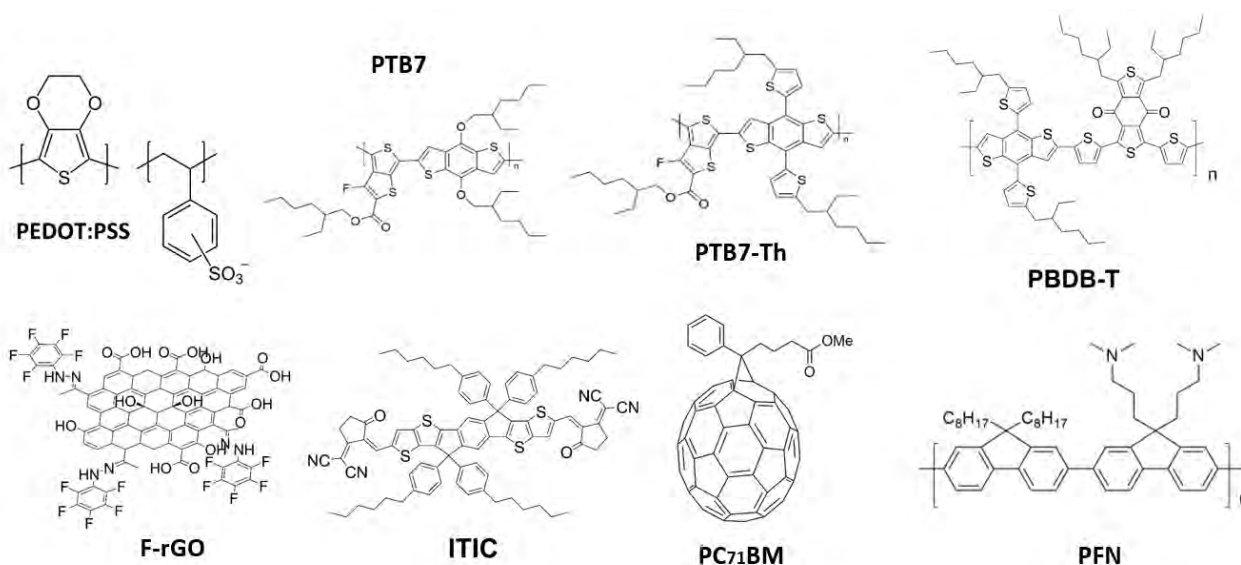
F-rGO: Fluorinated reduced graphene oxide.

ITIC: 2,2'-[[6,6,12,12-Tetrakis(4-hexylphenyl)-6,12-dihydrodithieno[2,3-d:2',3'-d']-s-indaceno[1,2-b:5,6-b']dithiophene-2,8-diyl]bis[methyldiylidene(3-oxo-1H-indene-2,1(3H)-diylidene)]]bis[propanedinitrile].

PC₇₁BM: [6,6]-phenyl-C₇₁-butyric acid methyl ester.

PFN: Poly[(9,9-bis(3'-(N,N-dimethylamino)propyl)-2,7-fluorene)-alt-2,7-(9,9-dioctylfluorene)].

“Chemical structures of the used materials”



1. Introduction

Nowadays, renewable energies are some of the most important topics worldwide because of the increase in the demand for in electricity, the unavoidable depletion of fossil fuel resources, and the environmental impact. Wind, water, geothermal heat and sunlight are some of the sustainable resources used to generate energy. One of the key aspects of renewable energies is that they are inexhaustible, along with the fact that their exploitation is environmentally friendly. In Figure 1.1, the estimated distribution of energy sources of total energy consumption in 2016 is shown. As can be observed, the biggest share of energy generation came from fossil fuels (79.5%), followed by 7.8% from traditional biomass, 2.2% from nuclear energy, and 10.4% from a mix of modern renewable technologies (combined renewable energy adds up to an estimated 18.2%). The biggest portion of modern renewables corresponds to electricity with 5.4% (3.7% from hydropower, and 1.7% from wind, solar, biomass, geothermal and ocean power), followed by thermal energy (4.1%) and transport biofuels (0.9%) [1].

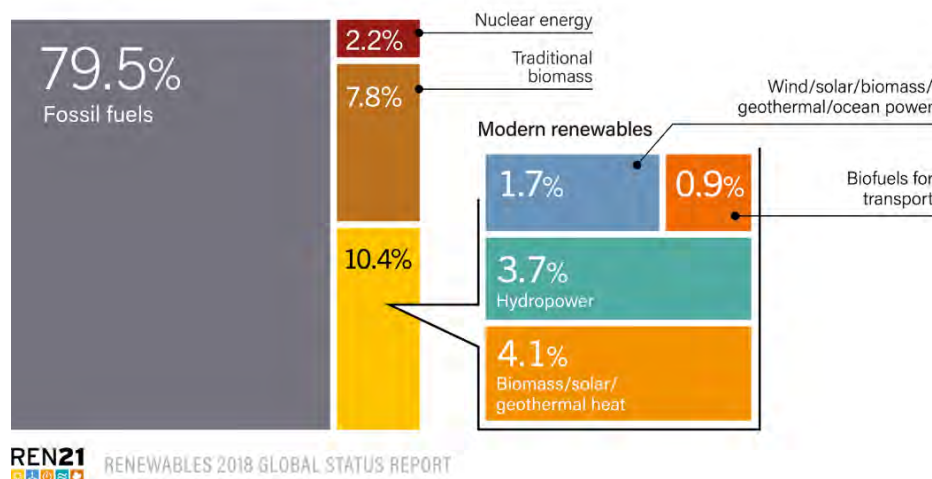


Figure 1.1: Estimated distribution of energy sources of total energy consumption in 2016 [1].

Some of these technologies are growing very fast, such as wind and solar photovoltaics (PV), as seen in Figure 1.2. In spite of the great acceptance of wind and solar PV energy sources, the growth of these technologies is affected by high demand and human population growth [1].

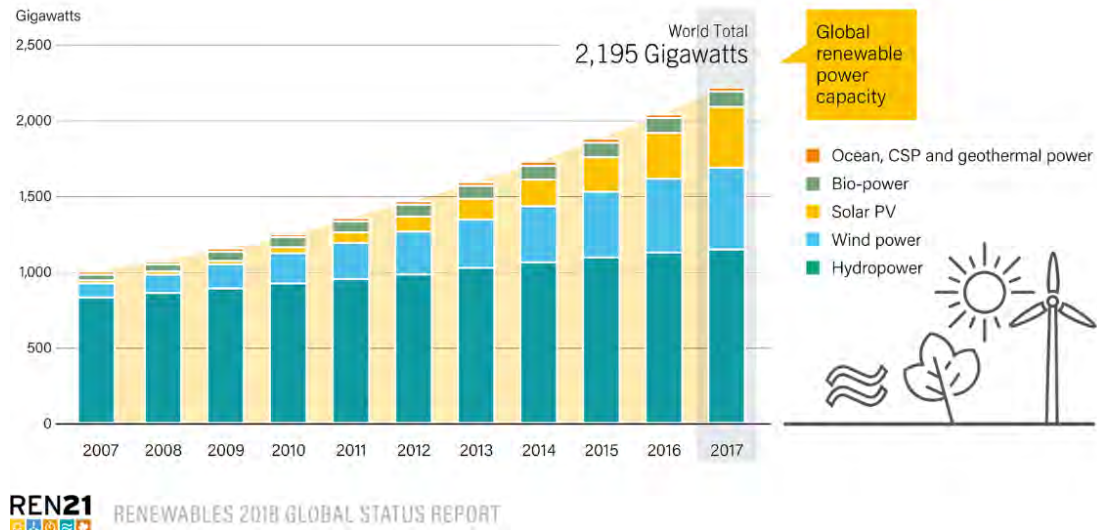


Figure 1.2: Global renewable power capacity from 2007 to 2017 [1].

Solar PV energy had a historical year in 2017. The growth in installed solar PV technology capacity was bigger, as compared to any other energy generation technology, and solar PV energy was the main source of new power capacity in several countries, including China, India, Japan and the United States. In 2017, as shown in Figure 1.3, solar PV energy had an impressive improvement in installed capacity of ~33%, at least 98 GW, in comparison to 2016. Approximately, 402 GW of solar PV energy were in operation worldwide at the end of 2017, which means that an average of 40,000 solar panels were installed every hour of the year. The top countries having the largest solar PV technology capacity are China, the United States, Japan, Germany and Italy, but several countries worldwide are also contributing significantly to the growth of the use of solar energy technology [1].

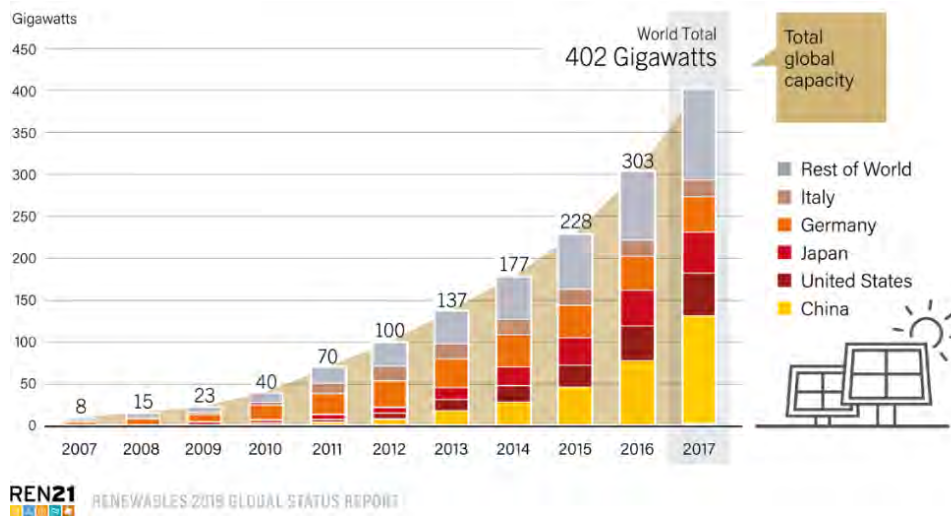


Figure 1.3: Solar PV Global Capacity by Country from 2007 to 2017 [1].

In Mexico, there have been efforts made to increase the use of renewable energies; in fact, a 35% increase in renewable power generation is expected by 2024, 37.7% by 2030 and 50% by 2050. In 2017, Mexico was among the Top 10 Countries with better geothermal power capacities, occupying the 6th place after New Zealand, and the use of such technology could satisfy 1.7% (5.9 TWh) of the country’s electricity needs during a year. Also, concentrating solar thermal installations were added during the same year in Mexico, the majority for industrial applications, having a total estimated capacity of 2.8 MW. Solar thermal heat has become more cost-effective than heat from fossil fuel boilers. For wind power capacity, Mexico is ranked second in Latin America and the Caribbean for total capacity (4 GW). Mexico has increased the investment in renewable energy by 6 billion USD [1]. One of the technologies that needs to be more exploited is that of solar PV cells, principally because of the feasibility of using it in Mexico due to the country’s geographic situation, which puts it under high sun irradiation throughout the year (~ 5.5 kWh/m²) [2].

This technology has evolved through time. In 1839, the first attempt in the area was made by the French Becquerel, who experimented with electrochemical cells [3]. In 1954, solar cells based on a P-N junction silicon semiconductor were built by Chapin and Bell laboratories [4]. Subsequently, thin-film photovoltaic cells were manufactured with inorganic semiconductors [5]. Then, in 1986, C. W. Tang began to deal with photovoltaic organic solar cells (part of the so-called third generation of solar cells) reaching a power conversion efficiency of about 1% [6].

Solar PV cell technologies can be divided into three generations. Crystalline silicon based solar cells are the first generation and, in fact, remain dominant in markets; they have good performance and stability, but they are still expensive and have some important drawbacks. Thin film PV cells based on inorganic semiconductors are the second generation and have some advantages over the first: generally, they have better absorption, can be processed onto large area substrates, and are a bit less expensive, but they are based on rare elements, and are still costly. Our generation of interest is the third, solar PV cells based on organic materials like polymers or small molecules; they are divided into dye-sensitized, multijunction cells, hybrid and organic devices [5,7], reaching, until now, PCEs of 14% [8], 17.3% [9], 23.7% [10] and 16.5% [11] respectively. Figure 1.4 shows the best research cell efficiencies from 1976 to 2019, revised by the National Renewable Energy Laboratory (NREL) [12]. Since 2003, it has been predicted that the new generations of OPVs and hybrid photovoltaic cells will become a cutting-edge technology, capable of providing sustainable and affordable energy. In particular, organic photovoltaic solar cells (OPVs) have several advantages over other photovoltaic technologies, and for that reason, they are at the core of what this work is about. At present, a lot of work is being done to develop this type of cells so that they can be used on an industrial scale. A key factor to achieve this is to develop organic materials that have the technical and economic characteristics required to be used in an industrial environment [13,14]. In the next chapter, a general overview of this technology will be presented.

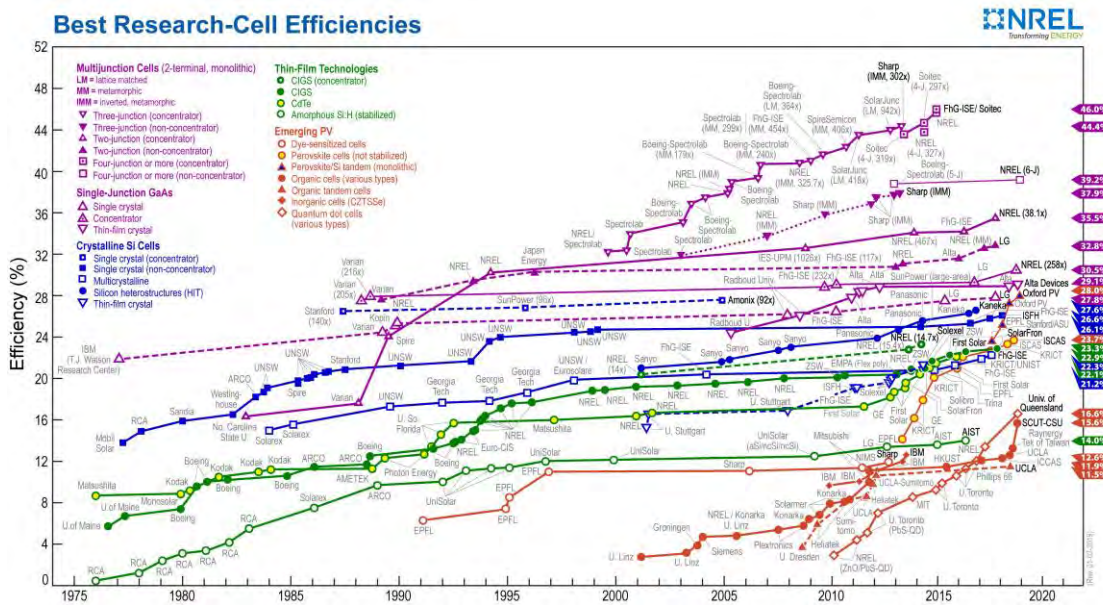


Figure 1.4: Best research cell efficiencies from 1976 to 2019 [12].

2. Organic solar cells

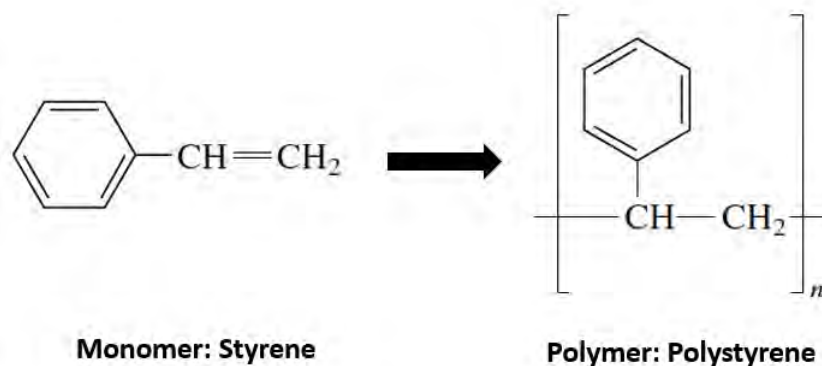
Organic solar cells are devices that convert sun light into electrical power through the photovoltaic effect, using thin films of organic semiconductors [5,7]. At present, OPVs have already achieved 17.3 % of power conversion efficiency (PCE) in a tandem architecture [9] and 16.5 % in a single-junction inverted architecture [11]. Also, commercial OPV panels with a PCE of $\sim 2\%$ and a size of $2.52 \times 0.52 \text{ m}^2$ are being tested [15]. Despite these recent PCE improvements at the laboratory level, it is still necessary to take into account important factors for large-scale commercialization of OPVs, such as stability (including flexible devices), fabrication processes and better efficiencies. This type of emerging technology has been widely studied because of its advantages over other solar cell technologies, which are mainly its low-cost, ease of fabrication, flexibility, low environmental impact, light weight and semi-transparency [16–21]. OPVs have two important disadvantages, relatively low power conversion efficiency and poor stability. The low efficiency depends largely on the architecture, active layer area, materials and method of fabrication used. The relatively poor stability entails, as a consequence, a short lifetime for the devices and this is due to ambient factors such as humidity, oxygen, temperature and illumination, among others [22]. These important disadvantages can be addressed with the use of new semiconductor materials, electrodes, encapsulation materials, etc.

2.1. Organic semiconductors

Organic semiconducting materials are carbon compounds and their derivatives, and they have very attractive properties to be used in photovoltaic applications (OPVs), light emitting diodes (OLEDs) and field-effect transistors (OFETs); some of these characteristics are that they have high absorption coefficients, mechanical flexibility and sufficient electrical conductivity, as well as being non-toxic, relatively cheap, easy to process and band-gap adjustable, among others [7]. The organic molecule structure is mainly formed by carbon-carbon and carbon-hydrogen bonds. Carbon atoms can be linked by conjugated bonds (an alternating single bond-double bond structure between them), and this leads to an extended delocalized π -electron system with good electronic polarizability, enabling absorption in the visible region and electrical charge transport [23]; other atoms can be on the structure, and they are named functional groups, such as hydroxyl, ether, aldehyde, ketone, carboxyl, etc. [24].

According to their molecular weight, there are two major classes of organic semiconductors: small molecular weight materials (monomers) and conjugated polymers (repetition of a monomer); in scheme 1 it is shown an example of a monomer (styrene) and a polymer (polystyrene). Those from the first class are interesting because of their ability to form ordered structures that enable high carrier mobilities; they are formed by conjugated π -electron systems and are deposited by means of vacuum deposition [25]. Those from the second class are formed by a chain of carbon atoms in a π -conjugated network, possibly with side chains to improve solubility in organic solvents. Their conjugated bonds define the material's electrical and optical properties. Polymers can be classified as low, medium or wide bandgap polymers. When lower bandgap polymers are used, better OPV efficiencies are expected [7].

Scheme 1: “Monomer and polymer”



In general terms, an organic semiconductor is a material that is capable of conducting electric charges. This type of materials have energetic levels that are analog to the valence and conduction bands of inorganic semiconductors, and they are the highest occupied molecular orbital (HOMO) and the lowest unoccupied molecular orbital (LUMO), respectively; the bandgap is the separation between them [24]. The HOMO level is full of electrons that can be excited and moved to the LUMO level (free of electrons), only if the absorbed photon energy is bigger than the bandgap energy [26]. The bandgap is responsible for absorption in organic materials. The absorption spectrum depends inversely on the bandgap, which means that if the bandgap is narrow, the absorption spectrum is wide and shifted to higher wavelengths; then, it is convenient to have low bandgap polymers, as mentioned before [27]. It is necessary that the organic semiconductors used in active layers absorb in the visible and near infrared spectrum (approximately from 400 to 1200 nm).

Organic semiconductors are also classified as electron-donor or electron-acceptor materials. Donors are those that have a low ionization potential, and thus, can easily donate an electron, while acceptors are those that have high electron affinity, and thus, can take up an electron [7].

2.2. Architecture

An OPV can be fabricated in two different configuration types: direct or inverse. In Figure 2.1a, the direct configuration is shown, consisting of a positive semitransparent electrode or anode (indium tin oxide (ITO), generally employed on top of a substrate), a hole transport layer (HTL), an active layer (where the photovoltaic process takes place), an electron transport layer (ETL), and a negative electrode or cathode [28]. In Figure 2.1b, the inverse configuration is shown, consisting of a negative semitransparent electrode (cathode) on top of a substrate (also ITO as the most frequently used), an ETL, an active layer, an HTL, and a positive electrode (anode) [29]. In this last structure, light goes into the OPV's cathode side, and ITO changes its function from anode to cathode, with the help of the buffer layers. The anode and the HTL (in the direct configuration), or the cathode and the ETL (in the inverse configuration), have to be semitransparent layers to allow the passage of light. HTL and ETL, also known as buffer layers, have important functions on the performance of solar cells; respectively, they improve the selectivity of charges and the collection of holes and electrons, facilitating charge collection at the electrodes. Poly(3,4-ethylenedioxythiophene) polystyrene sulfonate (PEDOT:PSS) is one of the most commonly conductive polymers used in OPVs as HTL because of its semitransparency and charge selectivity. As ETLs, several materials are used, such as metal oxides (ZnO, TiO), lithium fluoride (LiF) and poly[(9,9-bis(3'-(N,N-dimethylamino)propyl)-2,7-fluorene)-alt-2,7-(9,9-dioctylfluorene)] (PFN), among others. In Figure 2.2, the chemical structures of PEDOT:PSS and PFN materials can be observed, which were respectively used as HTL and ETL in this work for the fabrication of direct OPVs. The anode and cathode have different work functions to help charge transport and collection. Work function is the energy needed to pull out or insert an electron from or into the material. ITO is one of the most used electrodes (anode or cathode for direct or inverse configurations, respectively) due to its semitransparency, high work function and low sheet resistance. Some of the metals used as cathodes are aluminum (Al), silver (Ag) or other metals that have low work function values.

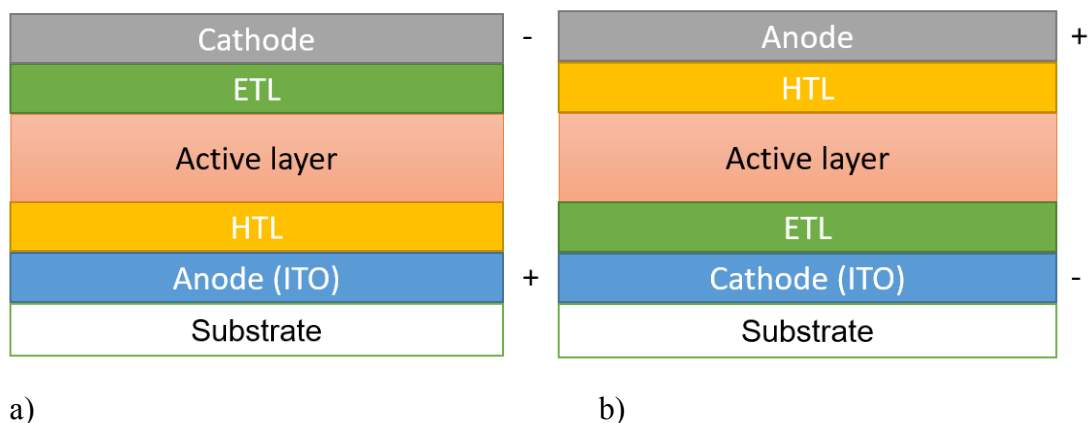


Figure 2.1: OPV (a) direct and (b) inverse configuration.

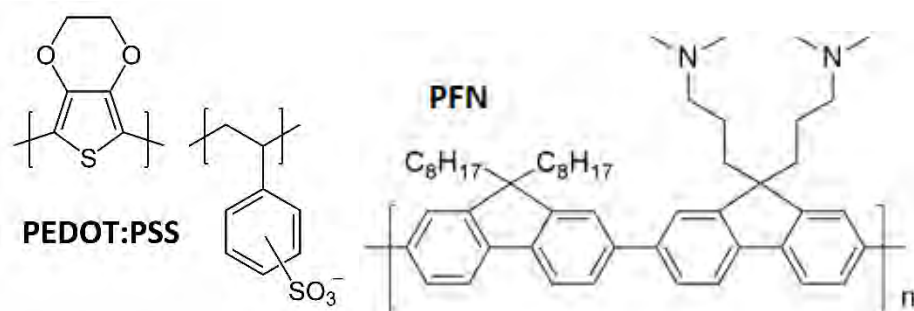


Figure 2.2: Chemical structures of two of the materials used as HTL (PEDOT:PSS) and ETL (PFN).

An OPV active layer can also be made with different structure configurations: bi-layer [30], bulk-heterojunction (BHJ) [31] and tandem [32]. A bi-layer structure (Figure 2.3a) is that where the donor and the acceptor layers are deposited as two independent layers; a main disadvantage of this kind of structure is that there may be loss in some donor-acceptor contact areas, which in consequence affects the generation of charge carriers (CCs). The BHJ approach (Figure 2.3b) is the most promising configuration in order to enhance interpenetrated interface area in OPVs, since it contributes to having an efficient charge separation of the excitons into CCs [33–35]; in this approach, a donor-acceptor mix is prepared into a solution, and then is deposited as a thin film, forming a nanoscale network of the materials and allowing good electric contact; BHJ OPVs can be binary (a mix of two materials) [28], ternary (a mix of three materials, Donor:Donor:Acceptor or Donor:Acceptor:Acceptor) [36], or even quaternary (a mix of four materials) [37], and OPV performance strongly depends on the morphology of this BHJ layer, for if such morphology is not good enough, there can be recombination processes inside the bulk, and this causes PCE decay. Finally, but not less important, there is the tandem structure (Figure 2.3c), which is a “sandwich”

of stacked OPVs connected in series or in parallel; this type of structure is used to increase active layer absorption range and to produce bigger open circuit voltage (V_{oc}), but it is complicated to join the OPVs and choose the right materials for their good performance. Nowadays, BHJ is the principal structure used in many research works, as it was in conducting the work leading to this thesis dissertation.

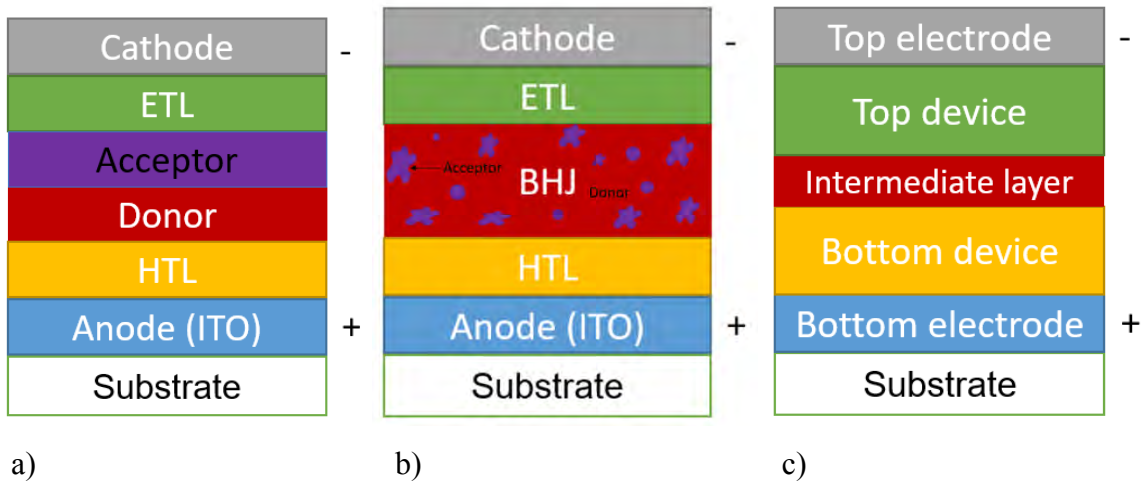


Figure 2.3: OPV (a) bi-layer, (b) heterojunction and (c) tandem structure in direct configuration.

2.3. Working principle

OPV performance depends largely on the mismatch of the energy level alignment of each component (HOMO and LUMO cascade between materials), organic compounds and architecture used, type of solvent, active layer deposition technique, annealing conditions, and thickness and morphology, among other factors [38,39]. The active layer is where the photovoltaic process takes place, and for that reason, it is extremely important to control the thickness and morphology of this layer, since these parameters directly affect the four principal OPV processes: light absorption, exciton dissociation, charge transport and charge collection [40–45]. It is well known that a thicker film has better light absorption than a thinner film, but also, it could increase the series resistance and affect CC transport and collection [46]. On the contrary, a thinner film could convert arriving photons into collected charges more efficiently [47], although not at the required largest rate because of the reduced absorption; thus, among other factors, the most adequate active layer thickness must be determined. CC lifetime and transit time define the upper limit for the active layer thickness in order to get efficient charge collection [48]; optimum active layer thickness is about 100 nm for most BHJ architectures [49–52]. After a brief explanation about the active layer,

the general working principle of these devices can be explained through the four principal OPV processes mentioned before.

Light absorption and exciton generation

As shown in Figure 2.4, a photon of incident light travels through the semitransparent anode and the HTL, and it is absorbed at the active layer by the donor polymer, exciting an electron from the HOMO to the LUMO level of the material (if the photon energy is bigger than the organic semiconductor bandgap), creating a Coulombic bound electron-hole pair (exciton) [53].

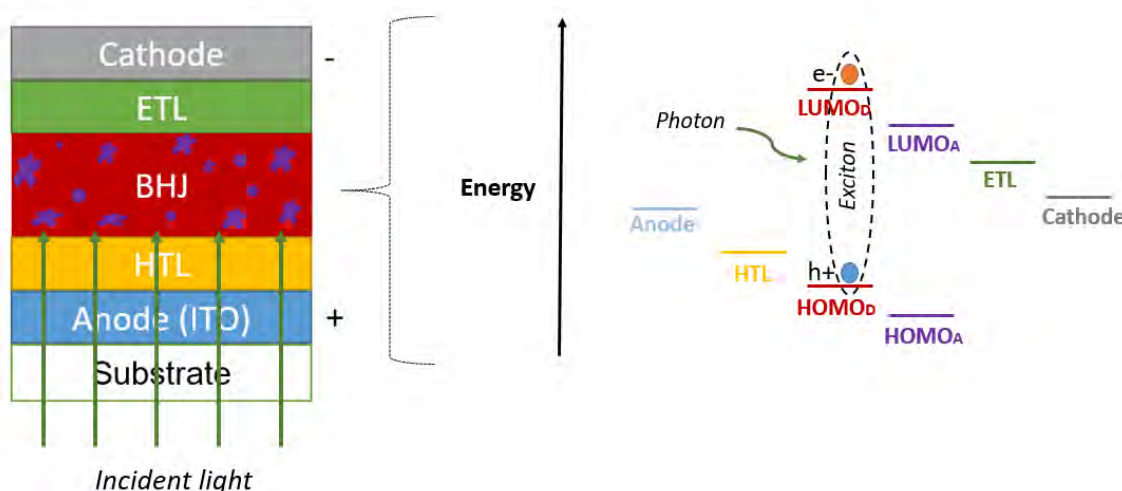


Figure 2.4: Light absorption and exciton generation.

Exciton dissociation

The generated exciton needs to diffuse (within the donor polymer) to reach the donor-acceptor contact interface and dissociate into CCs before recombination, as shown in Figure 2.5. The dissociation at the interface can occur only at energetically favorable acceptor molecules, transferring the electron from the LUMO of the donor material to the LUMO of the acceptor material, and dissociating into independent charges (leaving a hole in the HOMO level of the donor material) [53]. The energy difference between the LUMOs of the materials has to be larger than the exciton binding energy, at least 0.3 eV [7], and the LUMO of the acceptor material should have lower energy than the LUMO of the donor material. It is also important to mention that if the active layer is very thick (optimal active layer thickness is about 100 nm, as mentioned before), or the

materials' domain sizes are large (> 20 nm), then the probability of exciton recombination increases significantly, since exciton diffusion length is between 5 and 20 nm in organic materials [24,54]. Therefore, it is required that the donor and acceptor material form interpenetrating domains with a phase separation on the order of the exciton diffusion length to avoid charge recombination and to get efficient photocurrent generation [55].

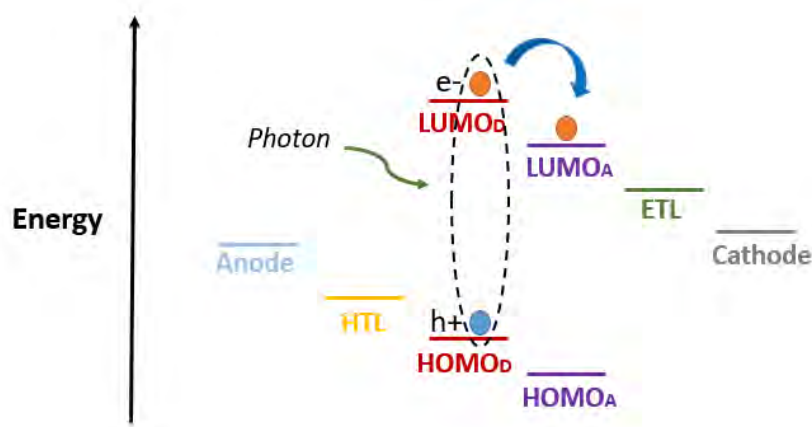


Figure 2.5: Exciton dissociation.

Charge transport

Once there are independent charges, a hole in the donor material and an electron in the acceptor material, they move through the donor HOMO and the acceptor LUMO respectively, in search of balance (as shown in Figure 2.6). The transport of CCs is limited by the active layer's charge mobility [53].

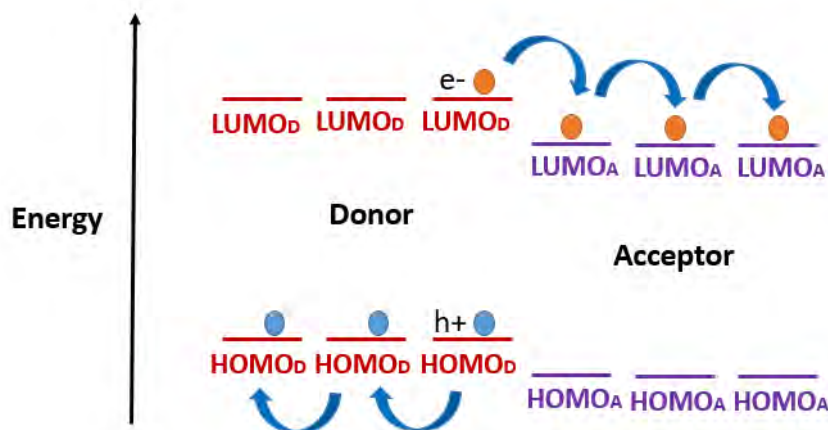


Figure 2.6: Charges transport.

Charge collection

HTL and ETL layers play an important role in avoiding charge recombination; they are selective with the holes and electrons charges respectively, and therefore, help CCs arrive to electrodes. It is very important to have the adequate ohmic contact between the OPV layers, because this influences CC transport in a strong fashion. Holes and electrons are then respectively collected by the anode and the cathode, as shown in Figure 2.7. The electrodes' work functions have to be also aligned in the energetic level system, for they make current generation possible [53].

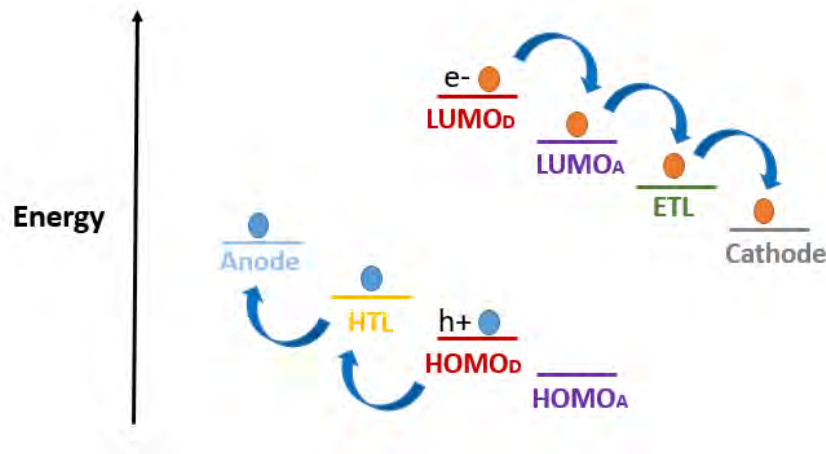


Figure 2.7: Charges collection.

There are different loss mechanisms from the absorption to collection processes that limit the device's performance. Geminate recombination happens when the same electron-hole pair is recombined radiatively, meaning that the exciton is relaxed to the ground state before dissociation due to its inability to reach the Donor-Acceptor interface [56]. Excitons have a few nanoseconds (~ 100 ns) to dissociate before radiatively recombining, so, if the materials' domain size is larger than the exciton diffusion length, the possibilities for recombination increase, as mentioned before. Non-geminate recombination happens when free CCs are traveling to the electrodes, and a free electron and hole are recombined (called bimolecular recombination), or when a free CC finds an opposite trapped CC and recombines (trap assisted recombination). The main difference between geminate and non-geminate recombination is that in the second case, the CCs did not stem from the same photon. For non-geminate recombination, time is between nanoseconds and milliseconds, and can be influenced by charge carrier mobility, active layer thickness, phase separation, etc. [56].

2.4. Fabrication

The steps of the fabrication process are explained below.

Substrate cleaning

The first fabrication step is the preparation of substrates. ITO covered glass substrates (glass/ITO electrode) are cut (in this work: $\sim 1.8 \text{ cm} \times 1.8 \text{ cm}$) and ultrasonically and sequentially cleaned for about 20 minutes in some solvents (in this case, in a detergent solution, distilled water and ethanol), and then, dried in an oven at $80 \text{ }^\circ\text{C}$ for at least 12 h. Finally, ITO substrates are treated with UV-Ozone plasma for 20 minutes to eliminate organic residues and contribute to adhesion to the next layer.

Solution preparation

Preparation of the active layer solution is the most important part of the fabrication process. It is necessary to select the right materials (donor and acceptor), π -conjugated systems with HOMO and LUMO levels forming a level cascade-like to make charge dissociation and transport possible, with a difference between donor and acceptor LUMOs of $\sim 0.3 \text{ eV}$, as mentioned before. The donor bandgap needs to be less than the acceptor bandgap, so that it requires less energy to get more easily excited. Then, the solvent for the solution has to be selected; solvent plays an important role in the morphology of the active layer, and for that reason, it is important to select the right one for the mix. It is extremely important that both donor and acceptor materials are soluble in the solvent, and this can be known by analyzing the materials' polarities. To maintain solution concentration, it is necessary that solvent boiling temperature be much greater than ambient temperature to avoid excessive evaporation. The solution is prepared mixing donor and acceptor materials at a specific ratio (for example: 1:1.5 w/w respectively), dissolving them to a specific concentration (for example: 30 mg (organic materials)/ml (solvent)), and then stirring the solution on a hot plate to obtain a well dissolved solution. It is necessary to control material ratio and solution concentration to obtain the right active layer thickness and morphology, thus achieving good device performance.

Film deposition

Once we have dried the substrates and prepared the solution, we can start depositing OPV films in the following order (for direct configuration): HTL, active layer and ETL. At the laboratory level, there are several OPV film fabrication methods, such as drop casting, spin coating and doctor

blading. One of the most frequently used techniques for active layer deposition is spin-coating, a technique in which polymers form films with low RMS roughness ($\sim 1\text{-}3\text{ nm}$) [57]. In this technique, the substrate is placed into the spinner and held in position by means of vacuum; then, the solution is added on top of the substrate, and the spinner starts to rotate with specific acceleration, angular speed and rotation time to evaporate the solvent and form the film, and through those parameters, it is relatively easy to control and reproduce film thicknesses; this deposition technique is principally used for OPVs with small areas. Another important technique that has recently been used a lot is doctor blading; which uses a metallic base where the substrate is placed, and then a blade moves along, dragging the solution and covering the substrate; with this technique, it is possible to make films with well-defined thickness at major OPV areas [58]. At the end of each film deposition, thermal and/or solvent annealing are necessary for structure ordering and drying. In this work, the spin-coating method was the one used to deposit OPV films.

Cathode deposition

The last step in OPV fabrication process is the deposition of the top electrode. The top metal electrode work function has to adequately connect with the ITO work function, favoring the flow of electrons. The most frequently used methods for top electrode deposition are evaporation and drop casting. Evaporation is the most expensive method because it requires equipment with special conditions, such as high-vacuum and high temperature; the material is deposited on top of the last OPV layer by means of a sublimation process. Drop casting is the cheapest way to deposit the top electrode. The metal is melted in a hot plate (at the metal boiling point temperature), and the substrate is put on the hot plate at the same temperature, so that it reaches a temperature similar to that of the metal, and then, the drop is placed at the top of the OPV; next, the melted metal is spread on top of the OPV, the device is removed from the hot plate, and the metal is allowed to solidify. Not all metals can be deposited using this last method, because the boiling points of some are too high, as is the case of Al or Ag. In this work, an alternative free-vacuum deposited top electrode was used; Field's metal (FM) is an eutectic alloy that has been previously used by our group [16,38,59–61], which is made up of 32.5% Bi, 51% In and 16.5% Sn by weight, has a melting point above 62°C , and can be deposited through drop casting at low temperature ($\sim 95^\circ\text{C}$) and room environment conditions [16,38,59–61], unlike other standard top electrodes (such as Al) that need to be deposited using high-vacuum evaporation, increasing device cost.

2.5. Characterization techniques

In the dark, an ideal solar cell behaves as a semiconducting current rectifier (or diode), see Figure 2.8 green curve, and can be represented by a current source connected in parallel with a rectifying diode. The corresponding current-voltage (J - V) characteristics are described by Shockley equation [5,62] ,

$$I = I_{ph} - I_0 \left(e^{\frac{qV}{k_B T}} - 1 \right) \quad (1),$$

where k_B is Boltzmann's constant ($1.38 \times 10^{-23} \text{ m}^2 \text{ kg} / (\text{s}^2 \text{ K})$), T is the temperature in Kelvin degrees, q is the electron charge, V is the voltage, I_{ph} is the photocurrent under illumination, and I_0 is the saturation current in the dark.

In practice, the J - V characteristics of a solar cell differ from the ideal characteristics because of leakage currents in the device. Therefore, a real OPV can be modeled with an equivalent circuit to take into account parasitic resistances (series and parallel resistances), and the analytical expression to model the equivalent circuit is governed by equation (2) [63,64] ,

$$I = I_0 \left(\exp \left(\frac{V - IR_s}{nk_B T} \right) - 1 \right) + \frac{V - IR_s}{R_{sh}} - I_{ph} \quad (2),$$

where n is the diode ideality factor (normally between 1 and 2), and R_s and R_{sh} are the series and parallel resistances, respectively, along with the other parameters that were previously defined.

OPV power conversion efficiency can be estimated through the J - V curve under illumination. The solar simulator used for J - V characterizations imitates the standard spectrum Air Mass 1.5 (AM1.5) with specific characteristics: sun angle zenith of 48.2° and an intensity of 100 mW/cm^2 . The solar simulator employed for this work was the Sciencetech SS150 class AAA, and it was calibrated using an Oriel reference cell. J - V curves were measured using a Keithley 2450 source meter under normal room conditions. To that end, the OPV was illuminated with the solar simulator, and the source meter was connected to the electrodes, where a potential difference sweep was applied to the cell, with the generated current being measured at the same time. With the applied voltage and the generated current, the J - V graph can be plotted, see Figure 2.8 blue curve. The important parameters that define OPV quality can be determined using the J - V curve.

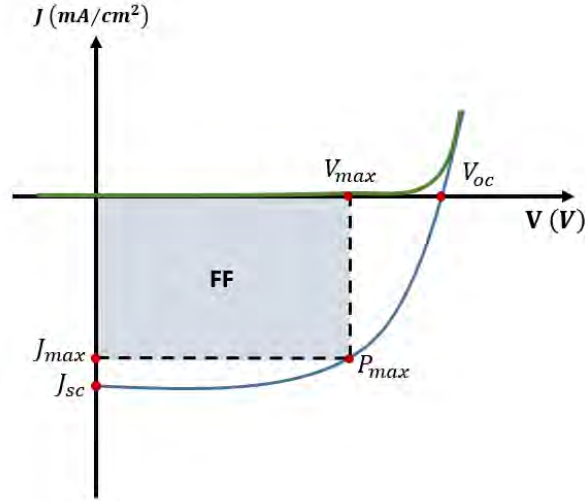


Figure 2.8: *J-V curve of a solar cell (with light->blue, in dark->green), with the main OPV parameters.*

Short circuit current density (J_{sc}) and open circuit voltage (V_{oc}) are obtained directly from the curve; they are at the intersections with the vertical and horizontal axes, respectively. J_{sc} is the value where V_{oc} is zero, and V_{oc} is the value where J_{sc} is zero. J_{sc} can be affected by the donor bandgap and CC dissociation. V_{oc} can be theoretically calculated as the difference between the donor HOMO and the acceptor LUMO, and it can be affected by the active layer morphology and the electrodes' work functions. Fill factor (FF) is the square area represented in Figure 2.8, and it is defined by equation (3):

$$FF = \frac{P_{max}}{J_{sc} * V_{oc}} = \frac{J_{max} * V_{max}}{J_{sc} * V_{oc}} \quad (3),$$

where P_{max} is the maximum power point at a voltage V_{max} and a current density J_{max} . For a high PCE, a small R_s and a large R_{sh} are required, and these parameters are highly impacted by active layer morphology. Then, to obtain a high FF , it is necessary to have low roughness and optimized thickness of the active layer in order to have good charge separation and transport.

PCE of solar cells can be calculated by means of equation (4),

$$PCE = \frac{P_{max}}{P_{in}} * 100\% = \frac{J_{sc} * V_{oc} * FF}{P_{in}} \quad (4),$$

where P_{in} is the source power (100 mW/cm^2) under the AM1.5 standard.

2.5.1. Complementary characterization techniques

UV-Vis spectroscopy: It is one of the most widely used techniques in almost every laboratory. It measures the intensity of light before it goes through the sample, and compares it with the light intensity that goes out of the sample; spectroscopic analysis is commonly carried out in solutions and solids [65]. In this work, a Lambda 900 UV-Vis spectrometer from Perkin Elmer Instruments was used for UV-Vis absorption measurements.

Atomic force microscopy (AFM): This is a powerful imaging technique and a common tool for material characterization, reaching resolutions on the nanometer scale. It has different ways of interacting with the sample. With AFM, mechanical, electrical, magnetic and optical spectroscopic properties of a sample can be characterized [66]. In this work, an AFM Easyscan2 from Nanosurf was used.

Scanning tunneling microscopy (STM): It is a technique used for imaging at the atomic level, which works on the basis of the quantum tunneling concept. A conducting tip is placed very close to the sample, and a voltage is applied, thus obtaining a surface image at the atomic scale [67]. In this work, STM determinations were carried out under ambient conditions with a Nanosurf Easyscan 2 STM device (by means of the liquid/solid interface technique [68,69]).

Scanning electron microscopy (SEM): This technique scans a surface with a high-energy focused beam of electrons, penetrating the sample to a given depth (depending on the accelerating voltage), and then, the electrons interact with the atoms in the sample, generating signals that are employed to get information of the surface. Optical resolution of SEM (between 1 and 20 nm) is much better than that achieved with a modern optical microscope (> 200 nm) [70,71]. In this work, SEM images were acquired with a Jeol JSM 7800F electron microscope.

X-ray diffraction (XRD): It is a nondestructive analytical technique for material characterization that gives detailed information about structures, chemical composition, phases, crystal orientations, crystallinity, and so forth. An X-ray monochromatic beam is projected onto the sample, and then scattered at specific angles caused by the interaction with the sample. The scattered X-rays interfere with each other, and the diffraction peaks are produced by the constructive interference between them [72]. In this work, X-ray diffraction pattern generation was carried out with a Bruker D2 PHASER.

Cyclic voltammetry (CV): It is a standard technique used for measuring electrochemical properties; it applies cycling potential scans, and measures the resulting current at the working electrode. With it, one can obtain qualitative information about the orbital energy levels of materials used for organic electronics [73]. CV measurements, in this work, were carried out using a PARSTAT 2273 potentiostat in a classical three-electrode electrolytic cell.

There are many other techniques for the characterization of solar cell and materials, such as impedance spectroscopy (IS), or light beam induced current/voltage (LBIC/LBIV), among others [60,74,75]. One important characterization technique that was used in this work is external quantum efficiency (EQE), or incident photon to current efficiency (IPCE). In the next chapter, it will be explained in detail.

3. External Quantum Efficiency

In order to realize the operational limit of these devices, it is important to understand the operating mechanism for OPVs and the principal processes related with PCE. The main processes (as explained before) are (i) photon absorption in the active layer, which produces the photogenerated excitons (η_{Ab}), (ii) exciton dissociation and CC generation (η_{CG}), (iii) transport of the holes by the donor conjugated material and the electrons through the electron acceptor material and the subsequent transfer of these CCs across the respective transport layers (η_{CT}), and finally, (iv) CC collection at the electrodes (η_{CC}) [50]. Those four processes directly affect the PCE value, and they can be analyzed through the EQE technique. EQE rules the performance of OPVs; it is the ratio between the generated and collected charges and the total number of incident photons, as shown in equation (5). EQE is expressed in terms of the four aforementioned processes according to equation (6) [50,55].

$$EQE = \frac{\text{number of generated and collected charges}}{\text{number of total incident photons}} \quad (5)$$

$$EQE = \eta_{Ab} \times \eta_{IQE} = \eta_{Ab} \times \eta_{CG} \times \eta_{CT} \times \eta_{CC} \quad (6)$$

Also, EQE measurements are a complement to the $J-V$ plots for both stability monitoring and OPVs characterization [55,76]. Nevertheless, the experimental acquired EQE value is often not enough to completely understand OPV performance, and calculation of internal quantum efficiency (IQE) is also important [77,78]. To determine IQE data, it is necessary to know the internal absorption (Q_{AL} or η_{Ab} as named above) of the active layer, as shown in equation (7). Then, with EQE and Q_{AL} data, IQE is calculated as shown in equation (8) [50,77,78].

$$Q_{AL} = \frac{\text{number of abs. photons in act. layer}}{\text{number of total incident photons}} \quad (7)$$

$$IQE = \frac{\text{number of generated and collected charges}}{\text{number of abs. photons in act. layer}} = \frac{EQE}{Q_{AL}} \quad (8)$$

Summarizing, EQE takes into account the total number of arriving photons to the OPV cell, and IQE is just related to the net absorbed photons at the active layer. When IQE is close to 100%, almost every absorbed photon results in CCs that are collected at the electrodes [47]. To improve IQE, and thus EQE, active layer thickness needs to have an adequate value. Also, it is important

to mention that variations in the complex refractive index ($\mathbf{n} = n' + ik$) of the layers that form the OPVs stack can affect their performance, specifically the EQE shape [77]. Through the layers' optical constants and thickness values, it is possible to perform simulations of the optical electric field distribution on each layer [77]. Then, it is necessary to get an accurate absorption spectrum of the active layer (Q_{AL}), due to all the internal reflections and interference processes that the stack structure produces [50]. Thus, for device optimization and for efficiency improvement, optical effects must be accounted for.

3.1. Set up

Our EQE experimental set up (homemade) is shown in Figure 3.1. The computer controlled EQE set up was implemented using a monochromator (Princeton Instruments Acton Series SP2500), a xenon lamp (Oriel Instruments model 66902) as light source, a power meter (Thorlabs PM100) with a measurement range from 400 to 1100 nm, a source meter (Keithley 2400), and lenses, irises and mirrors as optical components.

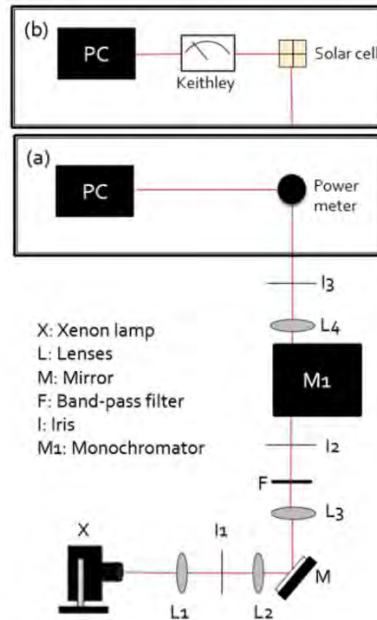


Figure 3.1: EQE experimental set up: (a) initial arrangement for light power measurements, (b) arrangement for OPV current determinations.

In the set-up, light (supplied by the xenon lamp) is collimated with two plano-convex lenses ($f=60$ mm, Thorlabs LA1401-A) and deviated with a mirror, then, it goes through a bi-convex lens ($f=100$ mm, Thorlabs LB1676) to focus the light onto the monochromator slit. An iris is used to

avoid noise at the entrance of the monochromator, and a high-pass filter (Thorlabs FB800-40) is used to avoid second order diffraction at higher wavelengths, see Figure 3.2. The monochromator, by means of diffraction gratings, splits the light into specific wavelengths, and the monochromatic output light passes through a bi-convex lens ($f=125$ mm, Thorlabs LB1904) and an iris to respectively focus and define the light spot, arriving next to the power meter detector (Figure 3.1a); power measurements at each wavelength are saved with the automated system. Then, the OPV is placed at the same position of the power meter detector, and the current is measured by the system with the source meter (Keithley) (Figure 3.1b). Once the current and the power have been obtained, the EQE curve is automatically plotted. A LabVIEW software was developed for the acquisition of EQE data. EQE(λ) values are determined from equation (9) [79] ,

$$EQE(\lambda) = \frac{J_{sc}(\lambda)}{P_{in}(\lambda)} \times \frac{hc}{e} \times \frac{1}{\lambda} = \frac{J_{sc}(\lambda)}{P_{in}(\lambda)} \times 1240 \times \frac{1}{\lambda} = \frac{1240J_{sc}}{\lambda P_{in}} \quad (9),$$

where $J_{sc}[mA/cm^2]$ is the short circuit photocurrent density produced in the cell at each λ , $P_{in}[mW/cm^2]$ is the irradiance of the incident light (at each λ), $\lambda[nm]$ is the incident photon wavelength, h is Planck's constant, c is the light speed, and e is the electron charge [79]. Through the integration of EQE over the solar spectrum, it is possible to evaluate the amount of current that the OPV device will generate upon being exposed to sunlight; then, as it is clear from equation (9), J_{sc} can be determined from EQE measurements. Therefore, to verify EQE results, the J_{sc} PV parameter was calculated from those measurements, and the estimated values were compared with those achieved using the $J-V$ plots; such parameter is calculated as the integral of the product of the measured EQE and the number of incident photons at each wavelength, see equation (10) [50,55].

$$J_{sc} \left(\frac{mA}{cm^2} \right) = \int \frac{P_{in\lambda}\lambda}{1240} \times \frac{EQE_{\lambda}}{100} d\lambda \quad (10)$$

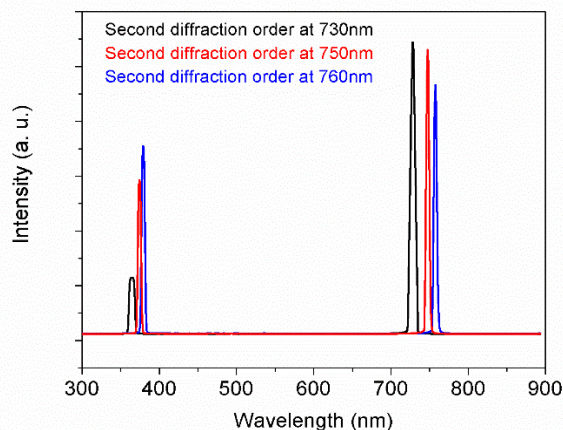


Figure 3.2: Light intensity measured from the monochromator output in order to observe the second diffraction order at different wavelengths (730, 750 and 760 nm).

With the purpose of verifying the reliability of EQE measurements and how OPV reproducibility behaves with the same thickness, two statistical analysis were made. The first analysis was made taking three different EQE measurements for the same cell. In Figure 3.3a and b, three EQE measurements for the same cell and EQE measurements with their standard deviation are respectively shown. The highest standard deviation value is 2.3 %; knowing this value, it is possible to say that the EQE measurements are 97.7 % reliable.

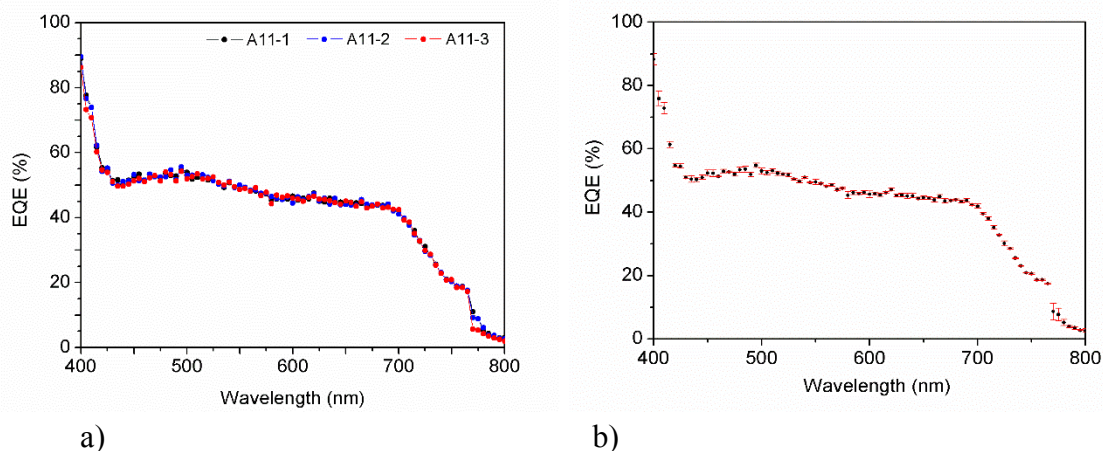


Figure 3.3: EQE measurements (a) for the same OPV cell, (b) with standard deviation. Highest standard deviation is 2.3 %; measurements are 97.7 % reliable.

The second analysis was done to determine the reproducibility error. Five cells on individual substrates were fabricated under the same fabrication conditions. In Figure 3.4 a and b, the $J-V$ and EQE curves of the tested cells are shown. The standard deviation (reproducibility error) in Figure

3.4c was calculated from EQE measurements, with 6.6% error, leaving 93.4% of good cell reproducibility. The highest standard deviations are between 755 and 770 nm, as can be observed for the graph, and this is due to the fact that the high-pass filter is manually placed at these wavelengths; therefore, these relatively high values are mainly due to human errors.

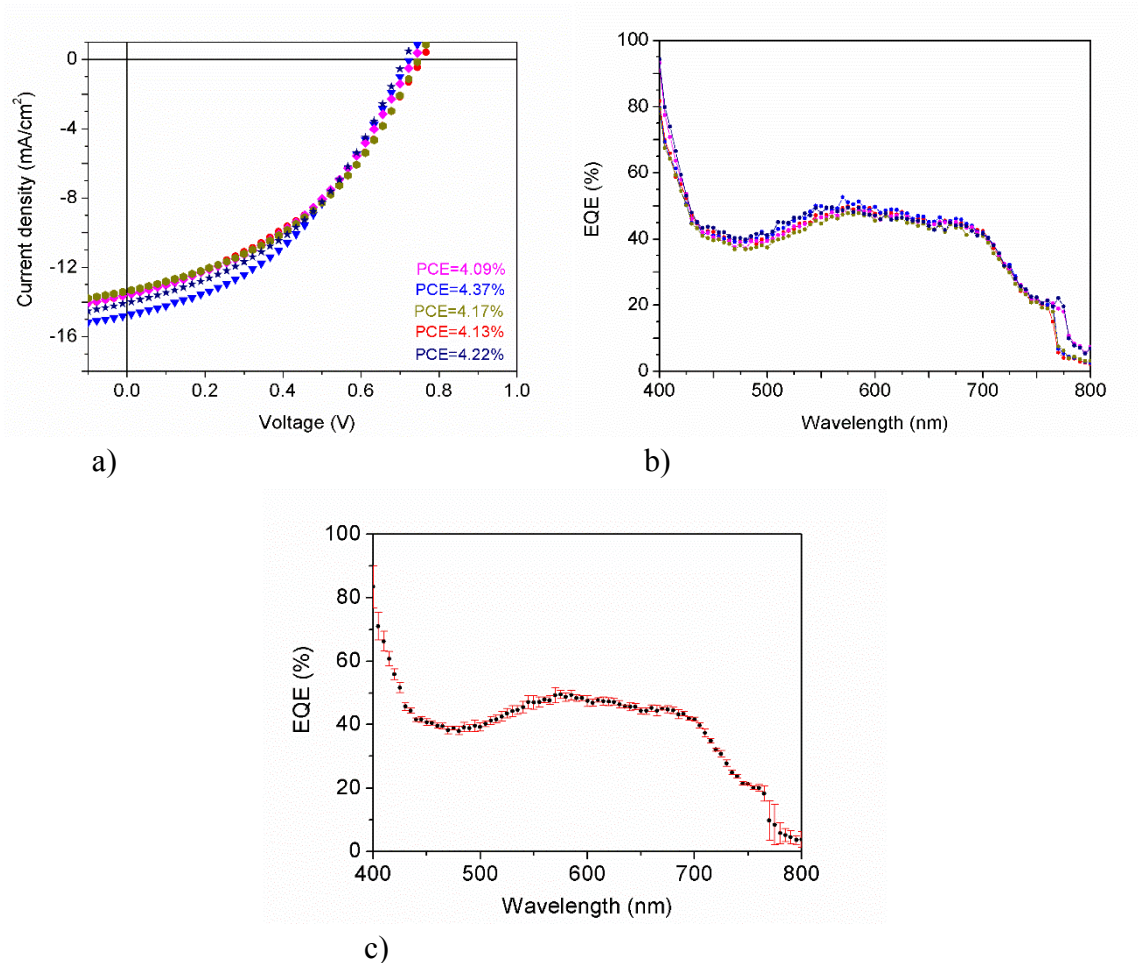


Figure 3.4: (a) *J-V* and (b) *EQE* measurements for five different *OPVs*, and (c) *EQE* measurements with standard deviation. Highest standard deviation (reproducibility error) is 6.6%; reliable reproducibility is 93.4%.

Additionally, the monochromator bandwidth was measured with a spectrometer (Ocean Optics USB 4000) to calibrate the monochromator and to verify that we have the wavelength of interest in the EQE measurements; the calibration procedure was performed using the MonoControl software from Princeton Instruments. In Figure 3.5, the bandwidth measurement at 550 nm is shown, and as can be noted, the full width at half maximum (FWHM) of the curve is 4 nm. As

EQE measurements are taken in 5 nm steps, the desired wavelength will be the obtained wavelength.

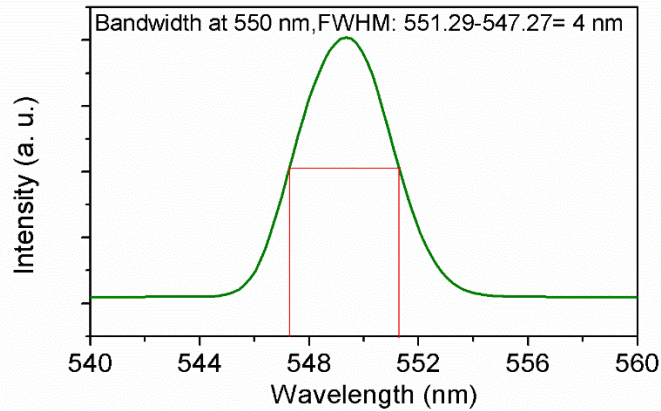


Figure 3.5: Bandwidth monochromator curve at 550 nm, FWHM of 4 nm.

Some images of the EQE homemade set-up are shown in Figure [3.6](#).

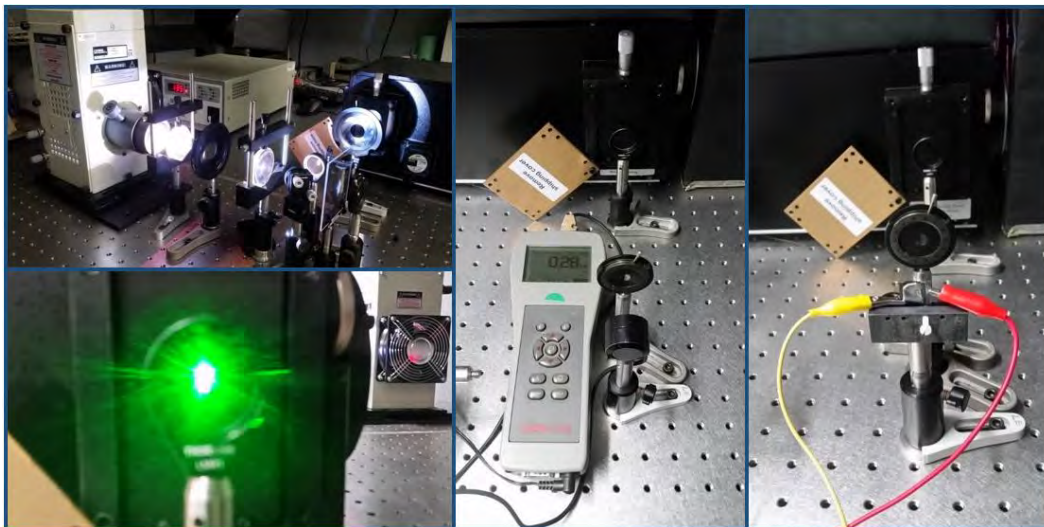


Figure 3.6: EQE homemade arrangement images.

3.2. Transfer Matrix Method (TMM)

As mentioned before, it is necessary to get an accurate absorption spectrum of the active layer, and therefore, optical effects must be taken into account; this analysis can be performed through TMM. This method, is one of the most important numerical methods in contemporary theoretical physics. It helps to predict and understand the behavior of thin films multilayer structures in a specific configuration through the transmission, reflection, absorption and electromagnetic field

distribution inside the layer system [80]. Several authors have used the well-established TMM to calculate Q_{AL} in solar cells by using the optical constants of the film layers, refractive index (n) and extinction coefficient (k). For instance, Moulé et al. [81] demonstrated that optical effects, such as reflections and interference, are responsible for the variations in OPV performance as a function of the active layer thickness; their OPVs' active layers were based on P3HT:PCBM or OC₁C₁₀-PPV:PCBM. Slooff et al. [82] modeled the absorption profile of a PF10TBT:PC₆₀BM active layer and obtained a calculated IQE of 75 %. Jung et al. [83] calculated the spatial distribution of the optical electric field intensity, the power density, and the power dissipation of OPVs based on a P3HT:PCBM active layer, and concluded that total device reflectance has an important impact on light absorption efficiency.

In this work, TMM was used to analyze the electric field distribution inside the OPV's thin film structure in order to optimize performance, and also, to obtain the accurate active layer absorption spectrum for IQE determinations. To use TMM, it is necessary to know the wavelength-dependent complex refractive index of each layer material. Then, through the layers' optical constants and thickness values, it is possible to perform simulations of the optical electric field distribution on each layer. As shown in Figure 3.7, our OPV devices are considered as a stack of m homogenous layers and $m+1$ interfaces which are parallel between them, with specific thicknesses (d) and optical constants (η), namely the dielectric constant $\epsilon_2(\omega)$ and magnetic permeability μ_2 . Film faces are located at $z = 0$ and $z = d$.

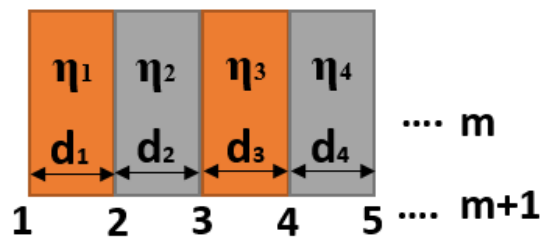


Figure 3.7: OPV cell stack consideration for TMM.

Using the transverse component continuity of the electric and magnetic fields on each surface, E and H respectively, the relationships between fields E_a, H_a at $z = 0$ and E_b, H_b at $z = d$ were obtained through the following expression (11),

$$\begin{bmatrix} \cos(k_2 d) & -isen(k_2 d) \frac{\mu_2}{\beta_2} \\ -isen(k_2 d) \frac{\beta}{\mu} & \cos(k_2 d) \end{bmatrix} \begin{bmatrix} E_b \\ H_b \end{bmatrix} = \begin{bmatrix} E_a \\ H_a \end{bmatrix} \quad (11),$$

where $k_2 = \frac{\omega}{c} \beta_2$ and $\beta_2 = \sqrt{\varepsilon_2 \mu_2 - \varepsilon_1 \mu_1 \text{sen}(\theta_i)}$, ω is the incident light frequency, c is the light velocity in vacuum, ε_1 and μ_1 are the medium parameters at $z < 0$, and θ_i is the incident angle from medium 1 to 2; we also considered an electric transversal light polarization, when the electric field is always on the x-y plane.

For the multilayer case, this relation was used to connect the fields at each adjacent interface. With the equations obtained, it is possible to determine all field amplitudes, considering the incident field amplitude at $z = 0$ as known, and also considering that the last layer only has a transmitted field and not a reflected one.

For the case of plane waves, the total fields on each layer were written in terms of the partial fields as (12) and (13),

$$E_j(z) = E_j^+ e^{ik_j z} + E_j^- e^{-ik_j z} \quad (12),$$

$$H_j(z) = \frac{\beta_j}{\mu_j} E_j^+ e^{ik_j z} - \frac{\beta_j}{\mu_j} E_j^- e^{-ik_j z} \quad (13),$$

where E_j^+ and E_j^- are the light field amplitudes traveling to the right or left, respectively, on the j layer. E_j^+ and E_j^- can be written in terms of the total fields at each interface, and the obtained expression allows us to draw the fields through all the system. For a detailed deduction, see reference [84].

To determine reflectance, $R = \left| \frac{E_R}{E_I} \right|^2$, where E_R is the reflected field and E_I is the incident (known) field, the continuity of the transverse components at $z = 0$ was used,

$$E_R + E_I = E_a \quad (14),$$

$$\frac{\beta_1}{\mu_1} E_I - \frac{\beta_1}{\mu_1} E_R = H_a \quad (15),$$

and from that,

$$R = \left| \frac{\frac{\beta_1}{\mu_1} E_a - H_a}{\frac{\beta_1}{\mu_1} E_a + H_a} \right|^2 \quad (16).$$

In the same manner, transmission can be obtained from the E_T field in the last medium using $T = \left| \frac{E_T}{E_i} \right|^2$.

To calculate absorption at each layer, it was necessary to carry out a balance of energy, and then, the continuity equation was used (equations 6.108 and 6.106 from [85]). The dissipated energy inside one medium is expressed with the term $\int \bar{J} \cdot \bar{E} dV$, where \bar{J} is the current density $\bar{J} = \sigma \bar{E}$, and σ is the material conductivity. After some algebra, absorption at layer j can be determined with

$$A_j = \frac{\varepsilon_j^2 \omega}{4\pi S_i} \int_{Z_j}^{Z_{j+1}} |E_j(z)|^2 dx \quad (17),$$

where Z_j and Z_{j+1} are the layer boundaries, S_i is the incident Poynting vector, and ε_j^2 is the imaginary part of the complex dielectric function at the j layer.

The dielectric function ($\varepsilon = \varepsilon' + i\varepsilon''$) is directly related to the complex refractive index ($n = n' + ik$) through $\varepsilon = n^2$ (from Maxwell equations). Therefore, the real and imaginary parts of the dielectric function are given by $\varepsilon' = n'^2 - k^2$ and $\varepsilon'' = 2n'k$, respectively. The complex refractive index is divided into the real part, the refractive index (n'), and the imaginary part, the extinction coefficient (k). The refractive index is a measure to know how much the velocity of light is reduced when it goes inside a medium, and the extinction coefficient is related to the absorption in a medium. The n' and k values used for TMM can be found elsewhere [86–89] for all layers (ITO, PEDOT:PSS, PFN), except for the PTB7-Th:PC₇₁BM blend film, for which the mentioned parameters were measured here by using an optical thin film analyzer (Filmetrics F20). PTB7-Th:PC₇₁BM films for these measurements were spin-coated over Si substrates with the same concentration and preparation conditions as those for the OPV solutions. Figure 3.8 shows a plot for the n' and k values, determined in this work as a function of the wavelength for the PTB7-Th:PC₇₁BM blend; these values are similar for those reported for the PTB7:PC₇₁BM film [90].

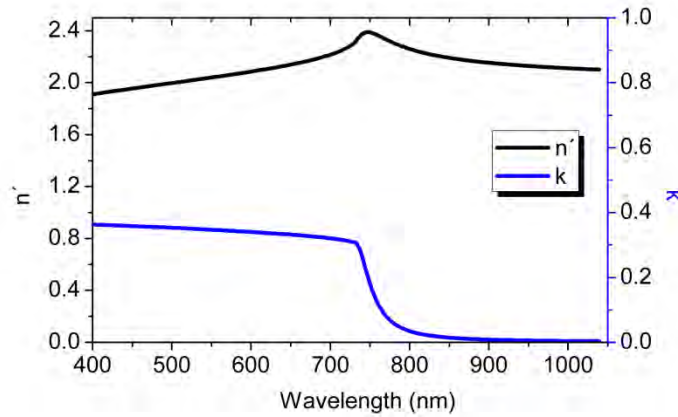


Figure 3.8: Refractive index (black line) and extinction coefficient (blue line) of PTB7-Th:PC₇₁BM blend film.

For the top electrode (FM), the direct sum of the dielectric constants (ε) multiplied by the volumetric fraction (f) of each material (32.5% Bi, 51% In y 16.5% Sn) was used,

$$eff = f_1 * \varepsilon_1 + f_2 * \varepsilon_2 + f_3 * \varepsilon_3 \quad (18),$$

where

$$f_1 + f_2 + f_3 = 1 \quad (19)$$

3.3. Internal Quantum Efficiency (IQE)

Regarding IQE, in 2015, Park et al. [50] reported an analysis of thickness-dependent internal quantum efficiency in OPVs for the PTB7:PC₇₁BM active layer, showing a significant reduction of IQE when increasing active layer thickness (work range: 66-320 nm). In that same year, Huang et al. [91] used an off-center solution fabrication method for PTB7-Th:PC₇₁BM based OPVs, with four different active layer thicknesses, 104, 180, 215 and 230 nm, and an inverted configuration, and they achieved near 100% IQE (at ~ 600 nm). In 2017, Fan et al. [92] studied the charge generation properties of OPVs based on PTB7-Th:PC₇₁BM doped with (1-bromo-4-nitrobenzene (C₆H₄BrNO₂)) through the IQE technique (at just an active layer thickness of 100 nm), indicating that this third component is useful for charge transport and transfer issues. Very recently, Chen et al. [93] used the EQE and IQE techniques to demonstrate an effective method to reach high efficiency in OPVs based on PTB7:PC₇₁BM blend by using a sol-gel-derived ZnO:Al₂O₃ composite layer, which helped to suppress recombination losses and to improve light absorption.

Once the internal absorption spectrum has been obtained through TMM, and EQE measurements have been taken, it is possible to plot IQE curves. IQE is the ratio of the generated and collected charges to the number of absorbed photons at the active layer, as shown in equation (8). With IQE measurements, the electronic and optical properties of cells can be analyzed separately, and thus, they provide relevant information about the solar cell electrical characteristics that cannot be obtained only through EQE [94]. The IQE spectral curve can give information about how efficiently the device convert photons to CCs, or about the CC recombination spatial dependence. The total recombination processes inside an OPV device are inversely related with IQE [94].

Poly[(ethylhexyl-thiophenyl)-benzodithiophene-(ethylhexyl)-thienothiophene] (PBDTTT-EFT) [95,96], commonly called as PTB7-Th or PCE10, is a derivative of poly[[4,8-bis[(2-ethylhexyl)oxy]benzo[1,2-b:4,5-b']dithiophene-2,6-diyl][3-fluoro-2-[(2-ethylhexyl)carbonyl]thieno[3,4-b]thiophenediyl]], known as PTB7 or PCE9, see all the chemical structures used in this work in the scheme showed before Introduction section. For a single OPV BHJ layer device, with this polymer, PCE can be greater than 9% [95,96]. In this work, direct PTB7-Th:PC₇₁BM based OPVs are fully characterized through the IQE technique by using the internal absorption estimated through TMM, when taking into account reflection and interference processes inside the OPV stack, unlike the case of PTB7:PC₇₁BM [50,93] (In reference [93] an inverted configuration is used). To get a deeper understanding of the OPV device performance, in the next chapter, an analysis of the EQE and IQE spectra will be carried out for several active layer thicknesses, based on PTB7-Th polymer, within a range from 40 to 165 nm, as well as a comparison/discussion between the experimentally obtained results and the theoretical simulations through TMM.

4. Device fabrication and experimental results

As a first step in this thesis dissertation, some comparisons between three relatively efficient polymers used in OPVs: two of the most common and low bandgap polymers: PTB7 and PTB7-Th and a relatively novel medium bandgap polymer PBDB-T are presented. Film morphology (through atomic force microscopy (AFM)), film molecular ordering (through scanning tunneling microscopy (STM)), and X-ray diffraction (XRD) issues are commented.

It has been proved that, with the incorporation of a third component in the OPV active layer, usually there exists an enhance in the harvesting solar energy and then in the charge transport and collection at the electrodes, and in some cases, also on lifetime stability; however, it depends on the third compound type and concentration into the active layer [97,98]. Therefore, several strategies for increasing efficiency in ternary OPVs have been carried out. It has been proved a photovoltaic parameters enhancement with the use of a second donor [99,100] or a second acceptor (fullerene or non-fullerene) [19,101]. For instance, isocyanate-treated graphene has been used to dope the active layer, based on P3HT, increasing 59% the conversion efficiency in comparison to the un-doped devices [102]. Also solution processable functionalized graphene (SPFG) was incorporated as a third component in PTB7:PC₇₁BM active layer obtaining a PCE increment of 22% with respect to the reference devices [16]. Cheng et al. [101], used ICBA to provide more routes for charge transfer at the PTB7:PC₇₁BM interface improving the average efficiency from 7.23% to 8.13 %. Wang et al. [103], used the non-fullerene acceptor molecule ITIC (2,2'-[[6,6,12,12-Tetrakis(4-hexylphenyl)-6,12-dihydrodithieno[2,3-d:2',3'-d']-s-indaceno[1,2-b:5,6-b']dithiophene-2,8-diyl]]bis[methyldiyne(3-oxo-1H-indene-2,1(3H)-diylidene)]]bis[propanedinitrile]) with PBDB-T, also named PCE12 (poly[[4,8-bis[5-(2-ethylhexyl)-2-thienyl]benzo[1,2-b:4,5-b']dithiophene-2,6-diyl]-2,5-thiophenediyl[5,7-bis(2-ethylhexyl)-4,8-dioxo-4H,8H-benzo[1,2-c:4,5-c']dithiophene-1,3-diyl]]), and PC₇₁BM to form efficient electron-transport pathways and, they reached a PCE of 10.2% compared to 9.2% and 8.1% for the binary PBDB-T:ITIC and PBDB-T:PC₇₁BM devices, respectively. The addition of magnetic oxide nanoparticles in OPVs P3HT:PC₇₀BM active layer has improved the lifetime and stability of these devices with an efficiency of ~ 3% [104]. On the other hand, 5 wt % of Fe₃O₄ nanoparticles (NPs), as doping agent into the P3HT:PCBM blend, increased conversion efficiency from 1.09% to 2.22% [105]. Lin et al. [106], reported a PCE increment from 2.08% to 2.3% with

the incorporation of small amounts of FeS₂ nanocrystals (NCs) (0.3 wt. %) into P3HT:PC₇₁BM active layer. Besides, Khan et al. [107], added 20 wt. % of FeS₂ quantum dots (with ~ 5 nm size) and reached a PCE of 3.62% compared to the reference device (2.32%). Then, as a second step in this work, non-toxic iron sulfide (FeS₂) nanocrystals (NCs) was used as a second electron-acceptor in PTB7:PC₇₁BM active blend with the configuration ITO/PEDOT:PSS/PTB7:PC₇₁BM:FeS₂/PFN/FM. FeS₂ NCs had been used with the purpose to enhance efficiency by improving dissociation and charge transport. Ternary active layers were prepared by blending small amounts of the semiconducting FeS₂ NCs at different weight ratios: 0.0, 0.25, 0.5, and 1.0 wt. %, with respect to the electron donor PTB7.

As a third step, PTB7-Th:PC₇₁BM solar cells with an active layer thicknesses varying from 40 to 165 nm were made under direct configuration ITO/PEDOT:PSS/PTB7-Th:PC₇₁BM/PFN/FM. An analysis of the external and internal quantum efficiency of the devices fabricated was carried out. A comparison between the experimental measurements and theoretical simulations (by TMM) was discussed in order to have better understanding of the OPVs performance.

PEDOT:PSS, as mentioned before, is widely used as HTL. However, it has several limitations, the chemical interaction between PEDOT:PSS and ITO cause the ITO corrosion due to the PEDOT:PSS acidity due to the polystyrene sulfonic acid (PSS), and also, the hydroscopic nature of PEDOT:PSS eventually reduces the device performance [108]. For this reason, 2-dimensional carbon based materials such as graphene oxide (GO) have been extensively used as HTLs. Graphene shows stable aqueous dispersion [109], possess excellent intrinsic properties, such as high thermal conductivity, transparency, and high electrical charge mobility [110,111]. Therefore, as a final step in this work, PBDB-T:ITIC and PBDB-T:PC₇₁BM binary solar cells were fabricated, reaching 8.9% and 6.9% respectively. Then, PBDB-T:ITIC based OPVs were tested with fluorinated reduced graphene oxide (F-rGO) as HTL and as a bilayer with the combination of PEDOT:PSS.

4.1. Donor polymers comparisons: PTB7, PTB7-Th and PBDB-T

Main difference between PTB7, PTB7-Th and PBDB-T polymers is their absorption spectra. In Figure 4.1 are shown low bandgap polymers PTB7, PTB7-Th and medium bandgap polymer PBDB-T absorption spectra. PTB7 and PTB7-Th polymers spectra are shifted to red compared

with PBDB-T spectrum: bandgap of PTB7-Th (1.58 eV) is smaller than that for PTB7 (1.64 eV) and at the same time, these two bandgaps, are smaller than that of PBDB-T (1.8 eV) [112,113]. Thus, OPVs devices based on PTB7-Th could enhance the photon absorption and can potentially have a better charge generation. Also, on the chemical structure of PTB7, it was replaced two oxygen atoms for two thiophene units to obtain PTB7-Th, with these modifications it was improved the planarity of the main chain and the polymer stability [112]. The absorption coefficient (α) of the active layers PTB7:PC₇₁BM, PTB7-Th:PC₇₁BM and PBDB-T:ITIC, at 485 nm, is around $1.9 \times 10^4 \text{ cm}^{-1}$, $2.5 \times 10^4 \text{ cm}^{-1}$ and $3.4 \times 10^4 \text{ cm}^{-1}$ respectively [114,115]. See Table 4.1.

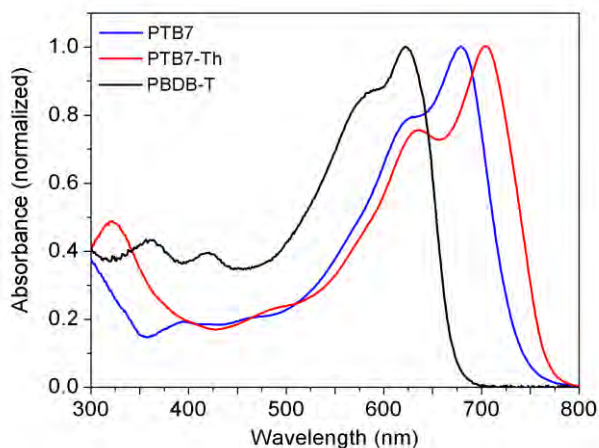
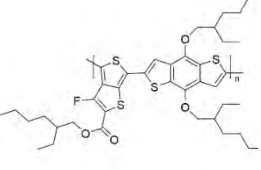
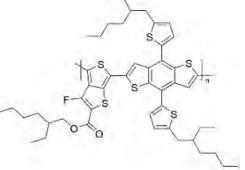
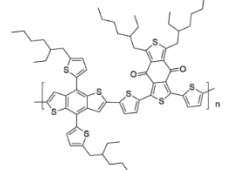


Figure 4.1: PTB7, PTB7-Th and PBDB-T absorption spectra in solution.

Table 4.1: Comparative data of the PTB7, PTB7-Th and PBDB-T donor polymers

Parameters:	PTB7	PTB7-Th	PBDB-T	References
Chemical structure				
Also named	PCE9	PCE10	PCE12	
LUMO	-3.3 eV	-3.66 eV	-2.92 eV	[16,116]
HOMO	-5.2 eV	-5.24 eV	-5.33 eV	[16,116]
^a Hole mobility	$5.8 \times 10^{-4} \text{cm}^2 \text{V}^{-1} \text{s}^{-1}$	$2.83 \times 10^{-3} \text{cm}^2 \text{V}^{-1} \text{s}^{-1}$	$1 \times 10^{-4} \text{cm}^2 \text{V}^{-1} \text{s}^{-1}$	[117–119]
^b Bandgap	1.64 eV	1.58 eV	1.8 eV	[112,113]
^a Absorption coefficient	$1.9 \times 10^4 \text{cm}^{-1}$	$2.5 \times 10^4 \text{cm}^{-1}$	$3.4 \times 10^4 \text{cm}^{-1}$	[114,115]
^c Chain thickness	~ 900 pm to 1 nm	~ 1.5 nm to 1.7 nm	~ 600 to 700 pm	This work
^c Chain separation	~ 960 pm	~730 pm	~ 700 pm	"
^a Roughness	~ 0.6 nm	~ 1.6 nm	~ 2.9 nm	"
Best PCE	6.89 %	7.65 %	8.87 %	"

^a On film, ^b Optical (on film), ^c From STM measurements

A series of measurements were carried out to compare PTB7, PTB7-Th and PBDB-T polymer films. For film thickness and morphology, it was used an AFM (Easyscan2 from Nanosurf) operated in contact mode employing cantilever tips with aluminum reflective coating (ContAl-G) from BudgetSensors. When operating in tapping mode by using cantilever tips PPP-NCLAu with a metallic layer (Au), phase contrast and topography images of the layers were acquired; measurements were performed under ambient conditions. For these AFM measurements, sample films were prepared under the same OPVs fabrication procedure (without PFN neither FM); active layer thickness was ~100 nm. In Figure 4.2 are shown the AFM topography images (top) and phase contrast images (bottom) (with $5 \mu\text{m} \times 5 \mu\text{m}$ scanning size) of: (a) PTB7, (b) PTB7-Th and (c) PBDB-T films; (d) PTB7:PC₇₁BM, (e) PTB7-Th:PC₇₁BM blends (ratio 1:1.5 wt %) with 3 % of DIO and (f) PBDB-T:ITIC (ratio 1:1 wt % with 0.5 % of DIO). Roughness values: (a) 0.6 nm, (b) 1.6 nm, (c) 2.9 nm, (d) 0.9 nm, (e) 2 nm and (f) 2.5 nm. For the case of PTB7-Th based films (b and e), the roughness increment is about 1 nm compared with the PTB7 cases (a and d); it may be due to the fact that PTB7-Th polymer film has thicker chains (~ 0.7 nm thicker, see Table 4.1) as commented below from STM measurements. Also, domains shown in Figure 4.2e (PTB7-Th) are

larger than those in Figure 4.2d (PTB7), which could be for the same above explained reason. For the PBDB-T:ITIC case (f), domains are larger and less spaced compared with the other two cases (d and e) and can be due to the chemical structure and chains thickness and separation (which are lesser for this polymer (~ 700 pm)) differences between PBDB-T and the other two polymers (see Table 4.1). These fact could improve CCs dissociation and transport. Also, PBDB-T HOMO is about 0.1 eV deeper compared with the similar HOMO of PTB7-Th and PTB7 (see Table 4.1), which can lead to higher OPVs V_{oc} [116].

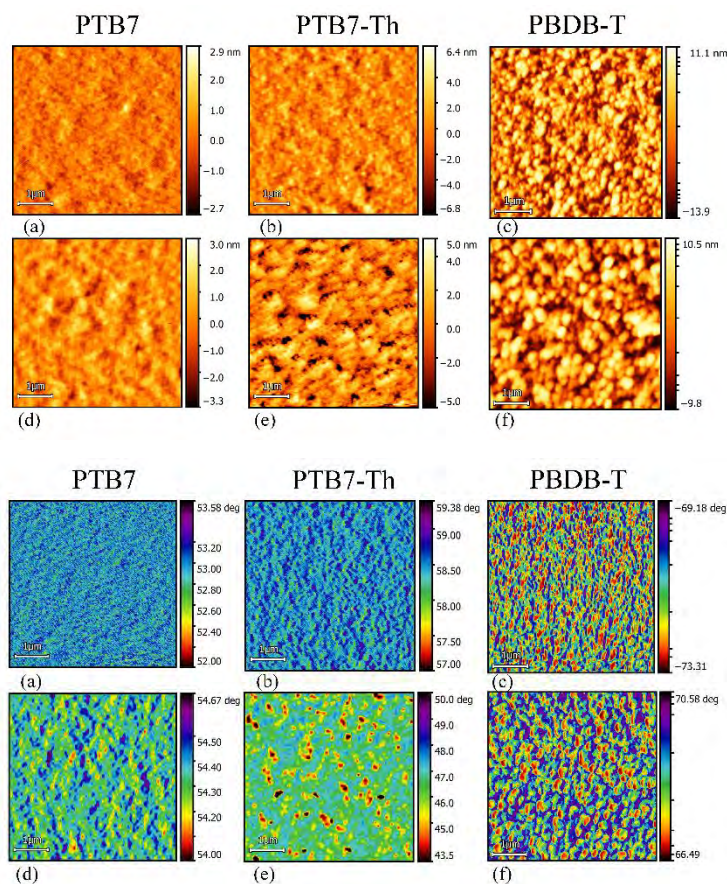


Figure 4.2: AFM topography (top, traditional color map) and phase contrast (bottom, spectral color map) images of (a) PTB7, (b) PTB7-Th, (c) PBDB-T, (d) PTB7:PC₇₁BM with DIO, (e) PTB7-Th:PC₇₁BM with DIO, (f) PBDB-T:ITIC with DIO. For all cases, bar scale = 1 μ m. As surface is relatively smooth, spectral color map provides better details.

PTB7, PTB7-Th and PBDB-T films (monolayers) were analyzed with STM to study their film molecular ordering at the nanoscale regime. For these latter measurements, PTB7, PTB7-Th and PBDB-T were dissolved in 1-phenyloctane with 3% of 1,8-diiodooctane (DIO) with a concentration of 0.1 mg/ml and deposited on highly ordered pyrolytic graphite (HOPG) surface by drop casting. Electrochemically etched and mechanically cut Pt-Ir wires were used as STM tips.

Before each film deposition, HOPG substrates were cleaved by using the adhesive tape technique to obtain an atomically clean surface; then, a droplet (about 2 μl) of 1-phenyloctane was directly deposited between the tip and the sample surface to make the liquid/solid interface for STM measurements. Sample thicknesses for STM measurements were less than 1 nm (about 300 pm according to an image profile that was taken and analyzed through Gwyddion open source software (v. 2.49)) Figure 4.3 shows the STM images, here are seen worm-like chains at two different scales for PTB7: (a) and (d); for PTB7-Th: (b) and (e); and for PBDB-T: (c) and (f). The scan size, the tunneling current (I_t) and the applied potential (U) were: for (a) 6 nm \times 6 nm, $I_t = 121$ pA and $U = 950$ mV, (b) 6 nm \times 6 nm, $I_t = 121$ pA and $U = 1.25$ V, (c) 5 nm \times 5 nm, $I_t = 200$ pA and $U = 0.9$ V, (d) 38 nm \times 38 nm, $I_t = 201$ pA and $U = 850$ mV, (e) 40 nm \times 40 nm, $I_t = 161$ pA and $U = 1.35$ V and (f) 20 nm \times 20 nm, $I_t = 120$ pA and $U = 1.15$ V.

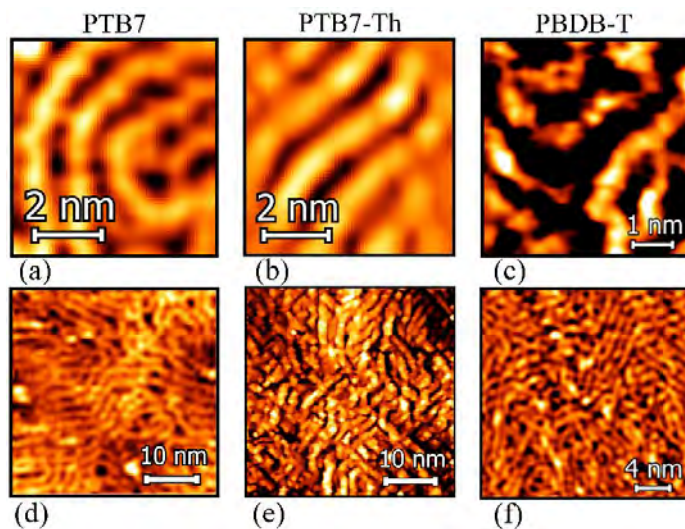


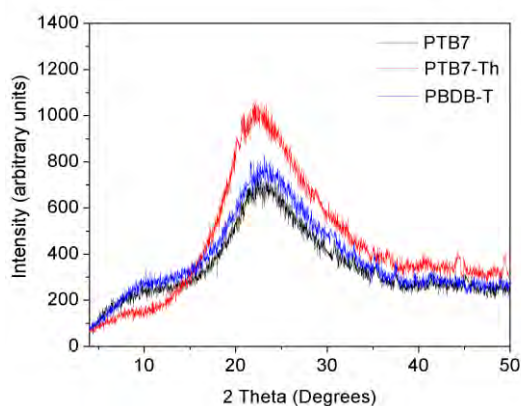
Figure 4.3: STM images showing worm-like chains of (a) PTB7 and (b) PTB7-Th with 6 nm \times 6 nm scan size, (c) PBDB-T with 5 nm \times 5 nm scan size, (d) PTB7 with 38 nm \times 38 nm scan size, (e) PTB7-Th with 40 nm \times 40 nm scan size and (f) PBDB-T with 20 nm \times 20 nm scan size.

From Figure 4.3 can be observed amorphous domains in the three polymers measurements; separations for PTB7 chains are a little larger (~ 960 pm) than for PTB7-Th chains (~ 730 pm) and for PBDB-T chains (~ 700 pm). Besides, thickness of PTB7-Th chains are thicker (~ 1.5 nm to 1.7 nm) than those for PTB7 chains (~ 900 pm to 1 nm) and for PBDB-T chains (~ 600 pm to 700 pm). Maybe, these differences could be due to the already commented chemical structure modifications of PTB7 polymer to get the PTB7-Th one, i.e., the replaced two oxygens for the two thiophene units [112]. The worm-like chains of PBDB-T, where the prolonged π system allows the polymer to form a better π - π stacking with an interchain distance around ~ 450 pm and a shorter

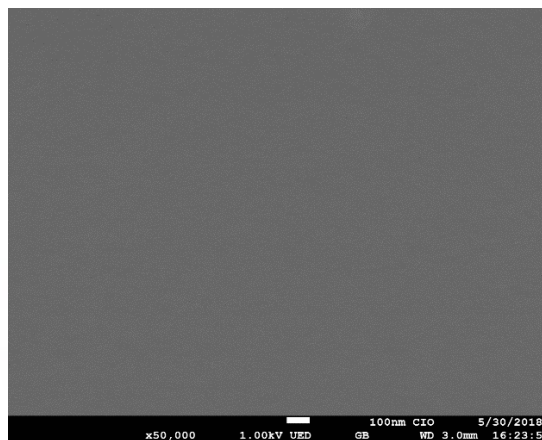
distance of ~ 700 pm between different polymer backbone chains can influence PCE (Figure 4.3c and f). This short distance between PBDB-T chains could facilitate a more efficient intramolecular charge separation, and thus improve the charge transfer from the active layer to the OPV electrodes.

XRD experiments were performed for 2θ in the range of $4\text{--}50^\circ$ by using incremental steps of 0.02° ; these measurements were carried out in an ambient atmosphere. Figure 4.4a shows the XRD patterns for PTB7, PTB7-Th and PBDB-T films. It is observed, in all patterns, the (010) plane formation indicating the π - π stacking with a face-on orientation [120,121]. The polymer films show the maximum peak between 22° and 23° , which is in good agreement with previous literature [121–123]. The higher intensity for the PTB7-Th pattern could indicate that has a better organized structure (packing of the chains) and higher co-planarity than the PTB7 and PBDB-T films [114,121]. Also, the maximum intensity value for PTB7 is in 22.4° , for PTB7-Th is in 22.7° and for PBDB-T is in 23.24° ; these small shifts could correlate with the smaller chain separation (d-spacing) in PTB7-Th films than the d-spacing in PTB7 layers and in the same manner PBDB-T has less d-spacing than PBT7 and PTB7-Th [121,122], see STM analysis in Figure 4.3 and Table 4.1.

Figure 4.4b, c and d show SEM images for PTB7:PC₇₁BM, PTB7-Th:PC₇₁BM and PBDB-T:ITIC layers, respectively (bar scale is 100 nm). Films are very homogenous and smooth, it correlates with the small films roughness values determined from AFM measurements: from 0.5 nm to 3 nm. For the PBDB-T case (d) an uniform fibrillar structure (interpenetrating network) can be observed, which could provide more homogeneous pathways, compared with the other two, helping CCs dissociation and transport in the active layer and diminishing exciton CCs recombination [124].



a)



b)

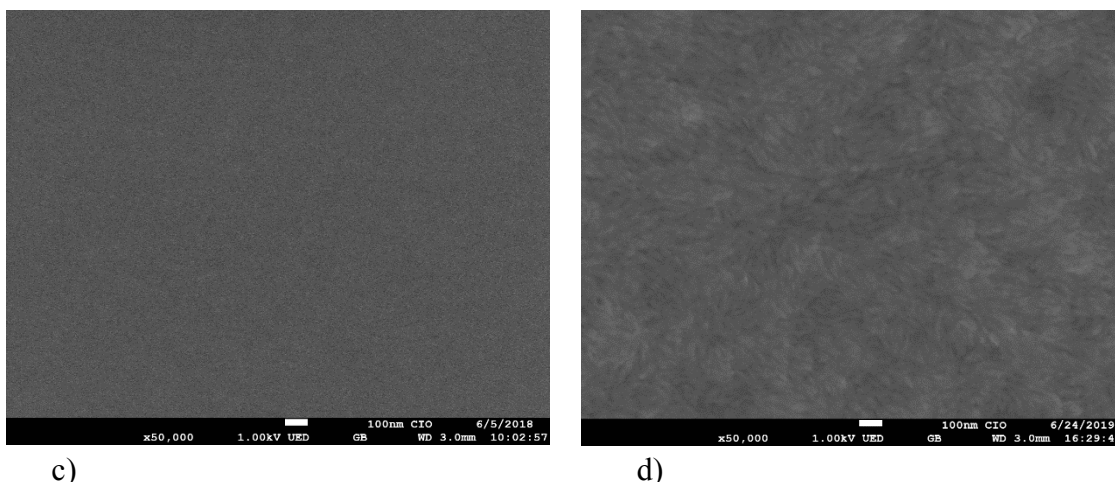


Figure 4.4: (a) XRD pattern of PTB7 (black line), PTB7-Th (red line) and PBDB-T (blue line) films, (b), (c) and (d) SEM images for PTB7:PC₇₁BM, PTB7-Th:PC₇₁BM and PBDB-T:ITIC films, respectively; surface is relatively smooth.

Conclusions of section 4.1

STM and XRD determinations indicate that PTB7-Th film chains are somewhat thicker and less spaced than those for PTB7 and also that, PTB7-Th films have a slightly better ordering and higher co-planarity, and thus, providing a possible better electrical charge transport; these facts could help to better understand the PV performance and stability in OPVs cells based on PTB7-Th than those based on PTB7. Otherwise, PBDB-T polymer, showing a worm-like pattern in a monolayer film with an interchain distance around ~450 pm and a shorter distance of ~700 pm between different polymer backbone chains, could facilitate a more efficient intramolecular charge separation and thus improve the charge transfer from the active layer to the OPV electrodes, due to the short distance between chains. Also, PBDB-T:ITIC uniform fibrillar structure and their domains larger and less spaced, could provide homogeneous pathways, helping CCs dissociation and transport and diminishing exciton CCs recombination. To the best of our knowledge this is the first time that these three polymers are compared between them.

4.2. PTB7: Iron sulfide nanocrystals as second electron-acceptor

Iron disulfide (FeS₂) is a natural earth-abundant and non-toxic material with possible applications in different areas such as lithium batteries, transistors and photovoltaic (PV) devices [125,126]. According to the analysis carried out by Wadia et al. [127], among 23 semiconductors, it is the best candidate for large-scale solar cells development at a low cost ($< 2 \times 10^{-6}$ €/W). Pyrite FeS₂ presents excellent optoelectronic properties: direct band gap (0.8 to 1.38 eV) [128–132], high

optical absorption coefficient ($2 \times 10^5 \text{ cm}^{-1}$) [128], high electron mobility (2 to $80 \text{ cm}^2/(\text{Vs})$) [128,133] and large charge carrier lifetime (200 ps) [134], therefore FeS_2 nanoparticles (NPs) could be a good alternative for PV applications [135]. Pyrite semi-spherical NCs were added as a second electron-acceptor, at different concentrations, into the active layer PTB7:PC₇₁BM of OPVs fabricated with the direct configuration glass/ITO/PEDOT:PSS/PTB7:PC₇₁BM:FeS₂/PFN/FM (as shown in Figure 4.5a). Figure 4.5b shows the chemical structure of PC₇₁BM ([6,6]-phenyl-C₇₁-butyric acid methyl ester).

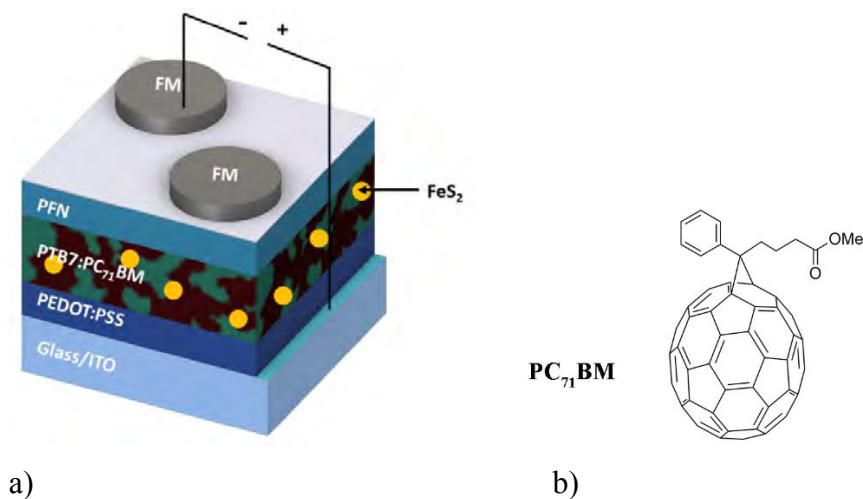


Figure 4.5: (a) OPV structure; (b) Chemical structure of PC₇₁BM.

Sample preparation and characterization

All chemicals were used as received without further purification. For OPVs fabrication, ITO covered glass substrates ($10 \text{ } \Omega/\text{sq}$, $\sim 165 \text{ nm}$ thickness) were purchased, from Delta Technologies, PEDOT:PSS (Clevios PVP AI 4083) was acquired from Heraeus and, PTB7 and PC₇₁BM from 1-Material Inc, PFN from 1-Material Inc and FM from Rotometals.

FeS_2 NCs were prepared using the hot two-pot method [136]. Iron II chloride (0.5M) and sulfur (0.57M) precursors were used to obtain the FeS_2 NCs. The iron precursor was dissolved with octadecylamine at 120°C for 1 h under argon atmosphere. Sulfur was dissolved with diphenyl ether at 70°C for 1 h under argon gas. Then sulfur-diphenyl ether solution was added in the iron-octadecylamine complex. The solution was heated up at 220°C for 2 h. Once the reaction is finished, the product was cooled down to 110°C , subsequently 5 ml of chloroform was added and kept at room temperature; finally, 35 ml of methanol were added to purify the product by

centrifugation, this step was repeated several times. The final product was re-dispersed in chloroform for the posterior active layer fabrication.

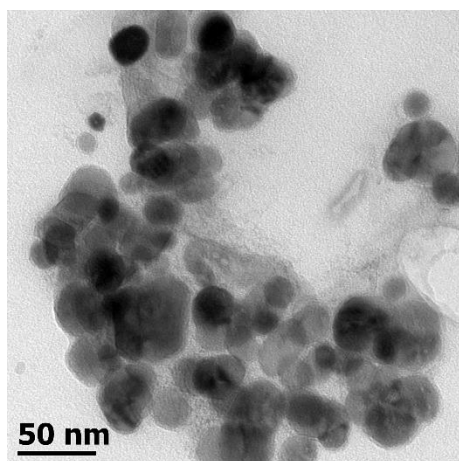
Solution for the active layer was prepared by dissolving PTB7 and PC₇₁BM at 1:1.5 w/w, 30 mg/ml in anhydrous chlorobenzene (CB):1,8-diiodooctane (DIO) (97:3 v/v) within a glovebox under nitrogen atmosphere. Solution was stirred in a hot plate for about 24 h at room temperature. FeS₂ NCs were added to the active layer at 0, 0.25, 0.5, 1.0 wt. % with respect to the electron donor and then mixed in an ultrasonic bath for 20 minutes. OPVs devices were fabricated as follows (Figure 4.5a): after ITO substrates were cleaned and dried, a PEDOT:PSS layer of ~ 40 nm thickness was spin-coated at 4500 rpm for 1 minute on top of the ITO substrate and then it was 120 °C thermally treated for 20 minutes. The active layer with and without FeS₂ was spin coated on ITO/PEDOT:PSS at 1900 rpm for 60 s at normal room conditions and then a thermal annealing of 80 °C for 15 minutes was provided to the deposited films (~ 100 nm). A PFN layer (~ 5-10 nm) was spin-coated at 6000 rpm on top of the active layer and exposed to thermal annealing for 15 minutes at 80 °C. Active area (0.07 cm²) was delimited with a Scotch tape. FM top electrode was deposited (after melting it at 95 °C in a hot plate) by drop casting on top of the PFN layer following the procedure previously reported [63]. The final device structure is: glass (1.1 mm)/ITO (~165 nm)/PEDOT:PSS (~40 nm)/PTB7:FeS₂:PC₇₁BM (~100 nm)/PFN (~5 nm)/FM.

TEM images were taken with a JEOL JEM-1010 with an acceleration potential of 80 kV. For STM measurements, FeS₂ were suspended in chlorobenzene with a concentration of 0.2 mg/ml and deposited on highly ordered pyrolytic graphite (HOPG) surface by drop casting. For CV measurements: the working electrode was an ITO electrode; the reference electrode was Ag⁺/Ag⁰ (0.01 M AgNO₃/0.1 M tetrabutylammonium perchlorate in acetonitrile) and the counter electrode was platinum. All CV measurements were carried out in dry acetonitrile using 0.1 M tetrabutylammonium hexafluorophosphate (TBAPF₆) as electrolyte at a scan rate of 100 mVs⁻¹, and each solution was purged with N₂ prior to measurement. UV-Vis characterization was performed through thin films of PTB7:PC₇₁BM active layer, with and without FeS₂ NCs at different concentrations (0, 0.25, 0.5 and 0.1 wt.%), spin coated on a corning glass at 1900 rpm for 60 s in order to obtain similar thickness (~ 100 nm). The active layer thickness was measured with the AFM operated in contact mode employing cantilever tips with aluminum reflective coating (ContAl-G) from BudgetSensors. AFM height (roughness) images were acquired in dynamic force

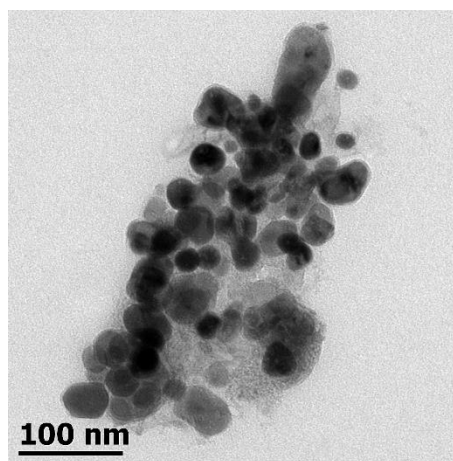
mode (using PPP-NCLAu from NanoSensors), which has better resolution than the contact mode [137]. For these AFM measurements, sample films were prepared under the same OPVs fabrication procedure (without PFN neither FM). A potentiostat/galvanostat PARTAT 2273 system was used for IS measurements. The impedance spectra were measured (in ambient atmosphere, at room temperature) under dark and illumination conditions using a frequency range from 1 to 500 kHz with an amplitude of 20 mV. The curves were simulated with ZView software [63].

OPVs results

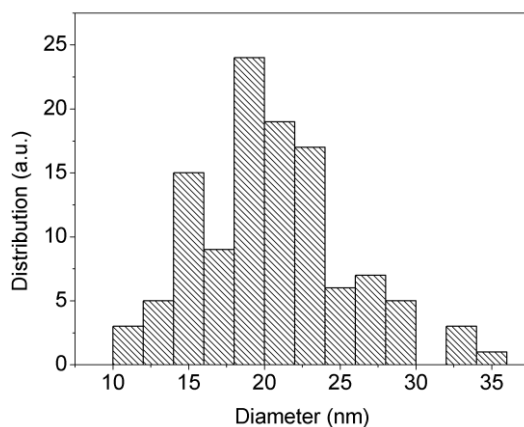
The diluted dark product of FeS₂ was observed by Transmission Electron Microscopy (TEM) (Figure 4.6a and b). Semispherical NCs, with an average size of 20 nm ± 4 nm, were observed. Distribution of the NCs size was determined from the *Image J software* (Figure 4.6c). X-ray pattern (reported in our previous work [136]) of these NCs, showed peaks at 2θ= 28, 33, 37, 40.7, 47.5, 56, 61.5, 64.5 °, corresponding to the pyrite crystalline phase (pyrite JCPDS (Joint Committee on Powder Diffraction Standards) card), which is in good agreement with the reported cubic morphology [138].



a)



b)



c)

Figure 4.6: (a) and (b) TEM morphology of FeS_2 NCs at 50 and 100 nm scale bar, respectively and, (c) distribution of NCs sizes.

FeS_2 thin films were analyzed with STM to study their film molecular ordering at the nanoscale regime. Figure 4.7a shows the STM image. The scan size, the tunneling current (I_t) and the applied potential (U) were: $50 \text{ nm} \times 50 \text{ nm}$, $I_t = 500 \text{ pA}$ and $U = 450 \text{ mV}$, respectively. Scanning Electron Microscopy (SEM) image of agglomerated FeS_2 NCs is shown in Figure 4.7b. In these TEM (Figure 4.6a and b), STM (Figure 4.7a) and SEM (Figure 4.7b) images can be appreciated that the size of the NCs are in the nanoscale regime (~ 15 to 25 nm) as stated previously.

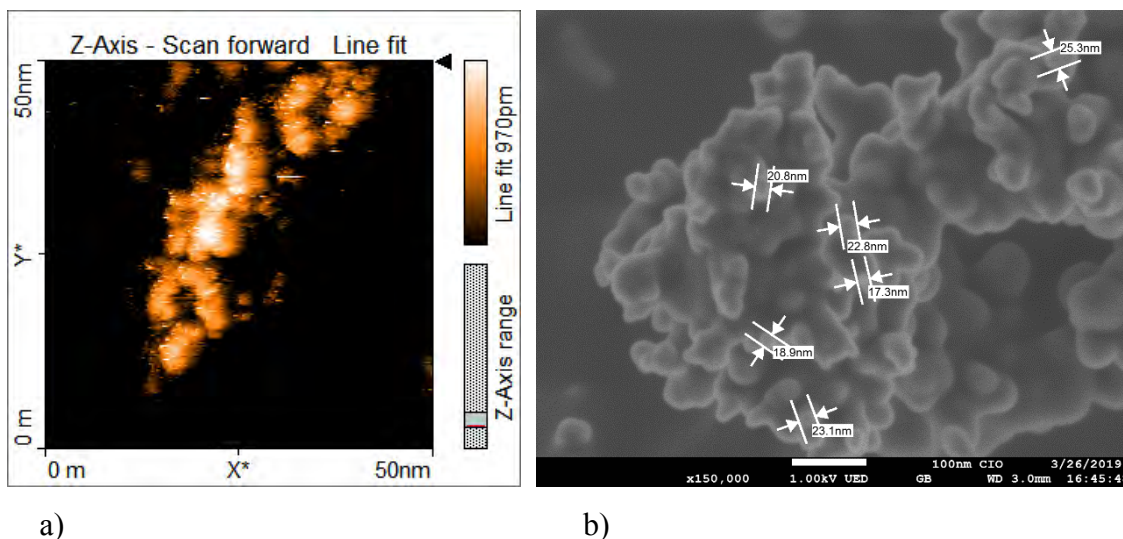


Figure 4.7: (a) STM image of FeS_2 deposited on HOPG substrate (thickness $\sim 20 \text{ nm}$) with $50 \text{ nm} \times 50 \text{ nm}$ scan size and (b) SEM image of FeS_2 NCs (scale bar = 100 nm).

Energy levels of FeS_2 NCs were characterized by CV, Figure 4.8a shows the cyclic voltammogram. For the CV measurements the working electrode was an ITO electrode; the

reference electrode was $\text{Ag}^+/\text{Ag}^\circ$ (0.01 M AgNO_3 /0.1 M tetrabutylammonium perchlorate in acetonitrile) and the counter electrode was platinum. All CV measurements were carried out in dry acetonitrile using 0.1 M tetrabutylammonium hexafluorophosphate (TBAPF_6) as electrolyte at a scan rate of 100 mVs^{-1} , and each solution was purged with N_2 prior to measurement. It shows an oxidation peak, i.e., the ionization potential at approximately +0.39 V and a reduction peak, i.e., the electron affinity at about -0.40 V. In order to estimate the electrochemical band gap energy, the valence and band conduction energies (E_{VB} and E_{CB} , respectively) were calculated through the following Equation (20) and (21):

$$E_{\text{VB}} = -\left(E_{[\textit{onset,ox}]} - E_{[\frac{1}{2}(\textit{Fc})]} + 4.8\right) \text{ eV} \quad (20)$$

and

$$E_{\text{CB}} = -\left(E_{[\textit{onset,red}]} - E_{[\frac{1}{2}(\textit{Fc})]} + 4.8\right) \text{ eV} \quad (21)$$

where $E_{[\textit{onset,ox}]}$ and $E_{[\textit{onset,red}]}$ are onset potentials of the oxidation and reduction relative to the ferrocene/ferrocenium (Fc^+/Fc), $E_{[\frac{1}{2}(\textit{Fc})]}$ (half-wave ferrocene potential) is 0.20 V, the value 4.8 eV represents the difference between the vacuum level potential of the normal hydrogen electrode. Thus, a E_{VB} of -4.99 eV and an E_{CB} of -4.20 eV, respectively, were determined resulting in a suitable energy band gap of 0.79 eV, which is close to the reported range [128–132]. Figure 4.8b shows the energy levels diagram of all used materials in the device structure. FeS_2 could improve OPVs performance as a second acceptor by charge carriers pathways generation and cascade like formation in the energy levels of the active layer materials (as shown in the diagram) [16]. Perhaps charges might travel through three different pathways: PTB7- FeS_2 , PC_{71}BM - FeS_2 and PTB7- PC_{71}BM [101]. These characteristics can help to a better exciton dissociation, charge transport and collection processes and indeed, to the overall PCE value.

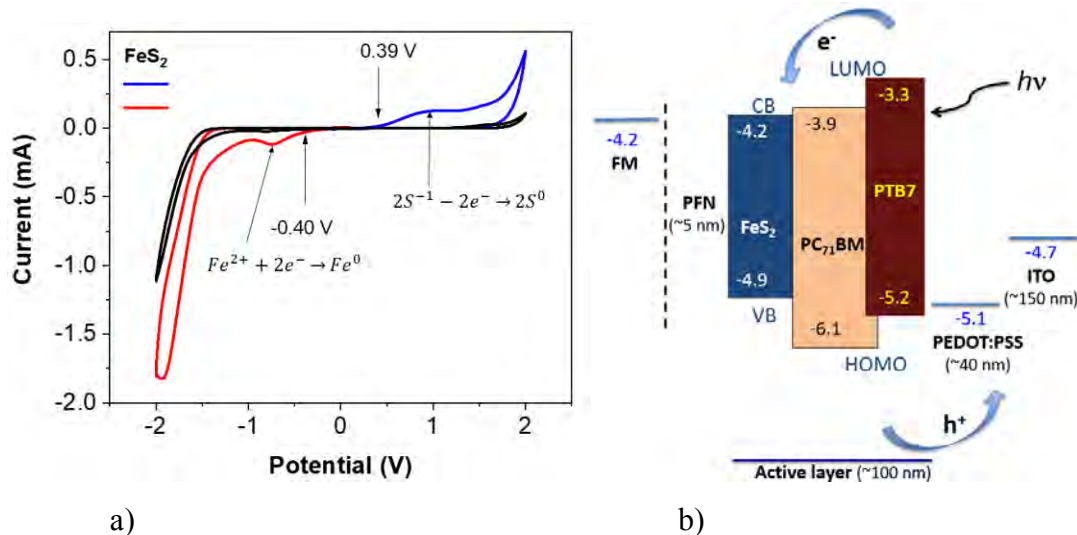


Figure 4.8: (a) Cyclic voltammograms of ITO (reference, black) and FeS_2 NCs in acetonitrile with TBAPF_6 0.1 M at 100 mV s^{-1} (Blue: Anodic zone, Red: Cathodic zone), (b) Flat energy levels diagram of the used organic materials as well as FeS_2 for OPVs fabrication [16].

Figure 4.9 shows UV-Vis absorption spectra of OPVs active layer with different concentrations of FeS_2 , as well as its alone absorption (also in film). The optical absorption of PTB7:PC₇₁BM active layer presents a broad absorption in the visible range (300 to 750 nm). In all absorbance spectra PTB7 peaks appear at 630 and 700 nm and PC₇₁BM peaks in 375 and 480 nm as reported elsewhere [139]. FeS_2 NCs do not contribute to the absorption spectra neither to light harvesting due to the low amount added to the PTB7:PC₇₁BM active layer [106]. Then, difference in absorption of the active layer could be to slight difference in sheet thicknesses as well as to some light dispersion due to optical quality.

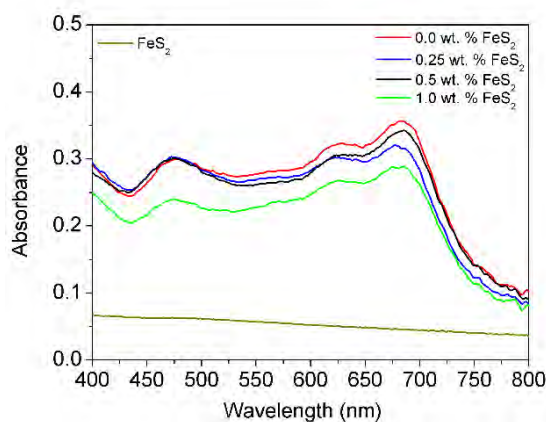


Figure 4.9: UV-Vis absorption of the blend PTB7:PC₇₁BM with different FeS_2 concentrations: 0.0 wt. %, 0.25 wt. %, 0.5 wt. %, 1.0 wt. %.

Figure 4.10a shows J - V plots of OPVs with 0, 0.25, 0.5 and 1 wt. % of FeS_2 as third component in ternary active layer. For OPVs with 0.5 wt. % of FeS_2 , a PCE of 6.47% was reached (with reference devices: 0 wt. %, PCE of 5.69%) and it was mainly due to a J_{sc} and FF increment (V_{oc} remains nearly the same). For each FeS_2 concentration, three different OPVs sets were fabricated and tested, results followed the same trend; Figure 4.10a shows the best values. EQE plots of OPVs reported in Figure 4.10a are shown in Figure 4.10b. EQE curves indicate that the generated photocurrent is reached mainly in the 400 - 750 nm range, which correlate to the PTB7:PC₇₁BM blend absorption. EQE for devices with 0.5 wt. % of FeS_2 is higher than that for the reference OPVs cells, this fact can be attributed to a better charge separation (exciton dissociation enhancement), transport and collection in devices [16]. In other words, exciton recombination reduction can take place while having additional electron charge pathways in the active layer; further, a better charge-balance (free holes/electrons) could also be presented and thus, improving the overall OPVs performance.

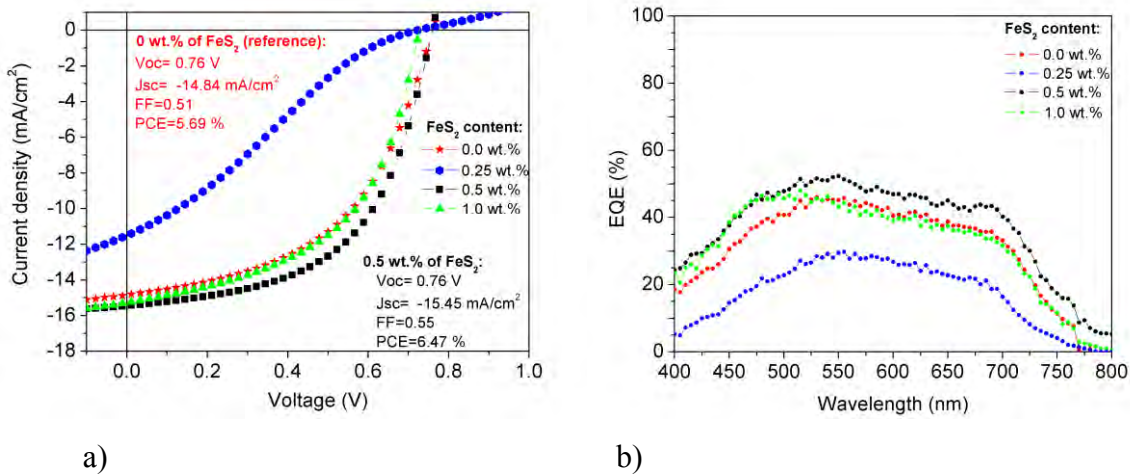


Figure 4.10: (a) J - V curves and (b) EQE of PTB7:PC₇₁BM based devices with different concentrations of FeS_2 : 0.0 wt. %, 0.25 wt. %, 0.5 wt. %, 1.0 wt. %.

The averaged PV parameters of the fabricated OPVs, with different amounts of FeS_2 , are shown in Table 4.2. For PCE, numbers in parentheses are the best values and standard deviations are also shown (in the literature, normally, PCE is the one that present the standard deviation because the other parameters are related with PCE). The best average efficiency (6.02 %) is for 0.5 wt. % of FeS_2 added into PTB7:PC₇₁BM as explained before. On the contrary, for 0.25 wt. % of FeS_2 exists a significant decrement in PV parameters (PCE= 1.57 %) compared to the reference OPVs (average PCE= 4.98 %).

Table 4.2: Average PV parameters of OPVs sets ($n=3$) with different FeS₂ content in the active layer. For PCE, numbers in parentheses are the best values and standard deviations are also shown.

FeS ₂ wt. %	Thickness (nm)	Voc (V)	FF	Jsc (mA/cm ²)	PCE (%)	Roughness (nm)
0.0	101	0.73	0.48	14.48	4.98±0.53 (5.69)	1.1
0.25	109	0.64	0.23	11.15	1.57±0.52 (2.09)	1.4
0.5	110	0.75	0.52	15.31	6.02±0.31 (6.47)	1.7
1.0	106	0.74	0.51	15.21	5.48±0.71 (5.97)	3.2

As shown in Figure 4.10a, OPVs with 0.25 wt. % of FeS₂ exhibit an S-shape type, this behavior could be due to charge recombination or accumulation as a consequence of poor charge's transport between OPV interfaces [140], or/and due to a poor quality of the BHJ active layer [141]. This S-curve shows a linear zone (low fill factor) attributed to a large serial resistance, which, perhaps, it could be attributed to the poor and irregular distribution (accommodation) of FeS₂ isolated NCs into the active blend at this low concentration (0.25 wt. %) inducing a reduction in Jsc and FF, and thus in the overall PCE, see SEM images in Figure 4.13 below. Also, PCE starts to decrease for OPVs with 1 wt. % of FeS₂ (5.48 %) and it could be due to the presence of FeS₂ agglomerates into the active layer. Figure 4.11 shows AFM images in non-contact mode in 2D (left) and 3D (right) of OPVs with different concentrations of FeS₂ (0.0 wt. %, 0.25 wt. %, 0.5 wt. % and 1.0 wt. %). Roughness has a tiny gradual increment as FeS₂ concentration increases (See Table 4.2 and Figure 4.11), which could create traps for charge carriers and to enlarge the leakage current. Because of these agglomerates, OPVs parameters start to decrease, free charges cannot be efficiently extracted; it is mainly observed for OPVs cells with 1 % of FeS₂ (See Figure 4.11 and 4.13d).

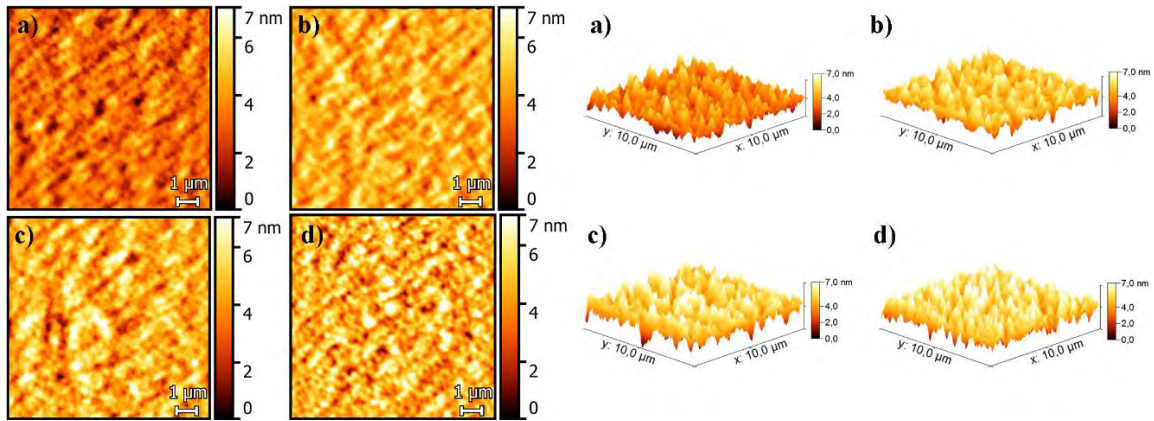


Figure 4.11: AFM images in non-contact mode in 2D (left) and 3D (right) of OPVs with different concentrations of FeS_2 : (a) 0.0 wt. %, (b) 0.25 wt. %, (c) 0.5 wt. % and (d) 1.0 wt. %.

Figure 4.12 shows a SEM image of an OPV layers cross-section, it is observed the thickness of each layer: ITO ~ 197 nm, PEDOT:PSS ~ 40 nm and PTB7:PC₇₁BM active layer ~ 113 nm, which acceptably correlate with sheet thicknesses determined from AFM in contact mode. Also, a zoom of the active layer with non-NCs is presented in Figure 4.12.

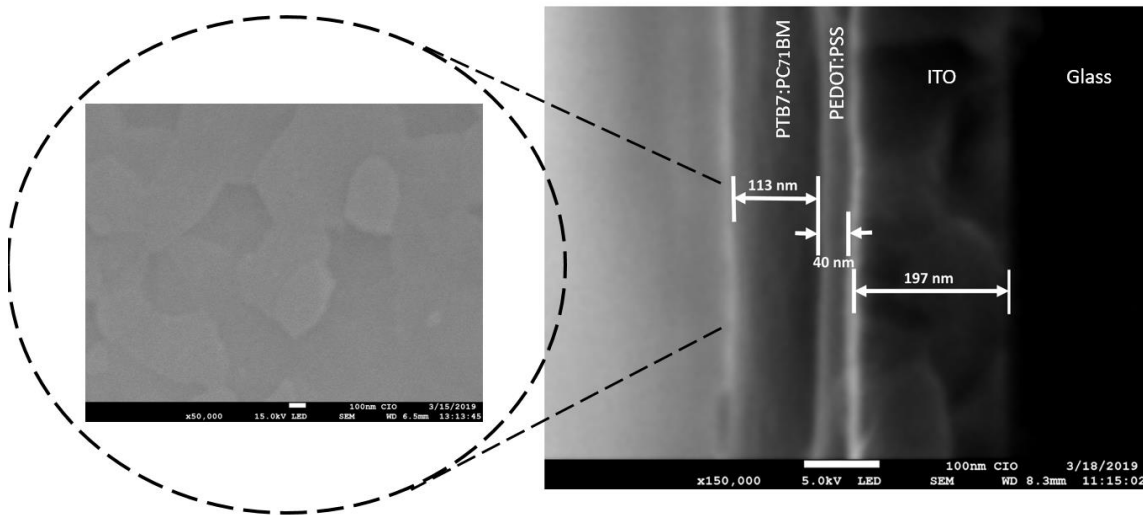
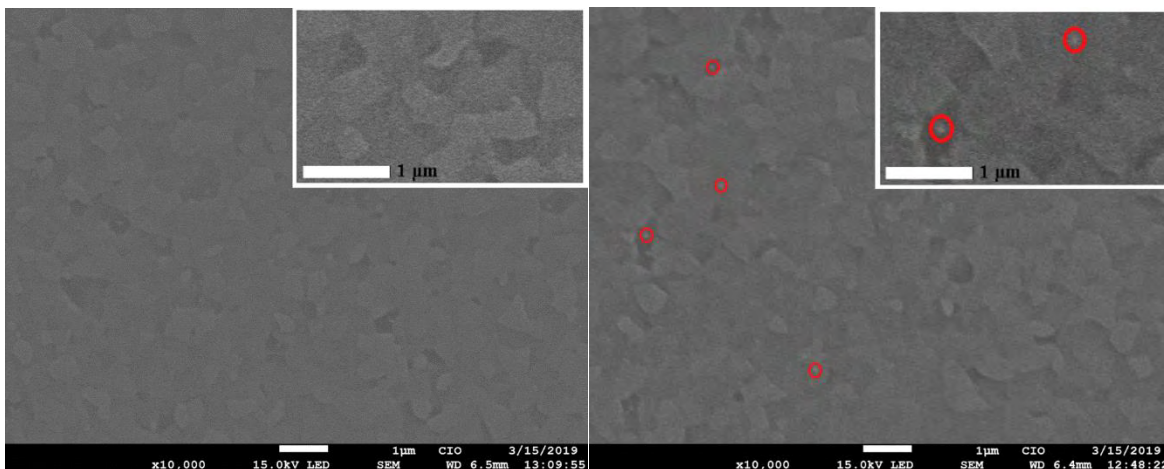


Figure 4.12: SEM image of OPVs layers (ITO ~ 197 nm; PEDOT:PSS ~ 40 nm; PTB7:PC₇₁BM ~ 113 nm) and an active layer zoom with non-NCs.

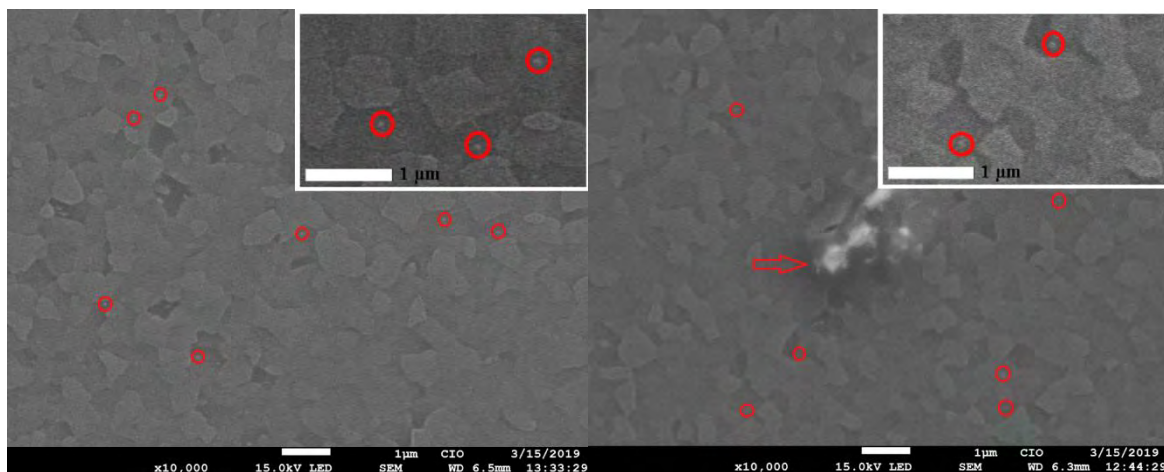
Figure 4.13, from a to d, shows SEM images of OPVs active layer with the different concentrations of FeS_2 . It can be noted the ITO layer (granular structure) due to the high used voltage for these SEM measurements (15 kV) in comparison with that for PEDOT:PSS image (Figure 4.13e) taken

at low voltage (1 kV) where the ITO layer cannot be distinguished. These SEM images are a complement to the AFM images showed in Figure 4.11; some NCs were denoted inside red circles, however, it is not very clear to observe them because they are immersed in the polymer matrix. In Figure 4.13b and c (0.25 wt. % and 0.5 wt. % respectively) can be observed some NCs distributed in the active layer, in minor quantity and more isolated for the b case (0.25 wt. %) compared to the c case (0.5 wt. %). In case d (1 wt. % of FeS₂) NCs agglomerates can also be observed.



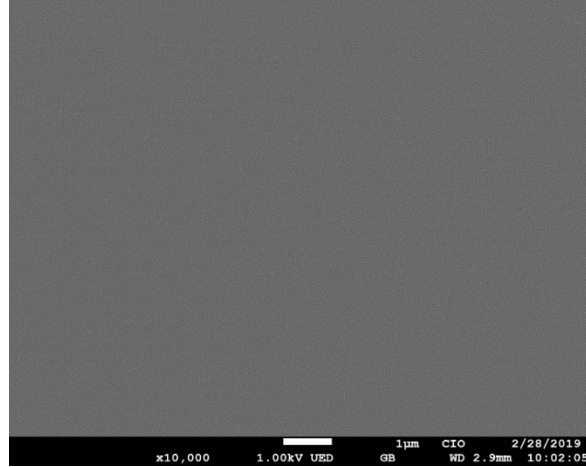
a)

b)



c)

d)



e)

Figure 4.13: SEM images (at 15 kV) of OPVs active layer with different concentrations of FeS₂: (a) 0.0 wt. %, (b) 0.25 wt. %, (c) 0.5 wt. % and (d) 1.0 wt. %; (e) image of PEDOT:PSS at a lower SEM voltage (1kV). Scale bar = 1 µm.

To study the CCs transport and recombination in devices based on PTB7:PC₇₁BM and PTB7:PC₇₁BM:FeS₂ (with 0.5 wt. % of FeS₂) impedance spectroscopy (IS) analysis was conducted. IS is an important technique for solar cell transport and recombination processes monitoring [142], these measurements can provide information about the different processes that limits the solar cell efficiencies: charge storage, carrier lifetimes, recombination and resistivity [143]. Figure 4.14 shows the IS (Nyquist plot) measurements and the simulations made (with the equivalent circuit model presented in Figure 8c), at different operating bias (0.0 V, 0.3 V, 0.6 V and close to Voc), under illuminated conditions for two OPVs cells based on a) PTB7:PC₇₁BM and b) PTB7:PC₇₁BM:FeS₂ with 0.5 wt. % of FeS₂. As can be seen, the fitted lines showed good agreement with the measured data. IS under dark conditions is also presented. IS achieved data are in agreement with the previously reported OPVs based on low band-gap polymers IS [63,143]. At low and large frequencies is possible to get information about the recombination (R_{rec}) and series resistance (R_s), respectively [63,142,143]. R_s is related to the overall resistance devices that can reduces J_{sc} value, R_{rec} to charge carriers recombination processes in the device and C is a non-ideal capacitor; the higher R_{rec} value is better for the devices [143]. Table 4.3 shows the equivalent circuit parameters (R_{rec} and R_s) reached from the fitted data for PTB7:PC₇₁BM and PTB7:PC₇₁BM:FeS₂ (with 0.5 wt. % of FeS₂) based solar cells. These values are in good agreement with the reported values of PTB7:PC₇₁BM solar cells [63,143]. R_s data are similar for both devices, which might suggest that the possible fabrication defects in the stack architecture are comparable

in both devices [63]. R_{rec} values present a rapid decrement while applied bias increased from 0.0 V to near V_{oc} , as shown in Figure 8d. This behavior is due to the fact that at high bias, the carriers density in the OPV increases and thus more recombination takes place in the device [63,143]. From Figure 4.14 and Table 4.3, it can be noted that R_{rec} values are in the same order of magnitude for both systems, but recombination resistance is higher for PTB7:PC₇₁BM:FeS₂ cells (red curve) to that of PTB7:PC₇₁BM (blue curve) cells. Therefore, IS analysis suggests that electrical losses by charge carriers recombination are diminished in devices with FeS₂ nanoparticles (specifically with 0.5 wt. %) and, therefore, the J_{sc} and FF values (shown in Table 4.2) of the latter device are improved.

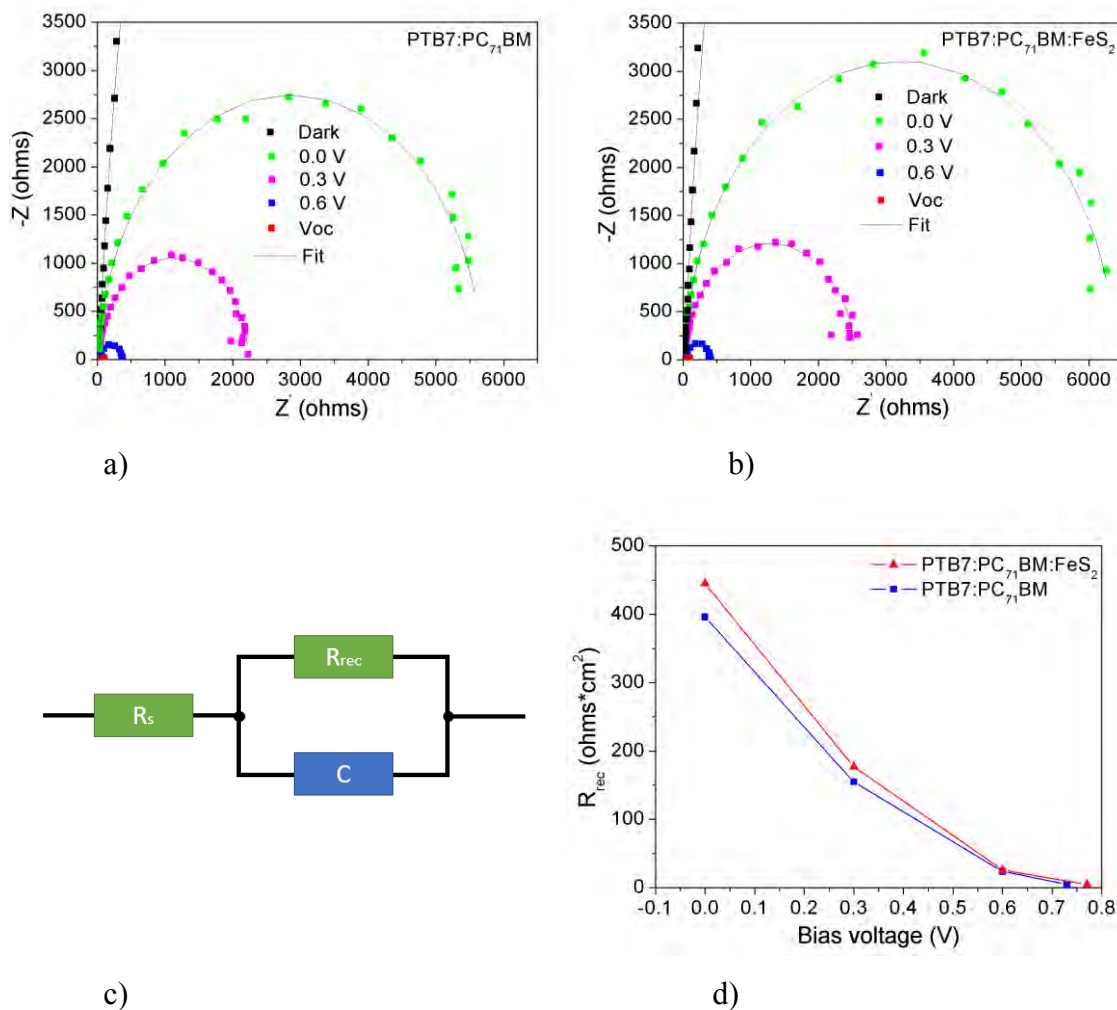


Figure 4.14: Impedance spectroscopy measurements (filled color squares) and simulations (black lines) of a) PTB7:PC₇₁BM and b) PTB7:PC₇₁BM:FeS₂ (with 0.5 wt. % of FeS₂); c) Equivalent circuit used for IS simulations; d) R_{rec} values vs bias voltage for PTB7:PC₇₁BM (blue) and PTB7:PC₇₁BM:FeS₂ (with 0.5 wt. % of FeS₂) (red).

Table 4.3: Parameters of the equivalent circuit used to simulate experimental IS data for PTB7:PC₇₁BM and PTB7:PC₇₁BM:FeS₂ (with 0.5 wt. % of FeS₂) based solar cells.

Device	DC bias (V)	R _s (Ω · cm ²)	R _{rec} (Ω · cm ²)
PTB7:PC ₇₁ BM	0.0 V	1.59	396
	0.3 V	1.83	155
	0.6 V	2.22	24
	Voc	2.20	5.2
PTB7:PC ₇₁ BM:FeS ₂ (0.5 wt. % of FeS ₂)	0.0 V	1.67	445
	0.3 V	1.88	177
	0.6 V	2.32	26
	Voc	2.27	4.8

Figure 4.15 shows two graphs for the OPVs averaged electrical parameters versus FeS₂ content of three independent experiments for each concentration. OPVs parameters present small variation for 0.5 wt. % and 1.0 wt. % of FeS₂ content compared with the reference (0.0 wt. %), however, as previously stated, PCE is statistically enhanced for the 0.5 wt. % FeS₂ concentration. For 1.0 wt. % of FeS₂ parameters starts to decrease because of the FeS₂ agglomerates. PV parameters decay significantly with 0.25 wt. % of FeS₂, as commented before. Summarizing, with the addition of 0.5 wt. % of FeS₂, a better charge generation/transport/collection is potentially reached because of the better exciton dissociation and additional charge pathways in the active layer. To the best of our knowledge, it is the first time that FeS₂ NCs are added to the PTB7:PC₇₁BM active layer and reached a PCE improvement in OPV devices.

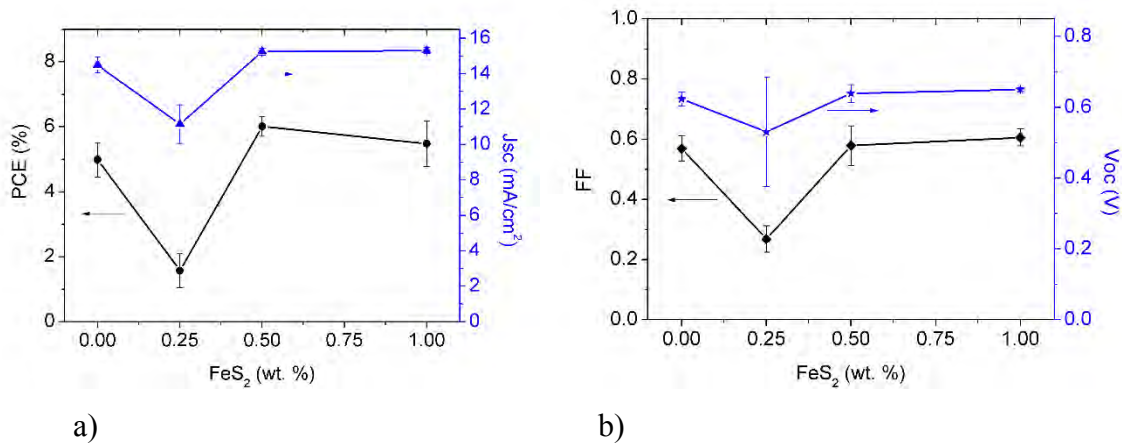


Figure 4.15: Electrical parameters of OPVs as a function of FeS₂ NCs content. Three different sets and at least three devices for each concentration were tested.

Conclusions of section 4.2

Iron sulfide (FeS_2) nanocrystals were added as a third component (second electron acceptor) in the PTB7:PC₇₁BM active layer to enhance solar cell performance. It was found, by varying the FeS_2 content (0, 0.25, 0.5 and 1.0 wt. %), an increment in PV parameters at a specific doping level (0.5 wt. %). PCE was 21% improved (average PCE of ~ 6 % (best = 6.47 %)) compared to reference devices (average PCE of ~ 5 % (best = 5.69 %)). Hence, FeS_2 NCs, due to the energy level accommodation within the active layer, potentially assist charge dissociation; also additional charge-carrier pathways are created improving charge transport and collection.

4.3. PTB7-Th: Active layer thickness variation analysis

In this section, an analysis of EQE and IQE of OPVs, based on PTB7-Th:PC₇₁BM, as a function of the active layer thickness ranging from 40 to 165 nm is carried out.

Sample preparation and characterization

All chemicals were used as they were purchased without further purification. After ITO substrates were cleaned and dried, a PEDOT:PSS layer of 40-nm thickness was spin-coated at 4500 rpm on top of the ITO substrate and dried in an oven for 20 minutes at 120 °C. As electron donors were used PTB7 and PTB7-Th (1-Material Inc.) and, as electron acceptor PC₇₁BM. The solution for the active layer was prepared by dissolving PTB7 or PTB7-Th and PC₇₁BM (ratio 1:1.5 wt %) in anhydrous CB with 3 % of DIO within a glovebox under nitrogen atmosphere. The solution was stirred in a hot plate for about 24 h at room temperature. Then, it was spin-coated, at normal room conditions, with different spin velocities onto the PEDOT:PSS layer to have the active layer thickness variation (40-165 nm). Deposited films were left in the glovebox overnight under N₂ atmosphere and at the next day, a thermal annealing of 80 °C for 15 minutes was provided. A PFN layer (~5-10 nm) was spin-coated at 5500 rpm on top of the active layer and exposed to thermal annealing for 15 minutes at 80 °C. Active area (0.07 cm²) was delimited with a Scotch tape. FM top electrode was deposited (after melting it at 95 °C in a hot plate) by drop casting on top of the PFN layer; during this procedure, the OPV cell was kept in the hot plate at the same temperature. Finally, OPVs cells were cooled down at room temperature. In Figure [4.16](#) the OPV cell structure: glass (1.1 mm)/ITO(165 nm)/PEDOT:PSS(40 nm)/PTB7-Th:PC₇₁BM(40-165 nm)/PFN(~5 nm)/FM used in this work is schematized.

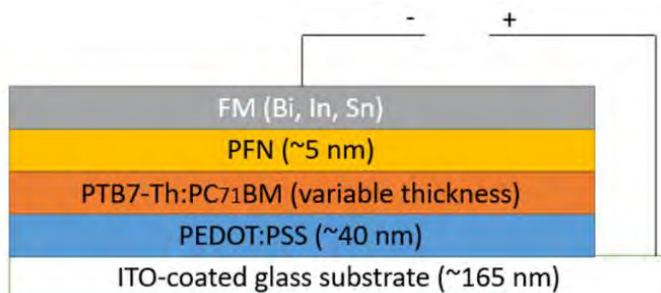


Figure 4.16: Architecture of the fabricated OPVs cells. See chemical structures in page x, before Introduction section.

OPVs J - V curves were measured by a Keithley 2450 source meter under normal room conditions with a solar simulator Sciencetech SS150 class AAA (under AM1.5). For film thickness and morphology, it was used the AFM operated in contact mode employing cantilever tips with aluminum reflective coating (ContAl-G) from BudgetSensors. When operating in tapping mode by using cantilever tips PPP-NCLAu with a metallic layer (Au), phase contrast and topography images of the layers were acquired; measurements were performed under ambient conditions. For these AFM measurements, sample films were prepared under the same OPVs fabrication procedure (without PFN neither FM); active layer thickness was ~ 100 nm. For STM measurements, PTB7 and PTB7-Th were dissolved in 1-phenyloctane with 3% of 1,8-diiodooctane (DIO) with a concentration of 0.1 mg/ml, and deposited on highly ordered pyrolytic graphite (HOPG) surface by drop casting. The use of 1-phenyloctane with DIO helps to get a better image quality because a phase separation between the polymer aggregated and nonaggregated chains occurs [61]. Electrochemically etched and mechanically cut Pt-Ir wires were used as STM tips. Before each film deposition, HOPG substrates were cleaved by using the adhesive tape technique to obtain an atomically clean surface; then, a droplet (about 2 μ l) of 1-phenyloctane was directly deposited between the tip and the sample surface to make the liquid/solid interface for STM measurements [61]. Sample thicknesses for STM measurements were less than 1 nm (about 300 pm according to an image profile that was taken and analyzed through Gwyddion open source software (v. 2.49)). For XRD and SEM characterizations, active films were prepared under the same OPVs fabrication procedure; however, for these cases, active layer thickness was ~ 180 nm.

OPVs results

In Figure 4.17 are shown the best J - V curves and achieved efficiencies for our fabricated OPVs based on PTB7:PC₇₁BM (PCE = 6.89 %) and PTB7-Th:PC₇₁BM (PCE = 7.65 %) as active layers.

PCE values for these OPVs (under direct configuration) are comparable with OPVs based on PTB7 derivatives reported in the literature: range 5–10 % [28,96]. The best PCE presented in this work (7.65 %) is slightly larger than one of the highest PCE reported under a similar configuration: 7.35 % [28]. However, for the EQE/IQE analysis carried out here as a function of the active layer thickness, we were more interested in maintaining the preparation conditions over the entire range of the studied active layer thicknesses, i.e., for these measurements, PCE values were slightly smaller; additionally, here it was used the alternative FM top electrode vacuum-free deposited [16,59,60,63].

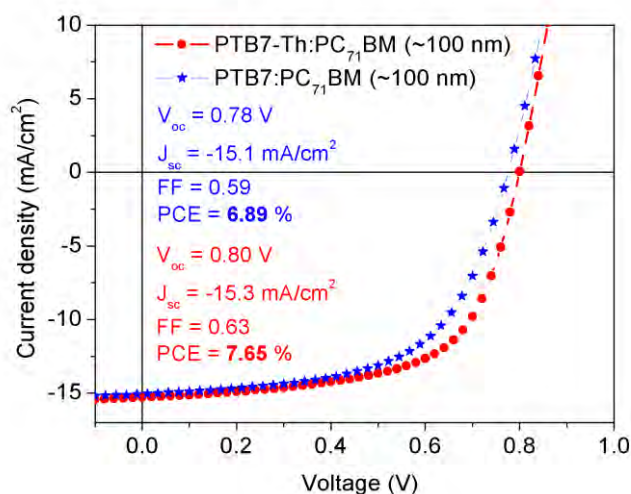


Figure 4.17: Best J - V curves and achieved efficiencies for PTB7:PC₇₁BM (blue curve) and PTB7-Th:PC₇₁BM (red curve) based OPVs devices by using the FM alternative top electrode vacuum-free deposited. OPVs performance is somewhat better for those based on PTB7-Th polymer.

In Figure 4.18 J - V data, for one of the sets made with PTB7-Th:PC₇₁BM blend (three different sets were fabricated and tested to verify these data), are presented for the active layer thickness from 40 to 92 nm (a) and from 100 to 165 nm (b); the measured EQE values versus wavelength are also shown for the corresponding thicknesses in c and d. It is noteworthy that the best EQE values are for the thickness range 92 to 110 nm, which are in concordance with the best PCE achieved efficiencies. In Table 4.4 are shown the PV parameters for the active layer thicknesses analyzed in this work. Also it is presented in Table 4.2 two EQE values (at 500 and 730 nm) to better observe the EQE differences between thicknesses. In Table 4.4 it is shown the highest achieved PCE (6.77 %) in that set and it is correlated with the highest EQE value at 485 nm (53 %), it corresponds for an active layer thickness of 100 nm, which is the optimum active layer thickness for most BHJ architecture [49–52]. In the thickness range 80 to 120 nm, J_{sc} values are in good agreement with

those reported in the literature for PTB7-Th:PC₇₁BM active layer (range: 13 to 15 mA/cm² [64,144]). Determined values for R_s and R_{sh} are between 2–20 Ωcm^2 and 138–210 Ωcm^2 , respectively, which are similar to those OPVs reported for PTB7-Th:PC₇₁BM blend film [64,144]. Also, similar R_s and R_{sh} values, to those mentioned in this work, are reported by H. Park et al. [50] for the blend PTB7:PC₇₁BM. The obtained V_{oc} and FF also are similar to those found in the literature under a similar configuration [64,144].

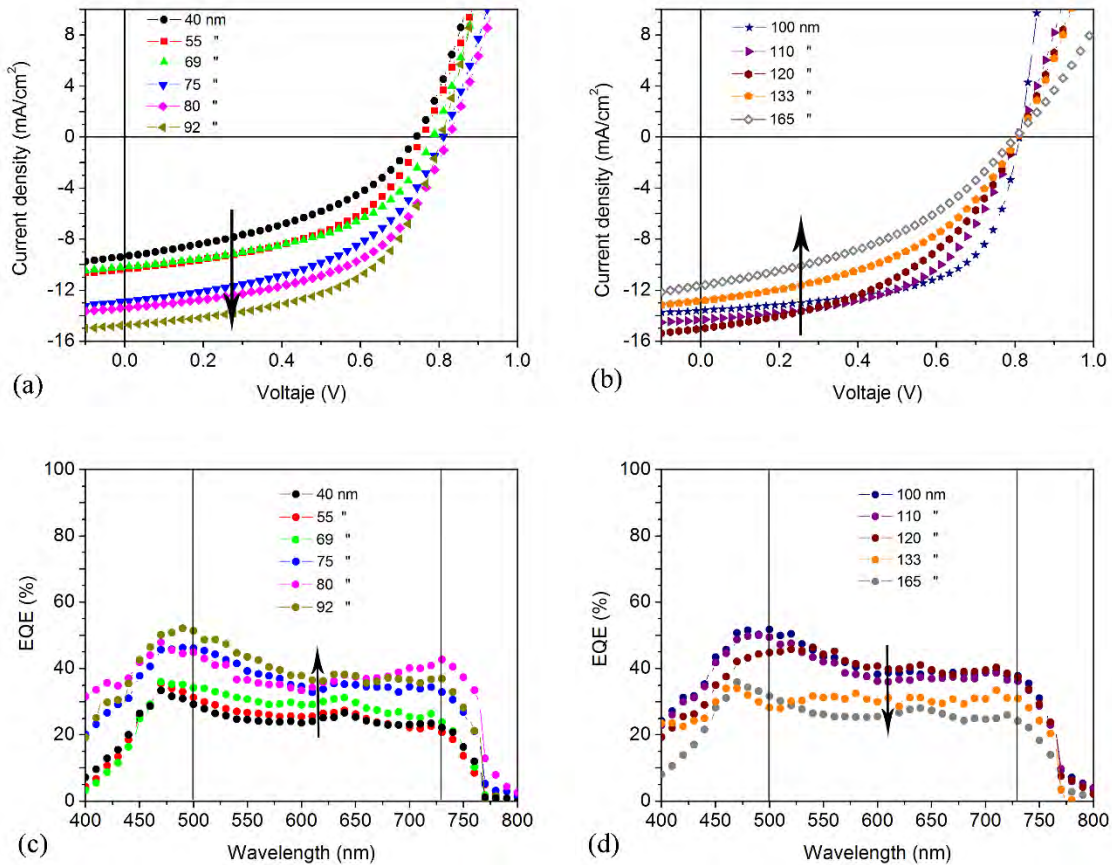


Figure 4.18: Current-density vs voltage (J - V) curves of PTB7-Th based OPVs devices with active layer thicknesses from (a) 40 to 92 nm, and (b) 100 to 165 nm. EQE vs wavelength of devices with active layer thicknesses from (c) 40 to 92 nm, and (d) 100 to 165 nm. For each thickness, at least three OPVs samples were fabricated and tested, they followed a similar trend.

Table 4.4: PV parameters at different active layer thicknesses. For each thickness, at least three OPVs samples were fabricated and tested, they followed a similar trend. OPVs configuration: glass/ITO/PEDOT:PSS/PTB7-Th:PC₇₁BM/PFN/FM. Standard deviation is included for the PCE values.

Thickness (nm)	V_{oc} (V)	J_{sc} (mA/cm ²)	FF	PCE (%)	EQE (500nm) (%)	EQE (730nm) (%)	R_s (Ω cm ²)	R_{sh} (Ω cm ²)
40	0.74	9.4	0.42	2.91±0.30	32	24	6	138
55	0.76	10.4	0.48	3.79±0.41	31	21	7	170
69	0.79	10.2	0.49	3.94±0.28	34	24	5	177
75	0.81	12.9	0.48	5.05±0.25	46	33	7	167
80	0.82	13.4	0.52	5.75±0.35	45	43	7	197
92	0.81	14.8	0.55	6.55±0.38	51	37	5	208
100	0.81	13.6	0.61	6.77±0.88	52	38	2	193
110	0.80	14.3	0.54	6.21±0.40	49	36	8	210
120	0.81	15.0	0.45	5.53±0.31	45	37	10	156
133	0.80	12.8	0.46	4.71±0.32	28	31	8	140
165	0.80	11.6	0.41	3.80±0.45	29	22	20	191

In Figure 4.19a and b are presented the PCE, J_{sc} , V_{oc} and FF values as a function of the active layer thickness. As shown in Figure 4.19a, PCE values increase when increasing the active layer thickness until 100 nm and, after that maximum, PCE values once again decrease. It is due to the CCs recombinations and charge's trapping that are present when the active layer is thicker (above 110 nm producing losses and reducing the possibility of CCs to survive and arrive to the electrodes [50]). On the other hand, when the active layer thickness has a significant decrease (under 75 nm) PCE is also reduced because not enough CCs are generated. J_{sc} values have a similar behavior than the PCE ones, while in Figure 4.19b V_{oc} values remains almost constant for all thicknesses and FF also decreases with increasing thickness (above 100 nm), however, it maintains similar values for thicknesses over 120 nm.

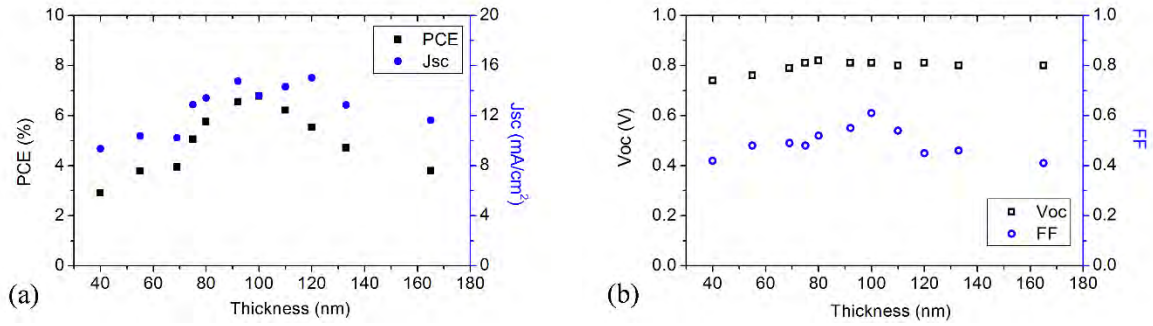


Figure 4.19: (a) PCE (filled squares), J_{sc} (filled circles), (b) V_{oc} (open squares), and FF (open circles) as a function of the active layer thickness.

In Figure 4.20a EQE values versus active layer thickness at the wavelengths of 500, 580 and 730 nm (see Figure 4.18c-d) are showed; these particular wavelengths were chosen because close to 500 nm is where the largest EQE values are reached, 730 nm is where there exists the maximum absorption of PTB7-Th and, 580 nm just as an intermediate wavelength. The average maximum EQE values for the three wavelengths are in the thickness range 92-110 nm, corresponding to the same range where the maximum values of PCE are reached (see Figure 4.19a).

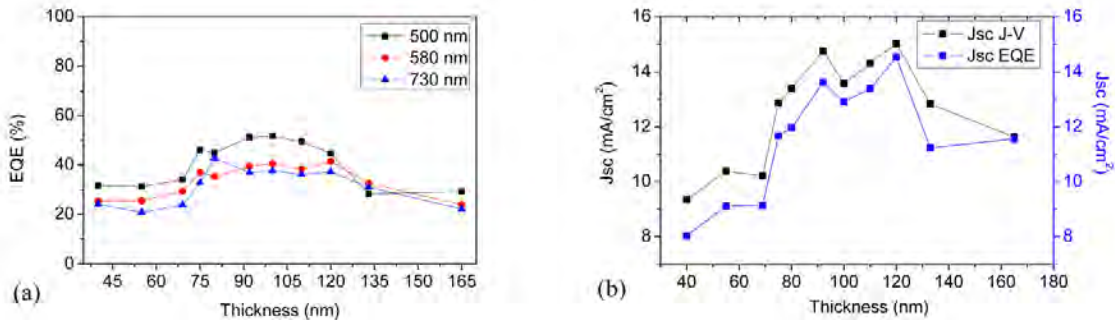


Figure 4.20: (a) EQE values at 500, 580 and 730 nm as a function of the active layer thickness, (b) J_{sc} determined from J - V curves (black squares) and J_{sc} estimated from EQE measurements (blue squares) versus active layer thickness.

In Figure 4.20b are shown the J_{sc} values determined from J - V curves (black squares) and those estimated from EQE measurements (blue squares) versus active layer thickness; as it can be seen, they follow the same behavior. In Table 4.5 are listed the J_{sc} values from J - V curves and from EQE measurements. As we can see, values are similar; however, always the estimated J_{sc} value from EQE is smaller than that from J - V curve (see also Figure 4.20b). It could be due to the fact that when EQE measurements were carried out, an approximately 10 % smaller OPV area was excited (illuminated) than the size of the solar cell's active area (0.07 cm^2), it was due to our experimental EQE set up conditions.

Table 4.5: Current density values from J-V curve vs the estimated ones from EQE. OPVs configuration: glass/ITO/PEDOT:PSS/PTB7-Th:PC₇₁BM/PFN/FM

Thickness (nm)	J_{sc} J-V (mA/cm ²)	J_{sc} EQE (mA/cm ²)
40	9.4	8.0
55	10.4	9.1
69	10.2	9.2
75	12.9	11.7
80	13.4	12.0
92	14.8	13.6
100	13.6	12.9
110	14.3	13.4
120	15.0	14.5
133	12.8	11.2
165	11.6	11.5

On the other hand, the optical electric field (of the illumination light) is affected by interference effects due to the strong light reflection at the metal as top electrode, and partial reflections at the layers interfaces of the cell stack when light propagates through the device. Thus, the optical electric field is modulated and when the active layer thickness increases the electrical field peaks could move off the active film. To better understand these facts, it was used the TMM for simulating the optical electric field inside the device. For simulations, our OPVs devices are considered as a stack of m layers and $m+1$ interfaces, which are parallel between them (see Figure 4.16); the thicknesses of all layers were kept fixed during calculations, except the active layer thickness that goes from 40 to 165 nm as mentioned above. It will be also assumed that the incident electromagnetic plane waves arrive to the first layer at normal incidence (from the ITO side) and that the top electrode is a mirror, represented by FM, with high reflectivity (then, the incident light travels twice through the active layer). These simulations only provide insight of the optical effects, but details of the excitons dissociation and CC's transport and collection efficiencies are needed to gain a complete picture of CC's generation and extraction. Both, optical and electronic effects define the overall performance of OPV devices.

In Figure 4.21 is presented the absorbance spectra of ITO, PEDOT:PSS and PTB7-Th:PC₇₁BM thin films: (a) experimentally determined (for each single layer; taking into account the same experimental conditions than for the whole OPV device), (b) calculated through TMM (without taking into account reflection and interference effects, i. e., for each single layer), and (c) estimated through TMM when taking into account reflection and interference effects (whole cell stack including PFN and FM). As expected, case c corresponds to the active layer film that mainly absorbs the incident energy for the considered PV device. Plots determined experimentally in a and through TMM in b did not take into account the reflection and interference processes that occurs into the cell due to FM top electrode (working as a perfect mirror), the absorbance for those layers were independently obtained and for this reason, results are significantly different to those reached through simulations with all the cell structure in c. Indeed, the measured active layer absorbance in a is smaller than the simulated (with all the layers together) in c because there is not the double light absorption (when reflected light at the top electrode is no presented) neither other interface reflections.

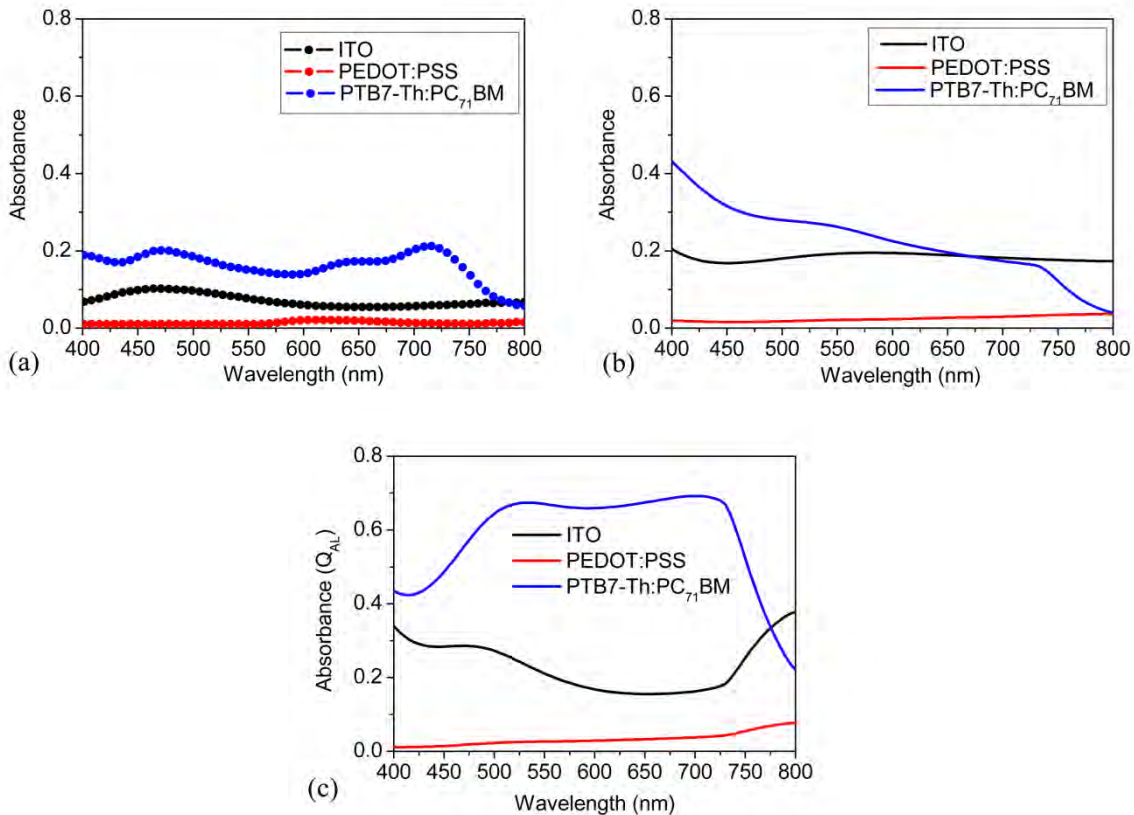


Figure 4.21: Absorbance of ITO, PEDOT:PSS and PTB7-Th:PC₇₁BM layers (a) experimentally determined (for each single layer), (b) calculated through TMM (for each single layer), and (c)

determined through TMM (with all the cell structure, where light cross the films twice because of the reflection at the top electrode and also there are other reflections contributions because of the films interfaces). Film thicknesses: 165, 40 and 100 nm for ITO, PEDOT:PSS and PTB7-Th:PC₇₁BM layers, respectively.

The square modulus of the optical electric field was calculated when light propagates through the layers of the OPV as shown in Figure 4.22 for an active layer thickness of 100 nm. It is considered a unitary incoming intensity and that light arrives from the bottom (ITO). At the beginning the intensity is unitary but when reflection occurs the intensity is amplified. It was observed an oscillatory behaviour (see Figure 4.23) due to multiple reflections at the interfaces as the light travels inside the device. The oscillatory behavior denotes the incipient formation of standing waves inside the system. PFN layer shows almost zero intensity of the electric field, this layer is very thin (~ 5 nm) and it is close to the reflective top electrode where the electric field must be quickly annulled. Also, it is shown the electric field for incident light (arriving from the left side) in Figure 4.23a with 500 (blue line) and 730 (red line) nm of wavelength, for an active layer thickness of 100 nm and in Figure 4.23b with 500 nm of wavelength for all active layer thicknesses. It should be noted that the extinction coefficient for the active layer is several times larger than the corresponding for ITO and PEDOT:PSS (for ITO = 0.054 [86], PEDOT:PSS = 0.08 [87], and for PTB7-Th:PC₇₁BM = 0.325 at 600 nm, see Figure 3.8). It is worth to mention that for an active layer thickness of 100 nm, the maximum electric field is roughly at the active layer center, which could improve the CCs transport and collection (for other thicknesses the maximum is sometimes shifted, see Figure 4.23b).

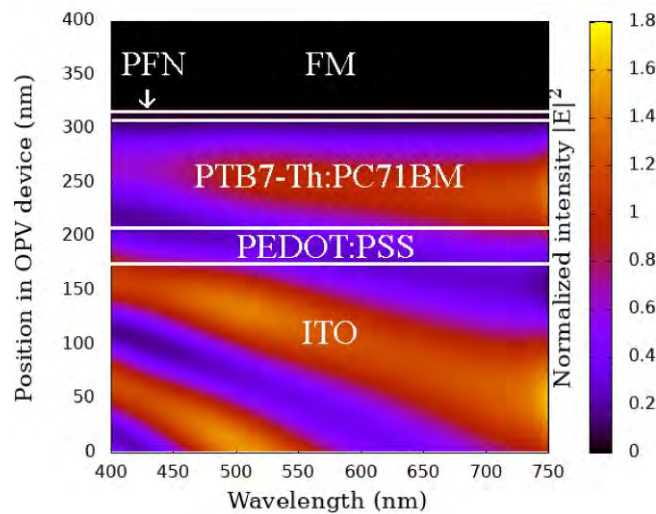


Figure 4.22: Optical electric field intensity (black color = zero intensity, yellow = maximum value estimated by TMM considering a unitary incoming intensity (light arriving from the bottom side)) passing

through these layer thicknesses: 165 nm of ITO, 40 nm of PEDOT:PSS, 100 nm of PTB7-Th:PC₇₁BM and 5 nm of PFN.

Similar simulations to those shown in Figure 4.22 and 4.23 were carried out in previous works for PTB7-Th:PC₇₁BM [52], PTB7:PC₇₁BM [50] and other active film blends [87]. Based on Figure 4.22, the generated charges could be correlated to the optical electric field intensity inside the active layer [50]. Kobori and Fukuda [52] stated that current density (J_{sc}) is not increasing proportional to the increase of active layer thickness, that the J_{sc} behavior is in agreement with the change in the simulated optical intensity distribution, and that there exist a close correspondence between the OPV performance and the optical density distribution. As mention before, the layer thicknesses plays a very important role in the optical electric field behavior. For example, if the ITO layer thickness were 20 nm, the optical electric field inside the stack would be different; besides, the ITO thickness is important for OPV performance because, with lesser ITO thickness the sheet resistance becomes bigger and thus the conductivity decrease.

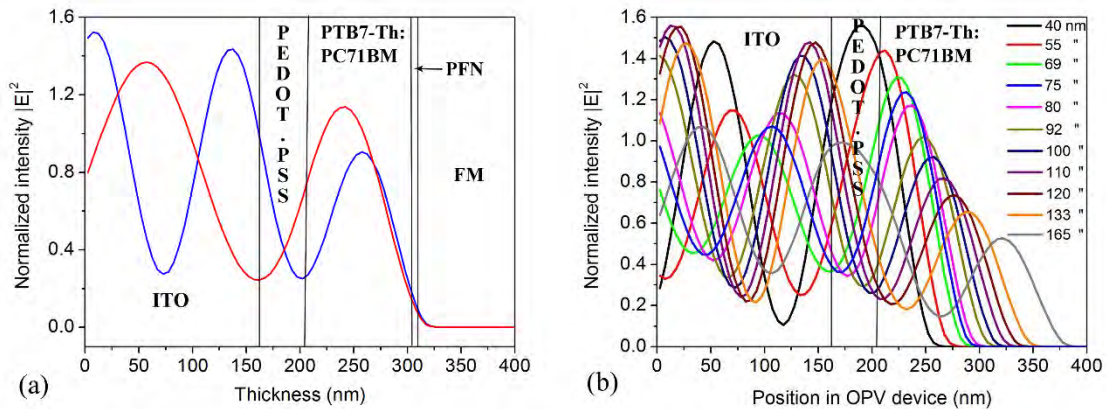


Figure 4.23: Optical electric field intensity calculated by TMM considering a unitary incoming intensity (incident from the left) for (a) 500 nm (blue line) and 730 nm (red line) light wave for an active layer thickness of 100 nm, (b) 500 nm light wave for all active layer thicknesses (from 40 to 165 nm, OPV position means from 205 nm to 370 nm for the thicker active layer). The showed electric field is the result from reflection and interference processes that occur inside the OPV cell stack.

Each layer absorption cannot be independently measured because the optical density of all layers together is not the sum of the optical density in each layer. This is due to interference effects caused by reflections and transmissions in the stack. The top metal electrode, used as cathode, introduce strong interference effects that contribute in the OPV absorption [94]. Figure 4.24a shows the calculated absorbance by TMM for the studied range of thicknesses of the active layer over glass substrate (single layer). On the other hand, Figure 4.24b shows the absorbance (Q_{AL}) by TMM when taking into account all the presented layers in the OPV device (see Figure 4.21b and c for

the active layer thickness of 100 nm). It can be seen that, without the other layers, absorbance increases as thickness does, however, for the case with the other presented OPVs films, this regularity is lost due to the mentioned interference effects. In this latter case, there exist an increment of the absorbance until about 80 nm, after that, it decreases again because the absorption in these thin film multilayer structures typically exhibits strong interference due to multiple reflections and transmissions at the interfaces. It is necessary to remember that for the estimation of IQE is more precise the case when all OPVs layers are presented. It is noted that the better efficiency obtained was for an active layer thickness of 100 nm and this result did not match with the thickness with better theoretical absorbance (80 nm). It could be due to the fact that the electric field inside the active film with 100 nm has a centered maximum and in the 80 nm case the maximum is shifted (see Figure 4.23b). When the maximum is centered, the electric charges could have better chance to arrive to the corresponding electrodes if the electron and hole mobilities values are matched. One way to obtain a ratio close to 1 between the electron and hole mobilities ($\mu_e/\mu_h = 1$) is varying the mixed weight ratio between the donor and acceptor materials [145]. The electron mobility for PC₇₁BM is $1 \times 10^{-3} \text{ cm}^2 \text{ V}^{-1} \text{ s}^{-1}$ [146] and the hole mobilities for PTB7 and PTB7-Th is $5.8 \times 10^{-4} \text{ cm}^2 \text{ V}^{-1} \text{ s}^{-1}$ [117] and $2.83 \times 10^{-3} \text{ cm}^2 \text{ V}^{-1} \text{ s}^{-1}$ [28], respectively, as showed in Table 4.1. Then, mobilities are in the same order of magnitude and with the D:A weight used ratio (1:1.5) the electrons and holes could arrive to their respective electrodes quasi-simultaneously. However, it is necessary to take into account also the buffer layers thickness and their mobilities. PEDOT:PSS and PFN film thicknesses are approximately 40 and 5 nm, respectively. When holes and electrons move through the PEDOT:PSS and PFN layers, respectively, mobility values change (PEDOT:PSS has a hole mobility of $1 \times 10^{-4} \text{ cm}^2 \text{ V}^{-1} \text{ s}^{-1}$ [147] and for the PFN layer it is assumed that carrier transport is similar as in the active layer because of the tiny PFN thickness (~ 5 nm) [148]).

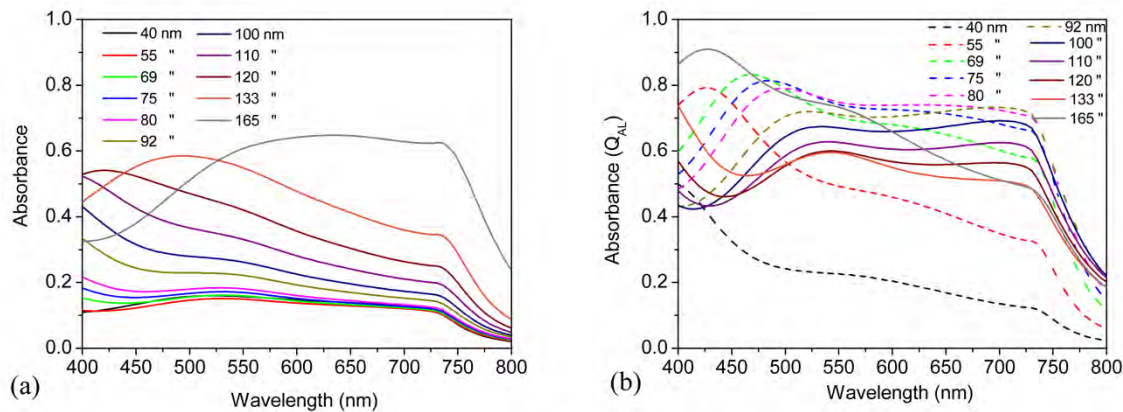


Figure 4.24: PTB7-Th:PC₇₁BM absorbance for each active layer thickness determined by TMM: (a) when just the active film is deposited on glass substrate; (b) with the complete cell configuration.

In Figure 4.25, the active layer absorbance (Q_{AL}) versus thickness, by taking into account reflection and interference effects as in Figure 4.25b, is presented for three different wavelengths: 500, 580 and 730 nm. Graphs follow the same trend: until 80 nm there exists an increment and then, a decrement in the absorbance occurs.

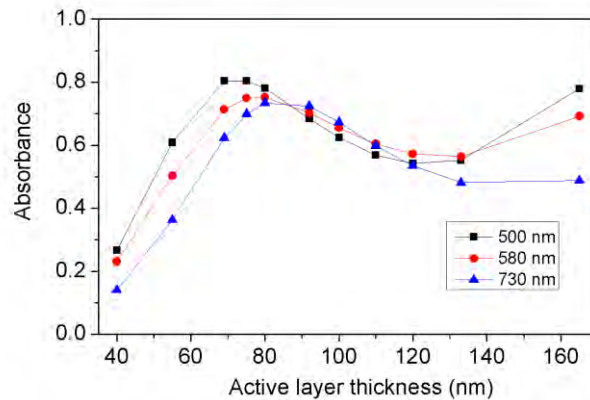


Figure 4.25: Active layer absorbance (by taking into account all the OPV layers) vs thickness obtained with TMM for three different wavelengths: 500, 580 and 730 nm.

With the active layer absorbance spectra showed in Figure 4.24b and the EQE measurements from Figure 4.18c and d, it was possible to calculate the IQE spectra for all the active layer thicknesses (according to equation (8)) as shown in Figure 4.26a from 40 to 92 nm and b from 100 to 165 nm. Figure 4.26c shows IQE versus active layer thicknesses for 500, 580 and 730 nm of incident wavelength. Analyzing the absorbance trend in Figure 4.25, it is noted that the better absorbance range is for 69-92 nm thickness. However in Figure 4.20a and Figure 4.26c, the range from 92 nm to 120 nm is where the best EQE and IQE values are reached. As we can see, before 92 nm and

after 120 nm, EQE and IQE values are smaller than those for the 92-120 nm range. It means that in the range of 92 to 120 nm the largest number of absorbed photons in the active layer are converted to charges and collected by the electrodes. Such deviations between PCE with the internal absorption, as the active layer thickness increases, have been reported previously [51,81,82] and it is correlated with the internal reflections and their interferences.

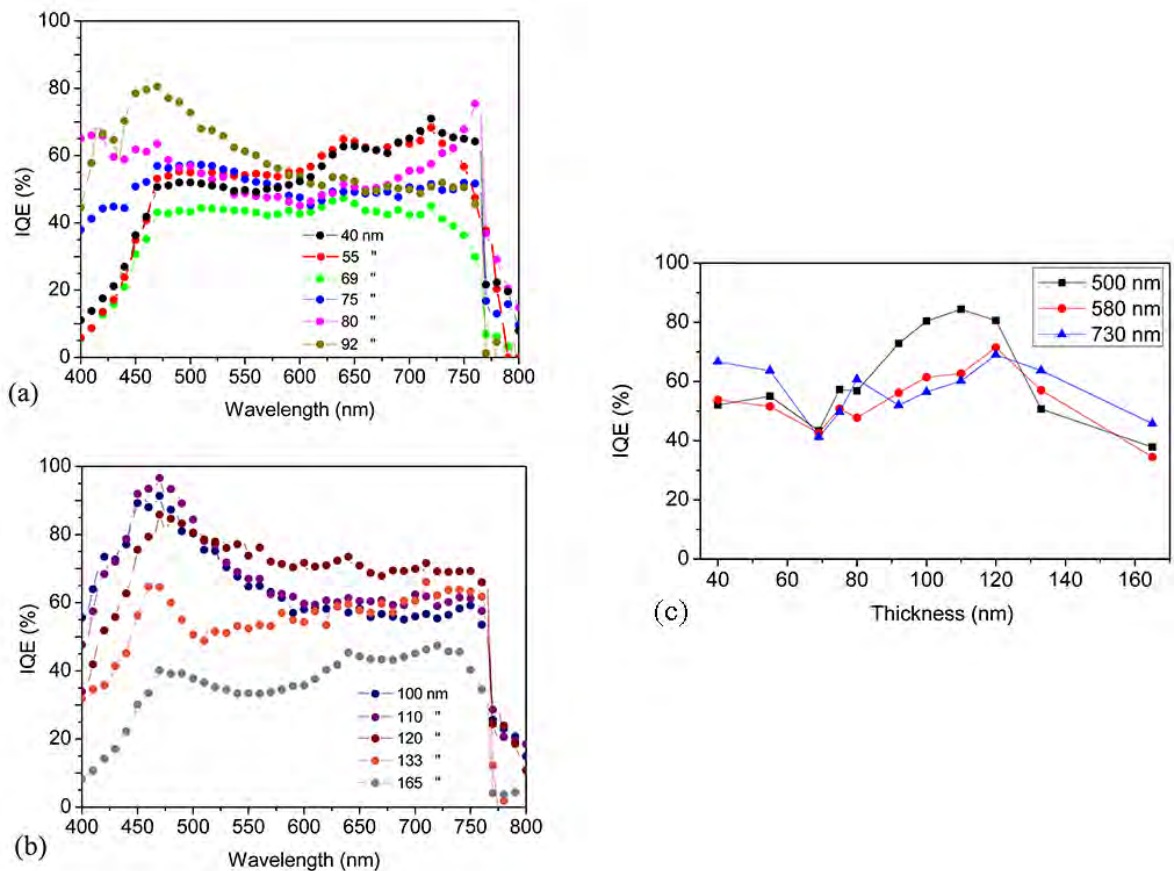


Figure 4.26: Internal Quantum Efficiency (IQE) obtained from EQE and the PTB7-Th:PC₇₁BM absorbance (from TMM) (a) from 40 to 92 nm thickness; (b) from 100 to 165 nm thickness; (c) IQE versus active layer thickness for three different wavelengths: 500, 580 and 730 nm.

In Table 4.6 are presented the IQE values for all the active layer thicknesses range at four specific wavelengths (470 (around maximum), 500, 580 and 730 nm). Here, values close to 100% were reached at any specific active layer thicknesses, however, at thicknesses larger than 120 nm, IQE values rapidly start to decrease similar to the earlier reports (see Figure 4.26b) [50,77]. The maximum IQE in Figure 4.26b reaches 97% at 470 nm for an active layer thickness of 110 nm (having an EQE of 49 %); and for an active layer thickness of 100 nm (maximum reached PCE), IQE value reaches 91.3% and EQE 50.7%, showing that these IQ efficiencies, related with the

exciton dissociation, the charge transport in donor and acceptor networks, and the charge extraction in both organic/electrode interfaces, are close to 100% in those thicknesses at specific wavelengths. After reached the maximum value, in some cases, IQE starts to decrease; for the 100 nm case, IQE goes down around 60% approximately. When having IQE close to 100 %, morphology of the OPVs active blended films should be close to the ideal donor and acceptor nanometer-scale interpenetrating network [47]. R_s and R_{sh} values are directly related with the OPVs morphology and consequently with their PV performance. The relatively small variation in R_s and R_{sh} values (see Table 4.4), indicates that morphology is not ideal, however, film surface is very smooth (as shown from AFM and SEM analysis).

Table 4.6: IQE values at 470 (around maximum IQE, for an active layer thickness in the range 92-120 nm), 500, 580 and 730 nm. OPVs configuration: glass/ITO/PEDOT:PSS/PTB7-Th:PC₇₁BM/PFN/FM

Thickness (nm)	IQE (470 nm) (%)	IQE (500 nm) (%)	IQE (580 nm) (%)	IQE (730 nm) (%)
40	51	52	54	67
55	53	55	52	64
69	43	43	43	41
75	57	57	51	50
80	64	57	48	61
92	81	79	56	52
100	91	80	61	56
110	97	84	63	60
120	86	81	71	69
133	65	51	57	64
165	40	38	35	46

IQE spectra can be divided into two parts: the region from 400 to 550 nm, dominated by the contribution of fullerene, and the region from 550 to 800 nm, dominated by the polymer contribution (in terms of their absorbance). In the 400 to 550 nm range (where the fullerene mainly absorbs), high IQE values are reached (from 92 to 120 nm active layer thickness range), and it involves a comparably efficient excitons generation and collection in the PCBM domains [149]. It is thought that those increments in the lower wavelengths are because, with the annealing

treatment, occurs the phase separation in the active layer that produces a morphology with smaller fullerene domains compared to the polymer domains. Then, excitons generated in the fullerene domains could be more easily diffused to the donor and acceptor interface, producing the charge dissociation. It is worth to mention that with the active layer increases, the IQE spectral dependency changes. According to equation (6), EQE is smaller for active film thicknesses from 120 nm to 165 nm (and also PCE) because of the decrement in the IQE values. There is an increase in losses for thicker films, and it is notable due to the rapidly drop of IQE. The highest losses are for thinner active layers, where the fullerene absorption is more significant (400-550 nm). Otherwise, for thicker active layer (above 120 nm) there exist, over the entire spectrum, an IQE with a more homogeneous behavior (the IQE spectral dependence is more constant). It can be concluded that thinner devices are limited, in the 400-550 nm wavelength region, by charge generation; otherwise thicker devices are affected by an increment in recombination mechanisms [149]. If an OPV device has large absorption but low EQE, it could mean that CCs transport and collection are diminished.

From equation (6), IQE is the combination of these three factors: $\eta_{CG} \times \eta_{CT} \times \eta_{CC}$. If we analyze those factors separately, η_{CG} seems to remain high in a BHJ active layer because in D:A interfaces the excitons dissociate effectively and form stable CCs [150]. Then η_{CT} and η_{CC} will be the responsible for IQE reduction, because the CCs did not transport correctly and did not arrive to electrodes, assuming the fact that there are losses for recombination and trapping when the active layer is thicker. At thicker film thickness, charge collection becomes limited, reducing the IQE value substantially. Our findings are similar to those of previous reported works [50–52,55,76–78,82], thus, it can be mentioned that the reduction, as the active layer increases over 120 nm, in EQE, and consequently in PCE, is due to the reduction in the product of η_{CT} and η_{CC} [50].

Conclusions of section 4.3

Here were fabricated and characterized OPVs with the configuration glass/ITO/PEDOT:PSS/PTB7-Th:PC₇₁BM/PFN/FM, for different active layer thicknesses in order to obtain a fully characterization regarding EQE and IQE measurements. For these latter determinations, internal absorption was estimated through TMM by considering reflection and interference phenomena in the OPV stack. The highest IQE took place for the active layer thickness range 92 to 120 nm. This estimated IQE spectra showed a significant reduction with the increasing

of active layer thickness (> 120 nm), and also if it was very thin (< 75 nm), it is because of the losses for recombination and trapping, and poor absorption, respectively. If an OPV cell exhibits a low EQE but a high absorption, then the reduction in efficiency arises from either poor transport or poor interfacial kinetics (or both).

4.4. PBDB-T: F-rGO as an alternative hole transport layer

First, PBDB-T:ITIC and PBDB-T:PC₇₁BM binary solar cells were fabricated, reaching 8.87% and 6.87% respectively. UV-Vis absorption spectra on films of PBDB-T:PC₇₁BM (blue) and PBDB-T:ITIC (red) blends are shown in Figure 4.27a. Spectra of the blends are the mix of the independent materials spectra and can be compared with the spectra reported previously [103]. As can be noted, PBDB-T:ITIC blend has more absorption in the near infrared compared with the PBDB-T:PC₇₁BM blend, and this is because the non-fullerene acceptor molecule ITIC absorbs mainly in that region. Figure 4.27b shows $J-V$ best curves for PBDB-T:PC₇₁BM (blue) and PBDB-T:ITIC (red) blends. The best efficiencies achieved for PBDB-T:PC₇₁BM and PBDB-T:ITIC case was 6.87 % and 8.87 % respectively which are comparable with the best reported efficiencies for direct BHJ configuration but with Al evaporated cathode (8.21 % and 9.38 % respectively) [103].

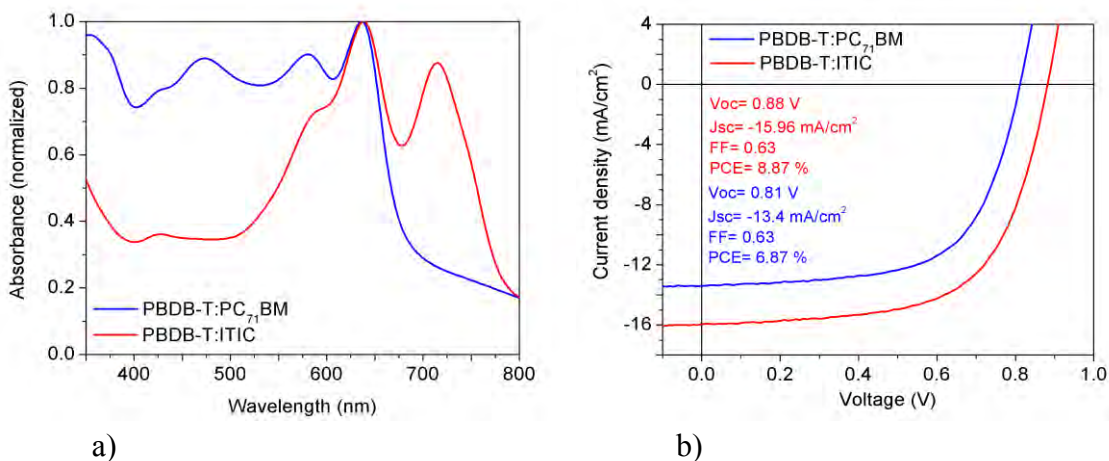


Figure 4.27: (a) UV-Vis absorption spectrum of PBDB-T:PC₇₁BM (blue) and PBDB-T:ITIC (red) and (b) $J-V$ curves of ITO/PEDOT:PSS/PBDB-T:PC₇₁BM (blue) or PBDB-T:ITIC (red)/PFN/FM.

Then, because of the results showed above, PBDB-T:ITIC blend was chosen for the HTLs tests. F-rGO is implemented in OPVs as HTL and as a bilayer with the combination of PEDOT:PSS. The well matched work function (5.1 eV) of F-rGO and PEDOT:PSS is likely to facilitate the charge transportation and an overall reduction in the series resistance [151].

Sample preparation and characterization

Flake graphite (Alfa Aesar, natural, 325 mesh, 99.8%), Sulphur acid (H₂SO₄, 98%), phosphoric acid (H₃PO₄, 85.5%), hydrochloric acid (HCl, 37%), potassium permanganate (KMnO₄, 99%), hydrogen peroxide (30%), pentafluorophenylhydrazine (Aldrich, 97%), chlorobenzene (C₆H₅Cl, Aldrich, anhydrous, 99.8%), and N,N-dimethylformamide (DMF, Aldrich, anhydrous, 99.8%) were used as received. PBDB-T and ITIC were obtained from 1-Material Inc. 1-phenyloctane and *n*-hexadecane were purchased from Sigma-Aldrich and used without further purification.

Preparation of F-rGO

Synthesis of F-rGO: GO was prepared from graphite powder according to Marcano's method as reported elsewhere [102,152,153]; is the reduction of GO with pentafluorophenylhydrazine. GO (40 mg, 1 wt equiv) was dispersed in deionized water (10 ml) using an ultrasonic bath cleaner. Then, 260 mg (1.3 mmol) of pentafluorophenylhydrazine was added to the suspension and stirred at 60 °C for 6 h. The mixture reaction was filtered, and the filtered product was washed with methyl alcohol. The black solid was dried at 80 °C for 12 h. The graphene oxide reduction with hydrazine induce chemical transformations in some functional groups; in reference [155] is reported a table with the affected ones, for example: 1-tetralone, 2-acetonaphthone, 2-hydroxy-1-naphthaldehyde, etc. Under this preparation method, OH groups in the structure, are easily lost [154]. F-rGO reaction occurs as is shown in Figure 2 of previous work of our group [154].

Devices fabrication

Figure 4.28a shows the chemical structures of ITIC and F-rGO materials, the other materials chemical structures were showed before. All chemicals were used as they were purchased without further purification. For the HTL it were tested three different approaches: PEDOT:PSS, F-rGO/PEDOT:PSS and F-rGO. PEDOT:PSS layer of ~ 40 nm thickness was spin-coated at 4500 rpm for 1 min on top of the ITO substrate (or over the F-rGO layer, after ITO substrates were cleaned and dried) and dried in an oven for 30 minutes at 80 °C. F-rGO layer (~ from 1 to 4 nm layer thickness) was spin-coated in dynamic mode at 2000 rpm for 1 min and 4500 rpm for 15 sec on top of the ITO substrate from a suspension of F-rGO in dimethylformamide (1 mg/ml) and dried in an oven for 20 min at 150°C. For the active layer it was used as electron donor: PBDB-T and, as electron acceptor, a non-fullerene material: ITIC. The solution for the active layer was

prepared by dissolving PBDB-T and ITIC at 1:1 w/w, 20 mg/ml in anhydrous chlorobenzene with 1,8-diiodooctane (CB:DIO) (99.5:0.5 v/v) within a glovebox under nitrogen atmosphere. Solution was stirred in a hot plate for about 24 h at room temperature. Then, it was spin-coated, at 2500 rpm for 1 min (active layer thickness ~ 100 nm) inside the glovebox, onto the PEDOT:PSS or F-rGO layer. A thermal annealing of 160 °C for 10 minutes was provided, and then, active layer was soaked with ethanol for 2 min and then was spin-coated on the active layer at 5000 rpm for 1 min. A PFN layer (~ 5 -10 nm) was spin-coated at 6000 rpm on top of the active layer and exposed to thermal annealing for 15 minutes at 80 °C. Active area of devices (0.07 cm²) was delimited with a Scotch tape. FM top electrode was deposited by drop casting on top of the PFN layer, after melting it at 95 °C in a hot plate; during this procedure, the OPV cell was kept in the hot plate at the same temperature. In Figure 4.28b the final OPV cell structure: glass/ITO/HTL/PBDB-T:ITIC/PFN/FM used in this work is schematized, where HTL is: PEDOT:PSS, F-rGO/PEDOT:PSS or F-rGO as mention before.

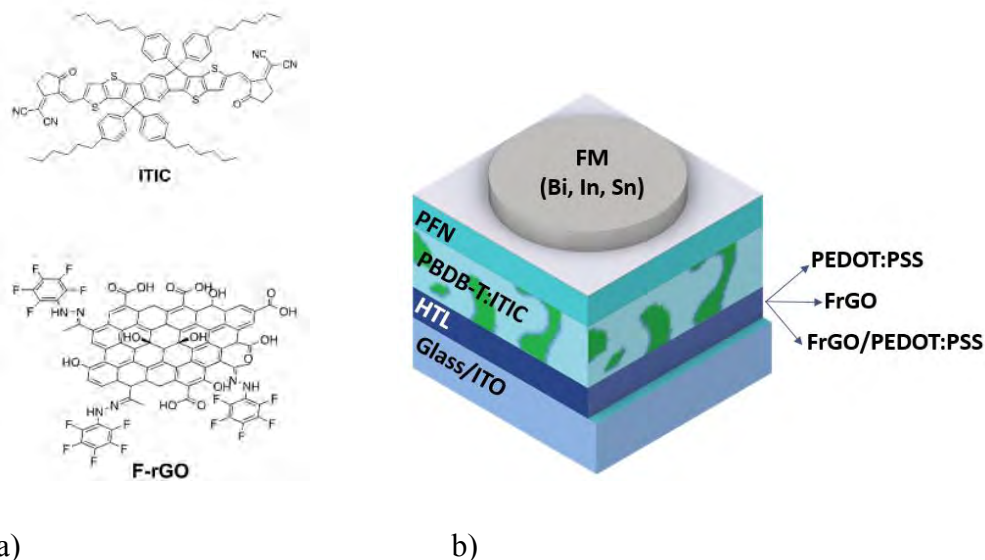


Figure 4.28: (a) chemical structures of ITIC and F-rGO, (b) architecture of OPV devices.

Characterization

For J - V , UV-Vis, SEM and EQE measurements were used the same devices mention before. In order to analyze device's stability, it was used the ISOS-D1 (shelf storage) testing protocol [156]. OPVs were stored in darkness at normal atmosphere conditions and J - V characterization was spaced for ~ 170 h (~ 7 days).

OPVs results

UV-Vis absorption spectra of the different HTLs (PEDOT:PSS, F-rGO/PEDOT:PSS and F-rGO) over glass/ITO are shown in Figure 4.29a, as noted the absorption of the three buffer layer tested are low because they are semitransparent. Figure 4.29b shows the absorption spectra for PBDB-T:ITIC active layer on top of glass/ITO/HTL, where HTL are also PEDOT:PSS, F-rGO/PEDOT:PSS or F-rGO. As can be observed in the image, there are not significant differences in absorbance with the use of the different buffer layers. PBDB-T:ITIC active layer spectrum is similar to those reported in the literature [157,158].

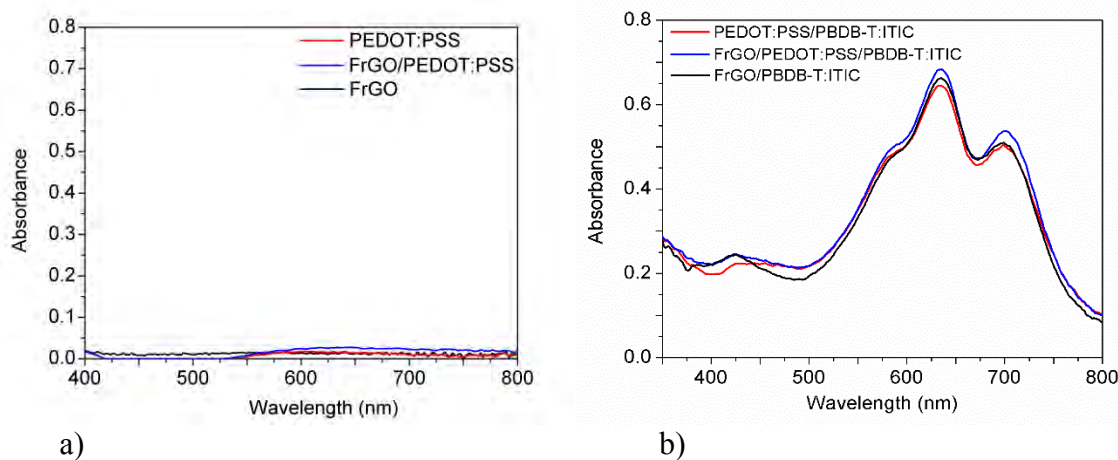


Figure 4.29: UV-Vis absorption spectra of (a) the HTLs used (PEDOT:PSS, F-rGO/PEDOT:PSS and F-rGO) and (b) PBDB-T:ITIC active layer over the different HTLs.

In Figure 4.30 is shown the best J - V curve and achieved efficiency for our fabricated OPVs based on PBDB-T:ITIC (PCE = 8.87 %) upon ethanol solvent treatment. PCE values for these OPVs, under direct configuration and with the use of the alternative FM top electrode vacuum-free deposited [16,38], are comparable with OPVs based on PBDB-T reported in the literature: range 7-11 % [19,103,124,159–162].

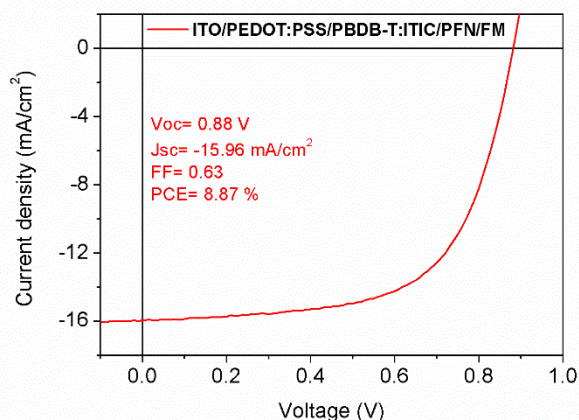


Figure 4.30: Best J - V curve (from series of at least five devices each) and achieved efficiency for PBDB-T:ITIC based OPVs devices using the FM alternative top electrode vacuum-free deposited.

Figure 4.31a and b shows the best J - V and EQE curves of OPV devices with the different HTLs. For the F-rGO/PEDOT:PSS as bilayer, it was expected an improvement in the efficiency because of better energy alignment between F-rGO (WF = 5.1 eV), PEDOT:PSS (WF = 5 eV) and the HOMO level of PBDB-T (WF = 5.2 eV), and also, potentially by an increment in conductivity by the weakening of the coulombic attraction between PEDOT and PSS through the functional groups of F-rGO nanosheets [109], however, a single F-rGO film does not cover homogeneously the ITO surface, as it can be seen from SEM images (Figure 4.32b); yielding a lower efficiency of 8.38% than for a single HTL of PEDOT:PSS (8.87 %). For F-rGO case only, as has been reported [163], it was expected an improvement in PCE due a better-matched WF with the highest occupied molecular orbital level of PBDB-T donor (WF = 5.2 eV), which induces a superior device open-circuit voltage. However, efficiency decays to 5.45% mainly due to a considerable voltage decreases (from 0.87 to 0.74 V), current density also has a decrement (of about 1 mA/cm²) and FF too. Devices with F-rGO as HTL exhibit very poor performance in comparison with PEDOT:PSS as HTL, main reason could be inhomogeneity of F-rGO on the ITO surface, which is in agreement with literature [164], however, it has been reported that F-rGO present significant improvement in the photovoltaic stability [164]. EQE measurements for PEDOT:PSS and F-rGO/PEDOT:PSS based OSCs are also very similar and reached almost 80%; for F-rGO case, EQE was almost 65%, these data in correlation with those from J - V plots. The averaged PV parameters (from series of at least five devices each) for the fabricated OSCs, with different HTL, are shown in Table 4.7 bellow. The best PCEs achieved for each case are shown in parenthesis.

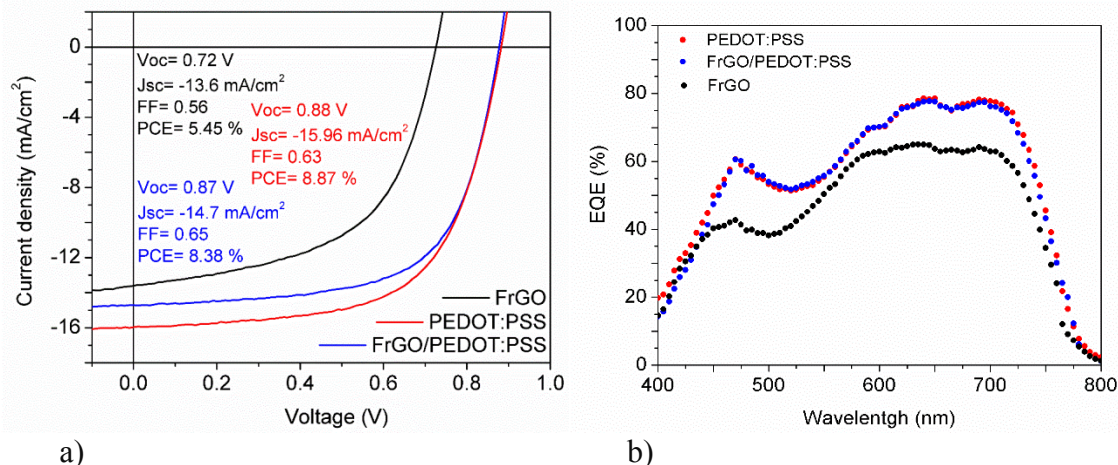
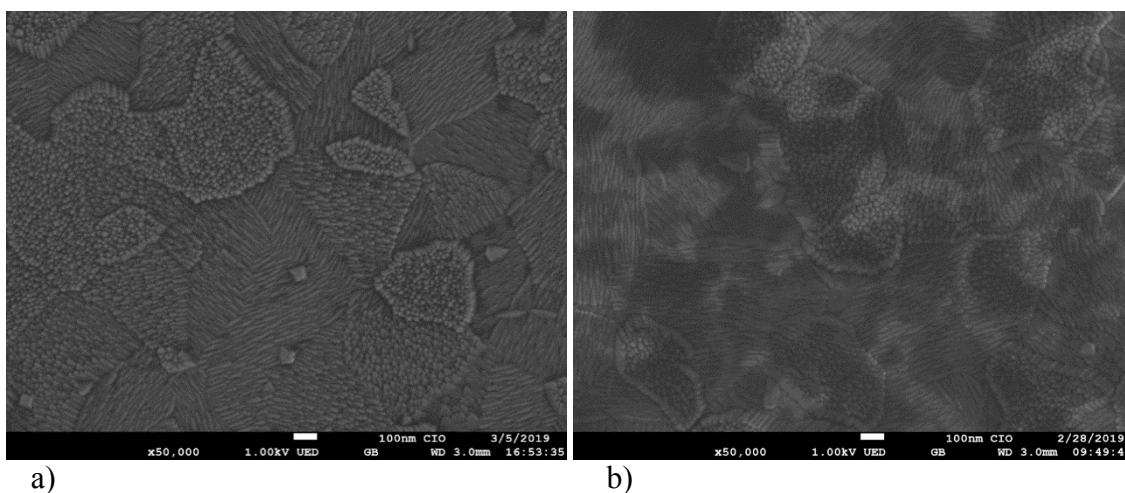


Figure 4.31: (a) Best J - V curves and achieved efficiencies and (b) EQE curves for PBDB-T:ITIC based OPVs devices with the different HTLs (PEDOT:PSS, F-rGO/PEDOT:PSS and F-rGO).

Figure 4.32 from a to d, shows SEM images of ITO, ITO/F-rGO, ITO/PEDOT:PSS and ITO/F-rGO/PEDOT:PSS respectively. It can be noted the typical granular structure of ITO layer in Figure 4.32a. In Figure 4.32b for the F-rGO case, it can be observed that here there is not an homogenous film over ITO (un-covered zones) [16]; also, it can still be observed the ITO structure on the back, and this fact partially is because of the F-rGO film low thickness (between 1 and 4 nm) [165–167]. OPV cells performance is sensitive to F-rGO film thickness due to its electrical insulating characteristics [167,168]. Figure 4.32c and d show the ITO/PEDOT:PSS and ITO/F-rGO/PEDOT:PSS SEM surface, as observed, the PEDOT:PSS layer is a homogenous film (thickness \sim 40 nm) and cover all the ITO or ITO/F-rGO surface.



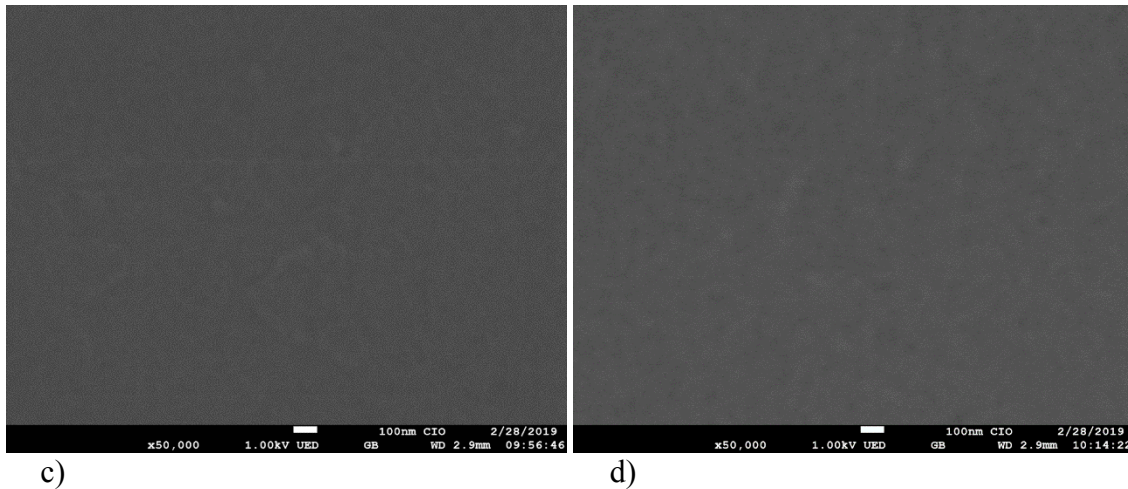
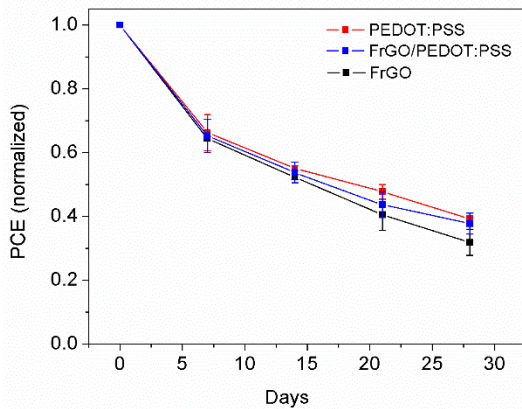


Figure 4.32: SEM images (at 1 kV) of a) ITO, b) ITO/F-rGO, c) ITO/PEDOT:PSS and d) ITO/F-rGO/PEDOT:PSS. Scale bar = 100 nm.

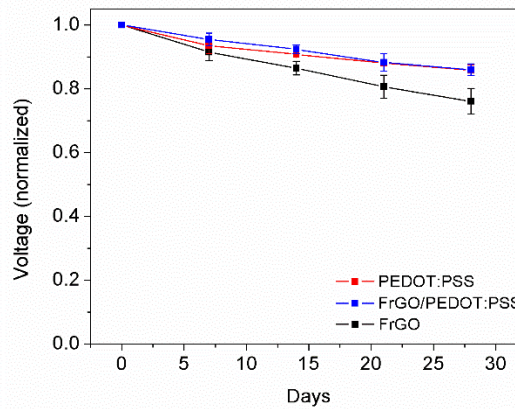
Table 4.7: PV average parameters of the fabricated devices. For PCE, numbers in parenthesis are the best values. OPVs configuration: glass/ITO/HTL/PBDB-T:ITIC/PFN/FM.

HTL	V_{oc} (V)	J_{sc} (mA/cm ²)	FF	PCE (%)
PEDOT:PSS	0.87	14.9	0.63	8.7±0.21 (8.9)
F-rGO/PEDOT:PSS	0.88	14.6	0.64	8.3±0.15 (8.4)
F-rGO	0.74	14	0.53	5.4±0.11 (5.5)

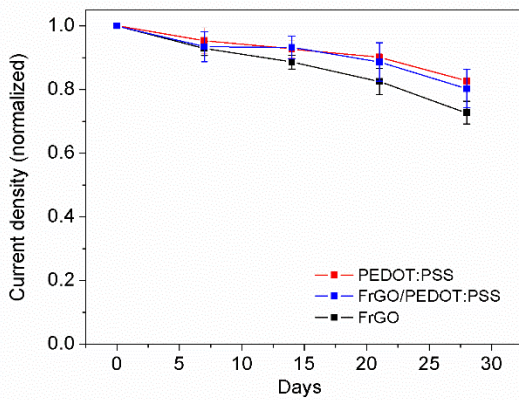
OPVs normalized parameters stability monitoring, under ISOS-D1 testing protocol (dark storage at ambient conditions) [156], are shown in Figure 4.33 from a to d. As can be observed devices with PEDOT:PSS (red) and F-rGO/PEDOT:PSS (blue) as HTLs shows a similar evolution in all of the parameters (PCE, V_{oc} , J_{sc} and FF). For the F-rGO case (black) the voltage and current density, and then the efficiency has a faster decay compared with the other two cases.



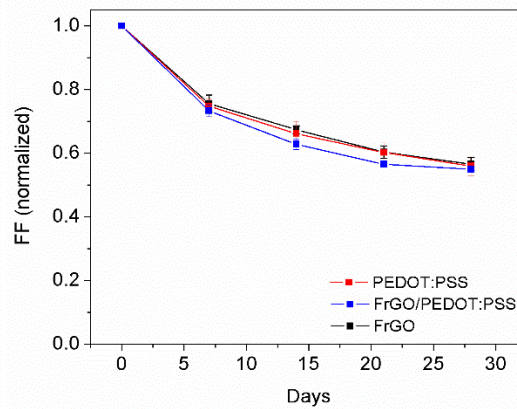
a)



b)



c)



d)

Figure 4.33: Stability of OPVs normalized parameters: (a) power conversion efficiency, (b) voltage, (c) current density and (d) fill factor, for the three HTLs (PEDOT:PSS red, F-rGO/PEDOT:PSS blue and F-rGO black) under ISOS-D1 testing protocol. The average values and error bars were calculated from three devices for each case.

Conclusions of section 4.4

The use of F-rGO as HTL has been investigated in non-fullerene devices with direct configuration: ITO/HTL/PBDB-T:ITIC/PFN/FM. OPVs PEDOT:PSS-based showed an average PCE of 8.7 %, and devices based on F-rGO as HTL exhibited an efficiency of 5.4%. When a bilayer of F-rGO/PEDOT:PSS was used as HTL an average PCE = 8.3% was achieved and this could be due to the fact that a single F-rGO film was deposited and this only film does not cover homogeneously the ITO surface. Moreover, device stability maintain similar with the use of F-rGO/PEDOT:PSS compared with just PEDOT:PSS.

5. Conclusions

In addition to the partial conclusions presented in sections 4.1, 4.2, 4.3 and 4.4, here are presented the general conclusions of this thesis dissertation.

- Donor polymers comparisons indicate that PTB7-Th film chains are somewhat thicker and less spaced, and have a slightly better ordering and higher co-planarity than those for PTB7, providing possible better electrical charge transport. Also, the novel PBDB-T polymer, due to its short distance between chains, could facilitate a more efficient intramolecular charge separation, and thus improve charge transfer from the active layer to the OPV electrodes. Besides, PBDB-T:ITIC uniform fibrillar structure and its larger and less spaced domains could provide homogeneous pathways, helping CC dissociation and transport, and diminishing recombination of exciton CCs. In this work, the best achieved efficiencies with these polymers was 6.89% for PTB7:PC₇₁BM, 7.65% for PTB7-Th:PC₇₁BM, and 8.87% for PBDB-T:ITIC.
- The use of a second electron-acceptor (ternary active layer) is favorable to assist charge dissociation (with cascade-like energy levels between materials), and also to create additional charge-carrier pathways, improving charge transport and collection at the electrodes. Therefore, the use of iron sulfide (FeS₂) nanocrystals at the PTB7:PC₇₁BM active layer helped to enhance solar cell performance at a specific doping level (0.5 wt. %); PCE was 21% improved (average PCE of ~ 6 % (best = 6.47 %)) compared to reference devices (average PCE of ~ 5 % (best = 5.69 %)).
- An active layer thickness variation analysis, with a full characterization regarding EQE and IQE measurements, was made (considering reflection and interference phenomena in the OPV stack through TMM) for the PTB7-Th:PC₇₁BM based OPVs. The estimated IQE spectra showed a significant reduction with the increase in the active layer thickness (> 120 nm), and also when it became too thin (< 75 nm); it is due to losses in recombination and trapping, and to poor absorption, respectively. If an OPV cell exhibits low EQE but high absorption, then the reduction in efficiency arises from either poor transport or poor interfacial kinetics (or both).
- Graphene derivatives, as mentioned before, have several advantages due to their high thermal conductivity, transparency and high electrical charge mobility, characteristics that

could be very well applied in photovoltaic devices. The use of F-rGO as an alternative HTL in PBDB-T:ITIC based OPVs had an average PCE = 8.3% when a bilayer of F-rGO/PEDOT:PSS was used. PEDOT:PSS-based OPVs showed an average PCE of 8.7 %, and devices based on F-rGO exhibited an efficiency of 5.4%. Moreover, device stability, tested under the ISOS-D1 protocol, remained similar with the use of F-rGO/PEDOT:PSS compared with just PEDOT:PSS.

Future work

To complement the studies made in this work, it would be interesting to make TMM analyses with different materials and thicknesses to reach a higher optical electric field inside the active layer, and therefore, achieve better photon absorption and charge generation, increasing OPV efficiency. This is a very helpful method because it allows one to simulate how the device will behave, removing the need to perform many laboratory tests (with the ensuing waste of time, materials, money, and the like), in order to achieve a well-functioning device. Also, ternary active layers are a promising way to achieve higher efficiencies in OPVs. The search for and use of new materials that have the required energetic levels along with a wide absorption spectrum (low bandgap), and that can be mixed, could be very interesting to improve OPV performance. On the other hand, the use of different buffer layers can improve charge transport and collection at the electrodes, and sometimes, also stability. Especially, graphene derivatives can be tested with more than one deposit to diminish the uncovered zones and/or with other thermal treatments; this could improve the homogeneity of the graphene layer, and therefore, the device stability and efficiency. It is important to mention that, within our group, we are acquiring new high-efficiency electron-donors and electron-acceptors to try to increase our PCE record to at least 15% in the near future.

Appendix A

Matlab program to determine Jsc from EQE:

```
% Ruta del archivo
f_ipce='a2.txt';
path_ = 'D:\Trabajo\Doctorado en Ciencias\Tesis\Mediciones\Calcular Jsc\';
ipce=load( [path_ f_ipce], '-ascii' );

% Carga de datos
f_power='potencia.txt';
potencia=load([path_ f_power], '-ascii' );
potencia=potencia(1:5:end);

% Calculo densidad de corriente
Jsc=ipce(:,1).*ipce(:,2).*potencia/1240;
Jsc=trapz(Jsc)*100; %A
Jsc*1000 %mA
```

Matlab program to determine Rs y Rsh using the single diode model:

```
% Cálculo del voltaje térmico Vt a 27°C (300 K)
% Carga del electrón q = 1.6021766208e-19;
% Constante de Boltzmann Kb = 1.38064852e-23 J/K;
n = 1.6;
Vt = n / (1.6021766208e-19 / 1.38064852e-23 / 300);
Iph=13.59e-3;

% Carga los datos
m = xlsread( 'F:\Trabajo\Tesis\Calculo Rs y Rsh\datos100.xls' );
V = m(:,1);
I = m(:,2);

% Elimina los voltajes negativos
% index = find( V < 0, 1, 'last' );
% V = V( index:end );
% I = I( index:end );
% clear( 'index' );

plot( V,I, 'ok' );

% Modelo de ajuste
photocell = @( x,xdata ) ( ...
    x(1) * ( exp( ( V - x(2)*I ) / Vt ) - 1 ) + ...
    ( V - x(2)*I ) / x(3) - Iph );

% Estimación de valores iniciales
hold on;
plot( V, photocell( [ 1e-10, 15,150 ], V ) )
plot( V, I, 'ok' );
hold off;
```

```

% Ajuste de la corriente ideal
[x,~] = lsqcurvefit( ...
    photocell, ... % Función
    [ 0.8e-10, 10,100 ], .... % Valores Iniciales
    V, I, [], [], ...
    optimset( 'Algorithm','levenberg-marquardt' ) );

% Despliega los valores
close all
hold on;
plot( V, I*1000, 'ko' );
plot( V, photocell( x, V )*1000, '-r' );
xlabel('Voltage (V)');
ylabel('J (mA/cm^{2})');
hold off;

fprintf( '\nCorriente de Saturacion (Is): %e\n', x(1) );
%fprintf( ' Fotocorriente Ideal (Iph): %e\n', x(2) );
fprintf( ' Resistencia en Serie (Rs): %f\n', x(2) );
fprintf( 'Resistencia en Paralelo (Rs): %f\n\n', x(3) );

semilogy(V,abs(I));
hold on;
semilogy(V, abs(photocell( x, V )), '-r' );
xlabel('Voltage (V)');
ylabel('J (mA/cm^{2})');
hold off;

```


Scientific publications

- 1- **Olivia Amargós-Reyes**, José-Luis Maldonado, Daniel Romero-Borja, Denisse Barreiro-Argüelles, Irving Caballero-Quintana, Oracio Barbosa-García, Jorge A. Gaspar, “*Organic photovoltaic cell analysis through quantum efficiency and scanning tunneling microscopy of the donor/blend as an active film*”, *J. Mater. Sci.* **54** (3), 2427-2445 (2019), DOI: <https://doi.org/10.1007/s10853-018-2956-2>
- 2- Marwa Chammam, Irving Caballero-Quintana, Denisse Barreiro-Argüelles, **Olivia Amargós-Reyes**, Youssef Aidibi, Brice Kauffmann, Carine Duhayon, José-Luis Maldonado, Gabriel Ramos-Ortíz, Valérie Maraval and Remi Chauvin, “*Expanding the carbo-benzene chemical space for electron-accepting ability trifluorotolyl/ tertio-butyl substitution balance*”, *Helv. Chim. Acta* **02**, e1900049 (2019), DOI: <https://doi.org/10.1002/hlca.201900049>
- 3- **Olivia Amargós-Reyes**, José-Luis Maldonado, Omar Martínez-Alvarez, Ma. Elena Nicho-Díaz, José Santos-Cruz, Juan Nicasio-Collazo, Irving Caballero-Quintana, Concepción Arenas-Arrocena, “*Non-toxic pyrite iron sulfide nanocrystals as second electron acceptor in PTB7:PC₇₁BM based organic photovoltaic cells*”, *Beilstein J. Nanotechnol.* **10**, 2238–2250 (2019), DOI: <https://doi.org/10.3762/bjnano.10.216>
- 4- Irving Caballero-Quintana, Daniel Romero-Borja, José-Luis Maldonado, Juan Nicasio-Collazo, **Olivia Amargós-Reyes**, Antonio Jiménez-González, “*Interfacial Energetic Level Mapping and Nano-ordering of Small Molecule/Fullerene Organic Solar Cells by Scanning Tunneling Microscopy and Spectroscopy*”, *Submitted*.
- 5- Irving Caballero-Quintana†, **Olivia Amargós-Reyes**†, José-Luis Maldonado, Juan Nicasio-Collazo, Daniel Romero-Borja and A. Bousseksou, “*Nanoscale properties and stability of PBDB-T:ITIC based solar cells using fluorinated reduced graphene oxide as hole transport layer*”. *In preparation*.

Acknowledgements in PUBLISHED scientific articles:

- 6- Juan Nicasio-Collazo, José-Luis Maldonado, Julio Salinas-Cruz, Denisse Barreiro-Argüelles†, Irving Caballero-Quintana, Carlos Vázquez-Espinosa, Daniel Romero-Borja, “*Functionalized and reduced graphene oxide as hole transport layer and for use in ternary organic solar cell*”, *Opt. Mater.* **98**, 109434 (2019), DOI: <https://doi.org/10.1016/j.optmat.2019.109434>.

- 7- Irving Caballero-Quintana, José-Luis Maldonado, Marco-Antonio Meneses-Nava, Oracio Barbosa-García, J. Valenzuela-Benavides, A. Bousseksou, “*Semiconducting Polymer Thin Films Used in Organic Solar Cells: A Scanning Tunneling Microscopy Study*”, *Adv. Electron. Mater.* **5**, 1800499 (2018), DOI: <https://doi.org/10.1002/aelm.201800499>.
- 8- Daniel Romero-Borja, José-Luis Maldonado, Oracio Barbosa, Mario Rodríguez, Arxel de León, Salvador Fernández, Enrique Pérez-Gutiérrez, “*Organic solar cells based on graphene derivatives and eutectic alloys vacuum-free deposited as top electrodes*”, *Carbon* **134**, 301-309 (2018), DOI: <https://doi.org/10.1016/j.carbon.2018.03.083>
- 9- Denisse Barreiro-Argüelles, Gabriel Ramos-Ortiz, José-Luis Maldonado, Enrique Pérez-Gutiérrez, Daniel Romero-Borja, Marco-Antonio Meneses-Nava, Jairo C. Nolasco, “*Stability study in organic solar cells based on PTB7:PC₇₁BM and the scaling effect of the active layer*”, *Solar Energy* **163**, 510-518 (2018), DOI: <https://doi.org/10.1016/j.solener.2018.01.090>
- 10- Enrique Pérez-Gutiérrez, Denisse Barreiro-Argüelles, José-Luis Maldonado, Marco-Antonio Meneses-Nava, Oracio Barbosa-García, Gabriel Ramos-Ortiz, Mario Rodríguez, and Canek Fuentes-Hernández, “*Semiconductor Polymer/Top Electrode Interface Generated by Two Deposition Methods and Its Influence on Organic Solar Cell Performance*”, *ACS Appl. Mater. Interfaces* **8** (42), 28763–28770 (2016), DOI: <https://doi.org/10.1021/acsami.6b08970>

References

- [1] Renewable Energy Policy Network for the 21st Century, Highlights of the REN21 Renewables 2018 Global Status Report in perspective, (2018). <http://www.ren21.net/gsr-2018/pages/highlights/highlights/> (accessed May 21, 2019).
- [2] No Title, (n.d.). <http://cienciamx.com/index.php/tecnologia/energia/329-reportaje-con-la-radiacion-solar-que-recibe-el-1-de-sonora-se-podria-generar-energia-suficiente-para-todo-el-pais> (accessed July 19, 2019).
- [3] E. Becquerel, Mémoire sur les effets électriques produits sous l'influence des rayons solaires, *C. R. Acad. Sci.* 9 (1839) 561–567.
- [4] D.-M. Chapin, C.-S. Fuller, G.-L. Pearson, A New Silicon p-n Junction Photocell for Converting Solar Radiation into Electrical Power, *J. Appl. Phys.* 25 (1954) 676–677. doi:10.1063/1.1721711.
- [5] B. Kippelen, J.-L. Brédas, Organic photovoltaics, *Energy Environ. Sci.* 2 (2009) 251–261. doi:10.1039/b812502n.
- [6] C.-W. Tang, Two-layer organic photovoltaic cell, *Appl. Phys. Lett.* 48 (1986) 183–185. doi:10.1063/1.96937.
- [7] A. Khalil, Z. Ahmed, F. Touati, M. Masmoudi, Review on organic solar cells, in: 2016 13th Int. Multi-Conference Syst. Signals Devices, IEEE, (2016) 342–353. doi:10.1109/SSD.2016.7473760.
- [8] I. Benesperi, H. Michaels, M. Freitag, The researcher's guide to solid-state dye-sensitized solar cells, *J. Mater. Chem. C.* 6 (2018) 11903–11942. doi:10.1039/C8TC03542C.
- [9] L. Meng, Y. Zhang, X. Wan, C. Li, X. Zhang, Y. Wang, X. Ke, Z. Xiao, L. Ding, R. Xia, H.-L. Yip, Y. Cao, Y. Chen, Organic and solution-processed tandem solar cells with 17.3% efficiency, *Science* 361 (2018) 1094–1098. doi:10.1126/science.aat2612.
- [10] R. Wang, M. Mujahid, Y. Duan, Z.-K. Wang, J. Xue, Y. Yang, A Review of Perovskites Solar Cell Stability, *Adv. Funct. Mater.* (2019) 1808843 (25 p.). doi:10.1002/adfm.201808843.
- [11] Y. Cui, H. Yao, J. Zhang, T. Zhang, Y. Wang, L. Hong, K. Xian, B. Xu, S. Zhang, J. Peng, Z. Wei, F. Gao, J. Hou, Over 16% efficiency organic photovoltaic cells enabled by a chlorinated acceptor with increased open-circuit voltages, *Nat. Commun.* 10 (2019) 2515 (8 p.). doi:10.1038/s41467-019-10351-5.
- [12] N.R.E. Laboratory, Best Research-Cell Efficiencies, (2018). <https://www.nrel.gov/pv/assets/images/efficiency-chart.png> (accessed November 21, 2019).
- [13] R. Po, A. Bernardi, A. Calabrese, C. Carbonera, G. Corso, A. Pellegrino, From lab to fab:

- How must the polymer solar cell materials design change?-an industrial perspective, *Energy Environ. Sci.* 7 (2014) 925–943. doi:10.1039/c3ee43460e.
- [14] J.-E. Carlé, M. Helgesen, M.-V. Madsen, E. Bundgaard, F.C. Krebs, Upscaling from single cells to modules – fabrication of vacuum- and ITO-free polymer solar cells on flexible substrates with long lifetime, *J. Mater. Chem. C* 2 (2014) 1290–1297. doi:10.1039/C3TC31859A.
- [15] A.-M. Freitas, R.-A.-M. Gomes, R.-A.-M. Ferreira, M.-P. Porto, Experimental performance of commercial OPV panels tested outdoor, *Renew. Energy*. 135 (2019) 1004–1012. doi:10.1016/j.renene.2018.12.051.
- [16] D. Romero-Borja, J.-L. Maldonado, O. Barbosa-García, M. Rodríguez, A. de León, S. Fernández, E. Pérez-Gutiérrez, Organic solar cells based on graphene derivatives and eutectic alloys vacuum-free deposited as top electrodes, *Carbon* 134 (2018) 301–309. doi:10.1016/j.carbon.2018.03.083.
- [17] H. Zhang, H. Yao, J. Hou, J. Zhu, J. Zhang, W. Li, R. Yu, B. Gao, S. Zhang, J. Hou, Over 14% Efficiency in Organic Solar Cells Enabled by Chlorinated Nonfullerene Small-Molecule Acceptors, *Adv. Mater.* 30 (2018) 1800613 (7 p.). doi:10.1002/adma.201800613.
- [18] X. Che, Y. Li, Y. Qu, S.-R. Forrest, High fabrication yield organic tandem photovoltaics combining vacuum- and solution-processed subcells with 15% efficiency, *Nat. Energy*. 3 (2018) 422–427. doi:10.1038/s41560-018-0134-z.
- [19] Q. An, F. Zhang, W. Gao, Q. Sun, M. Zhang, C. Yang, J. Zhang, High-efficiency and air stable fullerene-free ternary organic solar cells, *Nano Energy*. 45 (2018) 177–183. doi:10.1016/j.nanoen.2017.12.050.
- [20] S. Moon, S. Khadtare, M. Wong, S.-H. Han, G.-C. Bazan, H. Choi, Hole transport layer based on conjugated polyelectrolytes for polymer solar cells, *J. Colloid Interface Sci.* 518 (2018) 21–26. doi:10.1016/j.jcis.2018.02.009.
- [21] Q. Guan, R. Peng, Z. Liu, W. Song, R. Yang, L. Hong, T. Lei, X. Fan, Q. Wei, Z. Ge, Highly efficient polymer solar cells employing natural chlorophyllin as a cathode interfacial layer, *J. Mater. Chem. A* 6 (2018) 464–468. doi:10.1039/C7TA09233D.
- [22] H. Kang, G. Kim, J. Kim, S. Kwon, H. Kim, K. Lee, Bulk-Heterojunction Organic Solar Cells: Five Core Technologies for Their Commercialization, *Adv. Mater.* 28 (2016) 7821–7861. doi:10.1002/adma.201601197.
- [23] S.-R. Marder, K.-S. Lee, eds., *Photoresponsive Polymers II*, Springer Berlin Heidelberg, Berlin, Heidelberg, 2008. ISBN: 978-3-540-69454-0.
- [24] H. Hoppe, N.-S. Sariciftci, Organic solar cells: An overview, *J. Mater. Res.* 19 (2004) 1924–1945. doi:10.1557/JMR.2004.0252.
- [25] O. Ostroverkhova, *Organic Optoelectronic Materials: Mechanisms and Applications*, *Chem. Rev.* 116 (2016) 13279–13412. doi:10.1021/acs.chemrev.6b00127.

- [26] W.-C.-H. Choy, *Organic Solar Cells*, Springer London, London, 2013. ISBN: 978-1-4471-4823-4.
- [27] O.-A. Abdulrazzaq, V. Saini, S. Bourdo, E. Dervishi, A.-S. Biris, *Organic Solar Cells: A Review of Materials, Limitations, and Possibilities for Improvement*, Part. Sci. Technol. 31 (2013) 427–442. doi:10.1080/02726351.2013.769470.
- [28] L. Zhao, S. Zhao, Z. Xu, B. Qiao, D. Huang, X. Xu, Two effects of 1,8-diiodooctane on PTB7-Th:PC₇₁BM polymer solar cells, *Org. Electron.* 34 (2016) 188–192. doi:10.1016/j.orgel.2016.04.014.
- [29] O.-M. Awartani, B. Gautam, W. Zhao, R. Younts, J. Hou, K. Gundogdu, H. Ade, Polymer non-fullerene solar cells of vastly different efficiencies for minor side-chain modification: impact of charge transfer, carrier lifetime, morphology and mobility, *J. Mater. Chem. A* 6 (2018) 12484–12492. doi:10.1039/C7TA01746D.
- [30] Z. Wang, Z. Hong, T. Zhuang, G. Chen, H. Sasabe, D. Yokoyama, J. Kido, High fill factor and thermal stability of bilayer organic photovoltaic cells with an inverted structure, *Appl. Phys. Lett.* 106 (2015) 053305 (5 p.). doi:10.1063/1.4907399.
- [31] M.-B. Upama, N.-K. Elumalai, M.-A. Mahmud, M. Wright, D. Wang, C. Xu, A. Uddin, Effect of annealing dependent blend morphology and dielectric properties on the performance and stability of non-fullerene organic solar cells, *Sol. Energy Mater. Sol. Cells.* 176 (2018) 109–118. doi:10.1016/j.solmat.2017.11.027.
- [32] S.-C. Chen, Q. Zheng, Z. Yin, D. Cai, Y. Ma, High performance thermal-treatment-free tandem polymer solar cells with high fill factors, *Org. Electron.* 47 (2017) 79–84. doi:10.1016/j.orgel.2017.05.008.
- [33] G.-A. Nemnes, S. Iftimie, A. Palici, A. Nicolaev, T.-L. Mitran, A. Radu, S. Antohe, Optimization of the structural configuration of ICBA/P3HT photovoltaic cells, *Appl. Surf. Sci.* 424 (2017) 264–268. doi:10.1016/j.apsusc.2017.05.002.
- [34] M.-T. Sajjad, O. Blaszczyk, L.-K. Jagadamma, T.-J. Roland, M. Chowdhury, A. Ruseckas, I.-D.-W. Samuel, Engineered exciton diffusion length enhances device efficiency in small molecule photovoltaics, *J. Mater. Chem. A* 6 (2018) 9445–9450. doi:10.1039/C8TA01226A.
- [35] D.-R. Kozub, K. Vakhshouri, S.-V. Kesava, C. Wang, A. Hexemer, E.-D. Gomez, Direct measurements of exciton diffusion length limitations on organic solar cell performance, *Chem. Commun.* 48 (2012) 5859–5861. doi:10.1039/c2cc31925j.
- [36] B. Kan, Y.-Q.-Q. Yi, X. Wan, H. Feng, X. Ke, Y. Wang, C. Li, Y. Chen, Ternary Organic Solar Cells With 12.8% Efficiency Using Two Nonfullerene Acceptors With Complementary Absorptions, *Adv. Energy Mater.* 8 (2018) 1800424 (7 p.). doi:10.1002/aenm.201800424.
- [37] M. Ikram, R. Murray, M. Imran, S. Ali, S.-I. Shah, Enhanced performance of P3HT/(PCBM:ZnO:TiO₂) blend based hybrid organic solar cells, *Mater. Res. Bull.* 75

- (2016) 35–40. doi:10.1016/j.materresbull.2015.11.031.
- [38] O. Amargós-Reyes, J.-L. Maldonado, D. Romero-Borja, D. Barreiro-Argüelles, I. Caballero-Quintana, O. Barbosa-García, J.-A. Gaspar, Organic photovoltaic cell analysis through quantum efficiency and scanning tunneling microscopy of the donor/blend as an active film, *J. Mater. Sci.* 54 (2019) 2427–2445. doi:10.1007/s10853-018-2956-2.
- [39] B. Collins, Z. Li, J. Tumbleston, E. Gann, Absolute measurement of domain composition and nanoscale size distribution explains performance in PTB7:PC₇₁BM solar cells, *Adv. Energy.* 3 (2013) 65–74. doi:10.1002/aenm.201200377.
- [40] W.-L. Xu, B. Wu, F. Zheng, H.-B. Wang, Y.-Z. Wang, F.-G. Bian, X.-T. Hao, F. Zhu, Homogeneous phase separation in polymer:fullerene bulk heterojunction organic solar cells, *Org. Electron.* 25 (2015) 266–274. doi:10.1016/j.orgel.2015.06.042.
- [41] Y.-J. Kim, A control of structural morphology via introducing insulating polymers in n-type P(NDI2OD-T2) semiconductor, *J. Mater. Sci.* 53 (2018) 10513–10522. doi:10.1007/s10853-018-2300-x.
- [42] Y. Huang, E.-J. Kramer, A.-J. Heeger, G.-C. Bazan, Bulk Heterojunction Solar Cells: Morphology and Performance Relationships, *Chem. Rev.* 114 (2014) 7006–7043. doi:10.1021/cr400353v.
- [43] J.-J. van Franeker, M. Turbiez, W. Li, M.-M. Wienk, R.-A.-J. Janssen, A real-time study of the benefits of co-solvents in polymer solar cell processing, *Nat. Commun.* 6 (2015) 6229 (8 p.). doi:10.1038/ncomms7229.
- [44] A. Hassan, B. Kadem, W. Cranton, Organic solar cells: Study of combined effects of active layer nanostructure and electron and hole transport layers, *Thin Solid Films.* 636 (2017) 760–764. doi:10.1016/j.tsf.2017.04.008.
- [45] R. Ramani, S. Alam, A comparative study on the influence of alkyl thiols on the structural transformations in P3HT/PCBM and P3OT/PCBM blends, *Polymer* 54 (2013) 6785–6792. doi:10.1016/j.polymer.2013.10.023.
- [46] J. Peet, L. Wen, P. Byrne, S. Rodman, K. Forberich, Y. Shao, N. Drolet, R. Gaudiana, G. Dennler, D. Waller, Bulk heterojunction solar cells with thick active layers and high fill factors enabled by a bithiophene-co-thiazolothiazole push-pull copolymer, *Appl. Phys. Lett.* 98 (2011) 043301 (3 p.). doi:10.1063/1.3544940.
- [47] S.-H. Park, A. Roy, S. Beaupré, S. Cho, N. Coates, J.-S. Moon, D. Moses, M. Leclerc, K. Lee, A.-J. Heeger, Bulk heterojunction solar cells with internal quantum efficiency approaching 100%, *Nat. Photonics.* 3 (2009) 297–302. doi:10.1038/nphoton.2009.69.
- [48] A. Pivrikas, H. Neugebauer, N.-S. Sariciftci, Charge Carrier Lifetime and Recombination in Bulk Heterojunction Solar Cells, *IEEE J. Sel. Top. Quantum Electron.* 16 (2010) 1746–1758. doi:10.1109/JSTQE.2010.2044978.
- [49] J.-S. Moon, J. Jo, A.-J. Heeger, Nanomorphology of PCDTBT:PC₇₀BM Bulk Heterojunction Solar Cells, *Adv. Energy Mater.* 2 (2012) 304–308.

doi:10.1002/aenm.201100667.

- [50] H. Park, J. An, J. Song, M. Lee, H. Ahn, M. Jahnel, C. Im, Thickness-dependent internal quantum efficiency of narrow band-gap polymer-based solar cells, *Sol. Energy Mater. Sol. Cells*. 143 (2015) 242–249. doi:10.1016/j.solmat.2015.07.002.
- [51] D.-W. Sievers, V. Shrotriya, Y. Yang, Modeling optical effects and thickness dependent current in polymer bulk-heterojunction solar cells, *J. Appl. Phys.* 100 (2006) 114509 (7 p.). doi:10.1063/1.2388854.
- [52] T. Kobori, T. Fukuda, Effect of optical intensity distribution on device performances of PTB7-Th:PC₇₁BM-based organic photovoltaic cells, *Org. Electron.* 51 (2017) 76–85. doi:10.1016/j.orgel.2017.09.006.
- [53] A. Gusain, R.-M. Faria, P.-B. Miranda, Polymer Solar Cells-Interfacial Processes Related to Performance Issues, *Front. Chem.* 7 (2019) 1-25. doi:10.3389/fchem.2019.00061.
- [54] O.-V. Mikhnenko, P.-W.-M. Blom, T.-Q. Nguyen, Exciton diffusion in organic semiconductors, *Energy Environ. Sci.* 8 (2015) 1867–1888. doi:10.1039/C5EE00925A.
- [55] E.-A. Katz, A. Mescheloff, I. Visoly-Fisher, Y. Galagan, Light intensity dependence of External Quantum Efficiency of fresh and degraded organic photovoltaics, *Sol. Energy Mater. Sol. Cells*. 144 (2016) 273–280. doi:10.1016/j.solmat.2015.09.020.
- [56] C.-M. Proctor, M. Kuik, T.-Q. Nguyen, Charge carrier recombination in organic solar cells, *Prog. Polym. Sci.* 38 (2013) 1941–1960. doi:10.1016/j.progpolymsci.2013.08.008.
- [57] L.-A. Lozano-Hernández, J.-L. Maldonado, C. Garcias-Morales, A. Espinosa Roa, O. Barbosa-García, M. Rodríguez, E. Pérez-Gutiérrez, Efficient OLEDs Fabricated by Solution Process Based on Carbazole and Thienopyrrolediones Derivatives, *Molecules*. 23 (2018) 280 (19 p.). doi:10.3390/molecules23020280.
- [58] F.-C. Krebs, Fabrication and processing of polymer solar cells: A review of printing and coating techniques, *Sol. Energy Mater. Sol. Cells*. 93 (2009) 394–412. doi:10.1016/j.solmat.2008.10.004.
- [59] E. Pérez-Gutiérrez, J. Lozano, J. Gaspar-Tánori, J.-L. Maldonado, B. Gómez, L. López, L.-F. Amores-Tapia, O. Barbosa-García, M.-J. Percino, Organic solar cells all made by blade and slot-die coating techniques, *Sol. Energy*. 146 (2017) 79–84. doi:10.1016/j.solener.2017.02.004.
- [60] D. Barreiro-Argüelles, G. Ramos-Ortiz, J.-L. Maldonado, E. Pérez-Gutiérrez, D. Romero-Borja, M.-A. Meneses-Nava, J.C. Nolasco, Stability study in organic solar cells based on PTB7:PC₇₁BM and the scaling effect of the active layer, *Sol. Energy*. 163 (2018) 510–518. doi:10.1016/j.solener.2018.01.090.
- [61] I. Caballero-Quintana, J.-L. Maldonado, M. Meneses-Nava, O. Barbosa-García, J. Valenzuela-Benavides, A. Bousseksou, Semiconducting Polymer Thin Films Used in Organic Solar Cells: A Scanning Tunneling Microscopy Study, *Adv. Electron. Mater.* (2018) 1800499 (11 p.). doi:10.1002/aelm.201800499.

- [62] L. Markvart, Tom; Castañer, Practical Handbook of Photovoltaics, Elsevier, 2003. ISBN: 978-0-12-385934-1.
- [63] D. Barreiro-Arguelles, G. Ramos-Ortiz, J.-L. Maldonado, E. Perez-Gutierrez, D. Romero-Borja, A. Alvarez-Fernandez, PTB7:PC₇₁BM-Based Solar Cells Fabricated With the Eutectic Alloy Field's Metal as an Alternative Cathode and the Influence of an Electron Extraction Layer, IEEE J. Photovoltaics. 7 (2017) 191–198. doi:10.1109/JPHOTOV.2016.2617087.
- [64] K. Tada, Characteristics of PTB7-Th:C70 bulk heterojunction photocells under low-light illumination: Critical effect of dark parallel resistance, Phys. Status Solidi. 214 (2017) 1700018 (6 p.). doi:10.1002/pssa.201700018.
- [65] W. Mäntele, E. Deniz, UV–VIS absorption spectroscopy: Lambert-Beer reloaded, Spectrochim. Acta Part A Mol. Biomol. Spectrosc. 173 (2017) 965–968. doi:10.1016/j.saa.2016.09.037.
- [66] Nanosurf, (n.d.). <https://www.nanosurf.com/en/how-afm-works> (accessed June 5, 2019).
- [67] G. Binnig, H. Rohrer, Scanning tunneling microscopy, Surf. Sci. 126 (1983) 236–244. doi:10.1016/0039-6028(83)90716-1.
- [68] N.-T.-N. Ha, T.-G. Gopakumar, N.-D.-C. Yen, C. Mende, L. Smykalla, M. Schlesinger, R. Buschbeck, T. Ruffer, H. Lang, M. Mehring, M. Hietschold, Ester formation at the liquid–solid interface, Beilstein J. Nanotechnol. 8 (2017) 2139–2150. doi:10.3762/bjnano.8.213.
- [69] H. Cao, K. Tahara, S. Itano, Y. Tobe, S. De Feyter, Odd–Even Effects in Chiral Phase Transition at the Liquid/Solid Interface, J. Phys. Chem. C. 121 (2017) 10430–10438. doi:10.1021/acs.jpcc.7b02262.
- [70] Nanoscience instruments, (n.d.). <https://www.nanoscience.com/techniques/scanning-electron-microscopy/> (accessed June 5, 2019).
- [71] ATA Scientific, (n.d.). <https://www.atascientific.com.au/microscope-key-differences-sem-optical-microscopy/> (accessed June 5, 2019).
- [72] R. Kohli, Methods for Monitoring and Measuring Cleanliness of Surfaces, in: Dev. Surf. Contam. Clean., Elsevier, 2012: pp. 107–178. ISBN: 978-1-4377-7883-0.
- [73] O. Boltalina, T. Nakajima, New Fluorinated Carbons: Fundamentals and Applications, Elsevier, 2017. ISBN: 978-0-12-803479-8.
- [74] F.-C. Krebs, ed., Stability and Degradation of Organic and Polymer Solar Cells, John Wiley & Sons, Ltd, Chichester, UK, 2012. ISBN: 9781119942436.
- [75] S.-K. Gupta, L.-S. Pali, A. Garg, Impedance spectroscopy on degradation analysis of polymer/fullerene solar cells, Sol. Energy. 178 (2019) 133–141. doi:10.1016/j.solener.2018.12.024.
- [76] G. Teran-Escobar, D.-M. Tanenbaum, E. Voroshazi, M. Hermenau, K. Norrman, M.-T.

- Lloyd, Y. Galagan, B. Zimmermann, M. Hösel, H.-F. Dam, M. Jørgensen, S. Gevorgyan, S. Kudret, W. Maes, L. Lutsen, D. Vanderzande, U. Würfel, R. Andriessen, R. Rösch, H. Hoppe, A. Rivaton, G.-Y. Uzunoğlu, D. Germack, B. Andreasen, M.-V. Madsen, E. Bundgaard, F.-C. Krebs, M. Lira-Cantu, On the stability of a variety of organic photovoltaic devices by IPCE and in situ IPCE analyses – the ISOS-3 inter-laboratory collaboration, *Phys. Chem. Chem. Phys.* 14 (2012) 11824-11845. doi:10.1039/c2cp40821j.
- [77] A. Armin, M. Velusamy, P. Wolfer, Y. Zhang, P.-L. Burn, P. Meredith, A. Pivrikas, Quantum Efficiency of Organic Solar Cells: Electro-Optical Cavity Considerations, *ACS Photonics*. 1 (2014) 173–181. doi:10.1021/ph400044k.
- [78] G. Dennler, K. Forberich, M.-C. Scharber, C.-J. Brabec, I. Tomiš, K. Hingerl, T. Fromherz, Angle dependence of external and internal quantum efficiencies in bulk-heterojunction organic solar cells, *J. Appl. Phys.* 102 (2007) 054516 (8 p.). doi:10.1063/1.2777724.
- [79] G. Palma, L. Cozzarini, E. Capria, A. Fraleoni-Morgera, A home-made system for IPCE measurement of standard and dye-sensitized solar cells, *Rev. Sci. Instrum.* 86 (2015) 013112 (7 p.). doi:10.1063/1.4904875.
- [80] L.-N. Acquaroli, Matrix method for thin film optics, (2018) 1809 (6 p.). doi:arXiv:1809.07708.
- [81] A.-J. Moulé, J.-B. Bonekamp, K. Meerholz, The effect of active layer thickness and composition on the performance of bulk-heterojunction solar cells, *J. Appl. Phys.* 100 (2006) 094503 (8 p.). doi:10.1063/1.2360780.
- [82] L.-H. Slooff, S.-C. Veenstra, J.-M. Kroon, D.-J.-D. Moet, J. Sweelssen, M.-M. Koetse, Determining the internal quantum efficiency of highly efficient polymer solar cells through optical modeling, *Appl. Phys. Lett.* 90 (2007) 143506 (4 p.). doi:10.1063/1.2718488.
- [83] S. Jung, K.-Y. Kim, Y.-I. Lee, J.-H. Youn, H.-T. Moon, J. Jang, J. Kim, Optical Modeling and Analysis of Organic Solar Cells with Coherent Multilayers and Incoherent Glass Substrate Using Generalized Transfer Matrix Method, *Jpn. J. Appl. Phys.* 50 (2011) 122301 (8 p.). doi:10.1143/JJAP.50.122301.
- [84] H.-A. MacLeod, *Thin-Film Optical Filters*, CRC Press, 2001. ISBN: 9781420073027.
- [85] J.-D. Jackson, Electrodynamics, in: *Opt. Encycl.*, Wiley-VCH Verlag GmbH & Co. KGaA, Weinheim, Germany, 2007. doi:10.1002/9783527600441.oe014.
- [86] Refractive index database, (n.d.). doi:<https://refractiveindex.info/?shelf=other&book=In2O3-SnO2&page=Moerland>.
- [87] J.-F. Salinas, H.-L. Yip, C.-C. Chueh, C.-Z. Li, J.-L. Maldonado, A.K.-Y. Jen, Optical Design of Transparent Thin Metal Electrodes to Enhance In-Coupling and Trapping of Light in Flexible Polymer Solar Cells, *Adv. Mater.* 24 (2012) 6362–6367. doi:10.1002/adma.201203099.
- [88] E.-D. Palik, *Handbook of Optical Constants of Solids I*, Academic Press, College Park Maryland, 1985. ISBN: 978-0-08-054721-3.

- [89] E.-D. Palik, Handbook of Optical Constants of Solids II, Academic Press, College Park Maryland, 1991. ISBN: 978-0-12-544422-4.
- [90] G.-J. Hedley, A.-J. Ward, A. Alekseev, C.-T. Howells, E.-R. Martins, L.-A. Serrano, G. Cooke, A. Ruseckas, I.-D.-W. Samuel, Determining the optimum morphology in high-performance polymer-fullerene organic photovoltaic cells, *Nat. Commun.* 4 (2013) 2867 (10 p.). doi:10.1038/ncomms3867.
- [91] J. Huang, J.-H. Carpenter, C.-Z. Li, J.-S. Yu, H. Ade, A.-K.-Y. Jen, Highly Efficient Organic Solar Cells with Improved Vertical Donor-Acceptor Compositional Gradient Via an Inverted Off-Center Spinning Method, *Adv. Mater.* 28 (2016) 967–974. doi:10.1002/adma.201504014.
- [92] R. Fan, Z. Huai, Y. Sun, X. Li, G. Fu, S. Huang, L. Wang, S. Yang, Enhanced performance of polymer solar cells based on PTB7-Th:PC₇₁BM by doping with 1-bromo-4-nitrobenzene, *J. Mater. Chem. C* 5 (2017) 10985–10990. doi:10.1039/C7TC04062H.
- [93] J.-D. Chen, Y.-Q. Li, J. Zhu, Q. Zhang, R.-P. Xu, C. Li, Y.-X. Zhang, J.-S. Huang, X. Zhan, W. You, J.-X. Tang, Polymer Solar Cells with 90% External Quantum Efficiency Featuring an Ideal Light- and Charge-Manipulation Layer, *Adv. Mater.* 30 (2018) 1706083 (8 p.). doi:10.1002/adma.201706083.
- [94] G.-F. Burkhard, E.-T. Hoke, M.-D. McGehee, Accounting for Interference, Scattering, and Electrode Absorption to Make Accurate Internal Quantum Efficiency Measurements in Organic and Other Thin Solar Cells, *Adv. Mater.* 22 (2010) 3293–3297. doi:10.1002/adma.201000883.
- [95] W. Lee, S. Jeong, C. Lee, G. Han, C. Cho, J.-Y. Lee, B.-J. Kim, Self-Organization of Polymer Additive, Poly(2-vinylpyridine) via One-Step Solution Processing to Enhance the Efficiency and Stability of Polymer Solar Cells, *Adv. Energy Mater.* 7 (2017) 1602812 (9 p.). doi:10.1002/aenm.201602812.
- [96] L. Huang, X. Cheng, J. Yang, L. Zhang, W. Zhou, S. Xiao, L. Tan, L. Chen, Y. Chen, High-Performance Polymer Solar Cells Realized by Regulating the Surface Properties of PEDOT:PSS Interlayer from Ionic Liquids, *ACS Appl. Mater. Interfaces* 8 (2016) 27018–27025. doi:10.1021/acsami.6b09078.
- [97] Y. Runnan, Y. Huifeng, H. Jianhui, Recent Progress in Ternary Organic Solar Cells Based on Nonfullerene Acceptors, *Adv. Energy Mater.* (2018) 1702814 (9 p.). doi:10.1002/aenm.201702814.
- [98] H. Lu, X. Xu, Z. Bo, Perspective of a new trend in organic photovoltaic: ternary blend polymer solar cells, *Sci. China Mater.* 59 (2016) 444–458. doi:10.1007/s40843-016-5069-6.
- [99] N. Gasparini, L. Lucera, M. Salvador, M. Prosa, G.-D. Spyropoulos, P. Kubis, H.-J. Egelhaaf, C.-J. Brabec, T. Ameri, High-performance ternary organic solar cells with thick active layer exceeding 11% efficiency, *Energy Environ. Sci.* 10 (2017) 885–892. doi:10.1039/C6EE03599J.

- [100] G. Zhang, K. Zhang, Q. Yin, X.-F. Jiang, Z. Wang, J. Xin, W. Ma, H. Yan, F. Huang, Y. Cao, High-Performance Ternary Organic Solar Cell Enabled by a Thick Active Layer Containing a Liquid Crystalline Small Molecule Donor, *J. Am. Chem. Soc.* 139 (2017) 2387–2395. doi:10.1021/jacs.6b11991.
- [101] P. Cheng, Y. Li, X. Zhan, Efficient ternary blend polymer solar cells with indene-C60 bisadduct as an electron-cascade acceptor, *Energy Environ. Sci.* 7 (2014) 2005–2011. doi:10.1039/c3ee44202k.
- [102] D. Romero-Borja, J.-L. Maldonado, O. Barbosa-García, M. Rodríguez, E. Pérez-Gutiérrez, R. Fuentes-Ramírez, G. de la Rosa, Polymer solar cells based on P3HT:PC₇₁BM doped at different concentrations of isocyanate-treated graphene, *Synth. Met.* 200 (2015) 91–98. doi:10.1016/j.synthmet.2014.12.029.
- [103] B. Wang, Y. Fu, C. Yan, R. Zhang, Q. Yang, Y. Han, Z. Xie, Insight Into the Role of PC₇₁BM on Enhancing the Photovoltaic Performance of Ternary Organic Solar Cells, *Front. Chem.* 6 (2018) 198 (8 p.). doi:10.3389/fchem.2018.00198.
- [104] M.-S. Pereira, F.-A.-S. Lima, T.-S. Ribeiro, M.-R. da Silva, R.-Q. Almeida, E.-B. Barros, I.-F. Vasconcelos, Application of Fe-doped SnO₂ nanoparticles in organic solar cells with enhanced stability, *Opt. Mater.* 64 (2017) 548–556. doi:10.1016/j.optmat.2017.01.023.
- [105] Z. Çaldıran, M. Biber, Ö. Metin, Ş. Aydoğan, Improving the performance of the organic solar cell and the inorganic heterojunction devices using monodisperse Fe₃O₄ nanoparticles, *Optik (Stuttg.)* 142 (2017) 134–143. doi:10.1016/j.ijleo.2017.05.071.
- [106] C. Lin, D. Wang, Y. Wang, C. Chen, Y. Yang, Increased photocurrent in bulk-heterojunction solar cells mediated by FeS₂ nanocrystals, *Sol. Energy Mater.* 95 (2011) 1107–1110. doi:10.1016/j.solmat.2010.12.023.
- [107] M. Alam Khan, Y.-M. Kang, Synthesis and processing of strong light absorbent iron pyrite quantum dots in polymer matrix for efficiency enhancement of bulk-heterojunction solar cell, *Mater. Lett.* 132 (2014) 273–276. doi:10.1016/j.matlet.2014.06.106.
- [108] H. Youn, H.-J. Park, L.-J. Guo, Organic Photovoltaic Cells: From Performance Improvement to Manufacturing Processes, *Small.* 11 (2015) 2228–2246. doi:10.1002/sml.201402883.
- [109] H.-S. Dehsari, E.-K. Shalamzari, J.-N. Gavvani, F.-A. Taromi, S. Ghanbary, Efficient preparation of ultralarge graphene oxide using a PEDOT:PSS/GO composite layer as hole transport layer in polymer-based optoelectronic devices, *RSC Adv.* 4 (2014) 55067–55076. doi:10.1039/C4RA09474C.
- [110] K.-I. Bolotin, K.-J. Sikes, Z. Jiang, M. Klima, G. Fudenberg, J. Hone, P. Kim, H.-L. Stormer, Ultrahigh electron mobility in suspended graphene, *Solid State Commun.* 146 (2008) 351–355. doi:10.1016/j.ssc.2008.02.024.
- [111] T. Mahmoudi, W.-Y. Rho, H.-Y. Yang, S.R.P. Silva, Y.-B. Hahn, Highly conductive and dispersible graphene and its application in P3HT-based solar cells, *Chem. Commun.* 50

- (2014) 8705 (5 p.). doi:10.1039/C4CC03692A.
- [112] F. Bencheikh, D. Duché, C.M. Ruiz, J.-J. Simon, L. Escoubas, Study of Optical Properties and Molecular Aggregation of Conjugated Low Band Gap Copolymers: PTB7 and PTB7-Th, *J. Phys. Chem. C*. 119 (2015) 24643–24648. doi:10.1021/acs.jpcc.5b07803.
- [113] W. Liu, J. Zhang, Z. Zhou, D. Zhang, Y. Zhang, S. Xu, X. Zhu, Design of a New Fused-Ring Electron Acceptor with Excellent Compatibility to Wide-Bandgap Polymer Donors for High-Performance Organic Photovoltaics, *Adv. Mater.* 30 (2018) 1800403 (8 p.). doi:10.1002/adma.201800403.
- [114] S.-H. Liao, H.-J. Jhuo, Y.-S. Cheng, S.-A. Chen, Fullerene Derivative-Doped Zinc Oxide Nanofilm as the Cathode of Inverted Polymer Solar Cells with Low-Bandgap Polymer (PTB7-Th) for High Performance, *Adv. Mater.* 25 (2013) 4766–4771. doi:10.1002/adma.201301476.
- [115] K.-N. Zhang, X.-Y. Yang, M.-S. Niu, Z.-C. Wen, Z.-H. Chen, L. Feng, X.-J. Feng, X.-T. Hao, Modulating the morphology and molecular arrangement via the well-compatible polymer donor in multiple working mechanisms intertwined ternary organic solar cells, *Org. Electron.* 66 (2019) 13–23. doi:10.1016/j.orgel.2018.12.006.
- [116] T. Ye, S. Jin, C. Kang, C. Tian, X. Zhang, C. Zhan, S. Lu, Z. Kan, Comparison Study of Wide Bandgap Polymer (PBDB-T) and Narrow Bandgap Polymer (PBDTTT-EFT) as Donor for Perylene Diimide Based Polymer Solar Cells, *Front. Chem.* 6 (2018) 613 (8 p.). doi:10.3389/fchem.2018.00613.
- [117] Y. Liang, Z. Xu, J. Xia, S.-T. Tsai, Y. Wu, G. Li, C. Ray, L. Yu, For the Bright Future-Bulk Heterojunction Polymer Solar Cells with Power Conversion Efficiency of 7.4%, *Adv. Mater.* 22 (2010) E135–E 138. doi:10.1002/adma.200903528.
- [118] L.-W. Lim, F. Aziz, F.-F. Muhammad, A. Supangat, K. Sulaiman, Electrical properties of Al/PTB7-Th/n-Si metal-polymer-semiconductor Schottky barrier diode, *Synth. Met.* 221 (2016) 169–175. doi:10.1016/j.synthmet.2016.08.018.
- [119] W. Zhao, S. Li, H. Yao, S. Zhang, Y. Zhang, B. Yang, J. Hou, Molecular Optimization Enables over 13% Efficiency in Organic Solar Cells, *J. Am. Chem. Soc.* 139 (2017) 7148–7151. doi:10.1021/jacs.7b02677.
- [120] H.-C. Liao, C.-C. Ho, C.-Y. Chang, M.-H. Jao, S.-B. Darling, W.-F. Su, Additives for morphology control in high-efficiency organic solar cells, *Mater. Today*. 16 (2013) 326–336. doi:10.1016/j.mattod.2013.08.013.
- [121] T. Supasai, V. Amornkitbamrung, C. Thanachayanont, I.-M. Tang, T. Sutthibutpong, N. Rujisamphan, Visualizing nanoscale phase morphology for understanding photovoltaic performance of PTB7:PC₇₁BM solar cell, *Appl. Surf. Sci.* 422 (2017) 509–517. doi:10.1016/j.apsusc.2017.05.205.
- [122] W. Li, B. Guo, C. Chang, X. Guo, M. Zhang, Y. Li, Efficient polymer solar cells based on a copolymer of meta-alkoxy-phenyl-substituted benzodithiophene and thieno[3,4-

- b]thiophene, *J. Mater. Chem. A*. 4 (2016) 10135–10141. doi:10.1039/C6TA04030F.
- [123] B. Tang, J. Liu, X. Cao, Q. Zhao, X. Yu, S. Zheng, Y. Han, Restricting the liquid–liquid phase separation of PTB7-Th:PF12TBT:PC₇₁BM by enhanced PTB7-Th solution aggregation to optimize the interpenetrating network, *RSC Adv.* 7 (2017) 17913–17922. doi:10.1039/C6RA28306C.
- [124] C.-H. Tsai, Y.-A. Su, P.-C. Lin, C.-C. Shih, H.-C. Wu, W.-C. Chen, C.-C. Chueh, High-performance ternary polymer solar cells using wide-bandgap biaxially extended octithiophene-based conjugated polymers, *J. Mater. Chem. C*. 6 (2018) 6920–6928. doi:10.1039/C8TC01542B.
- [125] X. Zhang, Y. Xu, G. Guo, C. Ji, H. Tao, L. Shen, N. Bao, Tuning localized surface plasmon resonances of FeS₂ nanocrystals via shape and surface functional groups for enhanced photoconductivity, *J. Mater. Sci. Mater. Electron.* 28 (2017) 12717–12725. doi:10.1007/s10854-017-7097-x.
- [126] S. Shukla, J.-W. Ager, Q. Xiong, T. Sritharan, Scientific and Technological Assessment of Iron Pyrite for Use in Solar Devices, *Energy Technol.* 6 (2018) 8–20. doi:10.1002/ente.201700638.
- [127] C. Wadia, A.-P. Alivisatos, D.-M. Kammen, Materials Availability Expands the Opportunity for Large-Scale Photovoltaics Deployment, *Environ. Sci. Technol.* 43 (2009) 2072–2077. doi:10.1021/es8019534.
- [128] Y. Bi, Y. Yuan, C. Exstrom, S. Darveau, J. Huang, Air stable, photosensitive, phase pure iron pyrite nanocrystal thin films for photovoltaic application, *Nano Lett.* 11 (2011) 4953–4957. doi:10.1021/nl202902z.
- [129] J. Puthussery, S. Seefeld, N. Berry, M. Gibbs, M. Law, Colloidal iron pyrite (FeS₂) nanocrystal inks for thin-film photovoltaics, *J. Am. Chem. Soc.* 133 (2011) 716–719. doi:10.1021/ja1096368.
- [130] J.-M. Lucas, C.-C. Tuan, S.-D. Lounis, D.-K. Britt, R. Qiao, W. Yang, A. Lanzara, A.-P. Alivisatos, Ligand-Controlled Colloidal Synthesis and Electronic Structure Characterization of Cubic Iron Pyrite (FeS₂) Nanocrystals, *Chem. Mater.* 25 (2013) 1615–1620. doi:10.1021/cm304152b.
- [131] G. Kaur, B. Singh, P. Singh, M. Kaur, K.-K. Buttar, K. Singh, A. Thakur, R. Bala, M. Kumar, A. Kumar, Preferentially grown nanostructured iron disulfide (FeS₂) for removal of industrial pollutants, *RSC Adv.* 6 (2016) 99120–99128. doi:10.1039/C6RA18838A.
- [132] K.-P. Bhandari, P. Koirala, N.-R. Paudel, R.-R. Khanal, A.-B. Phillips, Y. Yan, R.-W. Collins, M.-J. Heben, R.-J. Ellingson, Iron pyrite nanocrystal film serves as a copper-free back contact for polycrystalline CdTe thin film solar cells, *Sol. Energy Mater. Sol. Cells.* 140 (2015) 108–114. doi:10.1016/j.solmat.2015.03.032.
- [133] S. Shukla, N.-H. Loc, P.-P. Boix, T.-M. Koh, R.-R. Prabhakar, H.-K. Mulmudi, J. Zhang, S. Chen, C.-F. Ng, C.-H.-A. Huan, N. Mathews, T. Sritharan, Q. Xiong, Iron Pyrite Thin

- Film Counter Electrodes for Dye-Sensitized Solar Cells: High Efficiency for Iodine and Cobalt Redox Electrolyte Cells, *ACS Nano*. 8 (2014) 10597–10605. doi:10.1021/nn5040982.
- [134] A. Kirkeminde, B.A. Ruzicka, R. Wang, S. Puna, H. Zhao, S. Ren, Synthesis and Optoelectronic Properties of Two-Dimensional FeS₂ Nanoplates, *ACS Appl. Mater. Interfaces*. 4 (2012) 1174–1177. doi:10.1021/am300089f.
- [135] S. Khalid, E. Ahmed, Y. Khan, K.-N. Riaz, M.-A. Malik, Nanocrystalline Pyrite for Photovoltaic Applications, *ChemistrySelect*. 3 (2018) 6488–6524. doi:10.1002/slct.201800405.
- [136] J. Santos-Cruz, R.E. Nuñez-Anita, S.A. Mayén-Hernández, O. Martínez-Alvarez, L.S. Acosta-Torres, J. de la Fuente-Hernández, E. Campos-González, M. Vega-González, M.C. Arenas-Arrocena, Colloidal synthesis of biocompatible iron disulphide nanocrystals, *Artif. Cells Nanomed. Biotechnol.* 46 (2018) 1034–1041. doi:10.1080/21691401.2017.1360321.
- [137] V. Jovanov, N. Yumnam, A. Müller, M. Gruber, V. Wagner, Determining Material-Specific Morphology of Bulk-Heterojunction Organic Solar Cells Using AFM Phase Imaging, *J. Phys. Chem. C*. 121 (2017) 9173–9180. doi:10.1021/acs.jpcc.7b01924.
- [138] S. Middya, A. Layek, A. Dey, P.P. Ray, Synthesis of Nanocrystalline FeS₂ with Increased Band Gap for Solar Energy Harvesting, *J. Mater. Sci. Technol.* 30 (2014) 770–775. doi:10.1016/j.jmst.2014.01.005.
- [139] D. Huang, Y. Li, Z. Xu, S. Zhao, L. Zhao, J. Zhao, Enhanced performance and morphological evolution of PTB7:PC₇₁BM polymer solar cells by using solvent mixtures with different additives, *Phys. Chem. Chem. Phys.* 17 (2015) 8053–8060. doi:10.1039/C4CP05826G.
- [140] A. Wagenpfahl, D. Rauh, M. Binder, C. Deibel, V. Dyakonov, S-shaped current-voltage characteristics of organic solar devices, *Phys. Rev. B*. 82 (2010) 115306 (8 p.). doi:10.1103/PhysRevB.82.115306.
- [141] G. del Pozo, B. Romero, B. Arredondo, Evolution with annealing of solar cell parameters modeling the S-shape of the current–voltage characteristic, *Sol. Energy Mater. Sol. Cells*. 104 (2012) 81–86. doi:10.1016/j.solmat.2012.04.048.
- [142] E. von Hauff, Impedance Spectroscopy for Emerging Photovoltaics, *J. Phys. Chem. C*. 123 (2019) 11329–11346. doi:10.1021/acs.jpcc.9b00892.
- [143] A. Guerrero, N.-F. Montcada, J. Ajuria, I. Etxebarria, R. Pacios, G. Garcia-Belmonte, E. Palomares, Charge carrier transport and contact selectivity limit the operation of PTB7-based organic solar cells of varying active layer thickness, *J. Mater. Chem. A*. 1 (2013) 12345 (10 p.). doi:10.1039/c3ta12358h.
- [144] E. Pérez-Gutiérrez, D. Barreiro-Argüelles, J.-L. Maldonado, M.-A. Meneses-Nava, O. Barbosa-García, G. Ramos-Ortíz, M. Rodríguez, C. Fuentes-Hernández, Semiconductor Polymer/Top Electrode Interface Generated by Two Deposition Methods and Its Influence

- on Organic Solar Cell Performance, *ACS Appl. Mater. Interfaces*. 8 (2016) 28763–28770. doi:10.1021/acsami.6b08970.
- [145] S. Foster, F. Deledalle, A. Mitani, T. Kimura, K.-B. Kim, T. Okachi, T. Kirchartz, J. Oguma, K. Miyake, J.-R. Durrant, S. Doi, J. Nelson, Electron Collection as a Limit to Polymer:PCBM Solar Cell Efficiency: Effect of Blend Microstructure on Carrier Mobility and Device Performance in PTB7:PCBM, *Adv. Energy Mater.* 4 (2014) 1400311 (12 p.). doi:10.1002/aenm.201400311.
- [146] B. Ebenhoch, S.-A.-J. Thomson, K. Genevičius, G. Juška, I.-D.-W. Samuel, Charge carrier mobility of the organic photovoltaic materials PTB7 and PC₇₁BM and its influence on device performance, *Org. Electron.* 22 (2015) 62–68. doi:10.1016/j.orgel.2015.03.013.
- [147] A. El Labban, H. Chen, M. Kirkus, J. Barbe, S. Del Gobbo, M. Neophytou, I. McCulloch, J. Eid, Improved Efficiency in Inverted Perovskite Solar Cells Employing a Novel Diarylamino-Substituted Molecule as PEDOT:PSS Replacement, *Adv. Energy Mater.* 6 (2016) 1502101 (5 p.). doi:10.1002/aenm.201502101.
- [148] J.-S. Yeo, M. Kang, Y.-S. Jung, R. Kang, S.-H. Lee, Y.-J. Heo, S.-H. Jin, D.-Y. Kim, S.-I. Na, In-depth considerations for better polyelectrolytes as interfacial materials in polymer solar cells, *Nano Energy*. 21 (2016) 26–38. doi:10.1016/j.nanoen.2016.01.003.
- [149] H. Azimi, M. Morana, T. Ameri, B. Dastmalchi, M. Scharber, K. Hingerl, C.-J. Brabec, Determining the internal quantum efficiency of organic Bulk Heterojunctions based on mono and bis-adduct fullerenes as acceptor, *Sol. Energy Mater. Sol. Cells*. 95 (2011) 3093–3098. doi:10.1016/j.solmat.2011.06.041.
- [150] F. Liu, W. Zhao, J.-R. Tumbleston, C. Wang, Y. Gu, D. Wang, A.-L. Briseno, H. Ade, T.-P. Russell, Understanding the Morphology of PTB7:PCBM Blends in Organic Photovoltaics, *Adv. Energy Mater.* 4 (2014) 1301377 (9 p.). doi:10.1002/aenm.201301377.
- [151] S. Rafique, S.M. Abdullah, M.M. Shahid, M.O. Ansari, K. Sulaiman, Significantly improved photovoltaic performance in polymer bulk heterojunction solar cells with graphene oxide /PEDOT:PSS double decked hole transport layer, *Sci. Rep.* 7 (2017) 39555 (10 p.). doi:10.1038/srep39555.
- [152] D.-C. Marcano, D.-V. Kosynkin, J.-M. Berlin, A. Sinitskii, Z. Sun, A. Slesarev, L.-B. Alemany, W. Lu, J.M. Tour, Improved Synthesis of Graphene Oxide, *ACS Nano*. 4 (2010) 4806–4814. doi:10.1021/nn1006368.
- [153] P. Ranjan, S. Agrawal, A. Sinha, T.-R. Rao, J. Balakrishnan, A.-D. Thakur, A Low-Cost Non-explosive Synthesis of Graphene Oxide for Scalable Applications, *Sci. Rep.* 8 (2018) 12007 (13 p.). doi:10.1038/s41598-018-30613-4.
- [154] J. Nicasio-Collazo, J.-L. Maldonado, J. Salinas-Cruz, D. Barreiro-Argüelles, I. Caballero-Quintana, C. Vázquez-Espinosa, D. Romero-Borja, Functionalized and reduced graphene oxide as hole transport layer and for use in ternary organic solar cell, *Opt. Mater.* 98 (2019) 109434 (15 p.). doi:10.1016/j.optmat.2019.109434.

- [155] C.K. Chua, M. Pumera, The reduction of graphene oxide with hydrazine: elucidating its reductive capability based on a reaction-model approach, *Chem. Commun.* 52 (2016) 72–75. doi:10.1039/C5CC08170J.
- [156] M.-O. Reese, S.-A. Gevorgyan, M. Jørgensen, E. Bundgaard, S.-R. Kurtz, D.-S. Ginley, D.-C. Olson, M.-T. Lloyd, P. Morvillo, E.-A. Katz, A. Elschner, O. Haillant, T.-R. Currier, V. Shrotriya, M. Hermenau, M. Riede, K.-R. Kirov, G. Trimmel, T. Rath, O. Inganäs, F. Zhang, M. Andersson, K. Tvingstedt, M. Lira-Cantu, D. Laird, C. McGuinness, S. (Jimmy) Gowrisanker, M. Pannone, M. Xiao, J. Hauch, R. Steim, D.-M. DeLongchamp, R. Rösch, H. Hoppe, N. Espinosa, A. Urbina, G. Yaman-Uzunoglu, J.-B. Bonekamp, A.J.J.M. van Breemen, C. Girotto, E. Voroshazi, F.-C. Krebs, Consensus stability testing protocols for organic photovoltaic materials and devices, *Sol. Energy Mater. Sol. Cells.* 95 (2011) 1253–1267. doi:10.1016/j.solmat.2011.01.036.
- [157] Y. Zheng, J. Huang, G. Wang, J. Kong, D. Huang, M. Mohadjer Beromi, N. Hazari, A.D. Taylor, J. Yu, A highly efficient polymer non-fullerene organic solar cell enhanced by introducing a small molecule as a crystallizing-agent, *Mater. Today.* 21 (2018) 79–87. doi:10.1016/j.mattod.2017.10.003.
- [158] W. Liu, W. Li, J. Yao, C. Zhan, Achieving high short-circuit current and fill-factor via increasing quinoidal character on nonfullerene small molecule acceptor, *Chinese Chem. Lett.* 29 (2018) 381–384. doi:10.1016/j.ccllet.2017.11.018.
- [159] S. Xie, Y. Xia, Z. Zheng, X. Zhang, J. Yuan, H. Zhou, Y. Zhang, Effects of Nonradiative Losses at Charge Transfer States and Energetic Disorder on the Open-Circuit Voltage in Nonfullerene Organic Solar Cells, *Adv. Funct. Mater.* 28 (2018) 1705659 (12 p.). doi:10.1002/adfm.201705659.
- [160] M.-B. Upama, M. Wright, N.K. Elumalai, M.-A. Mahmud, D. Wang, C. Xu, A. Uddin, High-Efficiency Semitransparent Organic Solar Cells with Non-Fullerene Acceptor for Window Application, *ACS Photonics.* 4 (2017) 2327–2334. doi:10.1021/acsp Photonics.7b00618.
- [161] X. Liu, B. Xie, C. Duan, Z. Wang, B. Fan, K. Zhang, B. Lin, F.-J.-M. Colberts, W. Ma, R.-A.-J. Janssen, F. Huang, Y. Cao, A high dielectric constant non-fullerene acceptor for efficient bulk-heterojunction organic solar cells, *J. Mater. Chem. A.* 6 (2018) 395–403. doi:10.1039/C7TA10136H.
- [162] E. Park, J. Seo, H. Han, H. Kim, Y. Kim, High-Efficiency Polymer:Nonfullerene Solar Cells with Quaterthiophene-Containing Polyimide Interlayers, *Adv. Sci.* 5 (2018) 1800331 (8 p.). doi:10.1002/advs.201800331.
- [163] X. Cheng, J. Long, R. Wu, L. Huang, L. Tan, L. Chen, Y. Chen, Fluorinated Reduced Graphene Oxide as an Efficient Hole-Transport Layer for Efficient and Stable Polymer Solar Cells, *ACS Omega.* 2 (2017) 2010–2016. doi:10.1021/acsomega.7b00408.
- [164] M. Hilal, J.I. Han, Significant improvement in the photovoltaic stability of bulk heterojunction organic solar cells by the molecular level interaction of graphene oxide with a PEDOT:PSS composite hole transport layer, *Sol. Energy.* 167 (2018) 24–34.

doi:10.1016/j.solener.2018.03.083.

- [165] S.-H. Kim, C.-H. Lee, J.-M. Yun, Y.-J. Noh, S.-S. Kim, S. Lee, S.M. Jo, H.-I. Joh, S.-I. Na, Fluorine-functionalized and simultaneously reduced graphene oxide as a novel hole transporting layer for highly efficient and stable organic photovoltaic cells, *Nanoscale*. 6 (2014) 7183–7187. doi:10.1039/C4NR01038H.
- [166] E. Stratakis, K. Savva, D. Konios, C. Petridis, E. Kymakis, Improving the efficiency of organic photovoltaics by tuning the work function of graphene oxide hole transporting layers, *Nanoscale*. 6 (2014) 6925–6931. doi:10.1039/C4NR01539H.
- [167] Y.-J. Jeon, J.-M. Yun, D.-Y. Kim, S.-I. Na, S.-S. Kim, Moderately reduced graphene oxide as hole transport layer in polymer solar cells via thermal assisted spray process, *Appl. Surf. Sci.* 296 (2014) 140–146. doi:10.1016/j.apsusc.2014.01.061.
- [168] J.-M. Yun, J.-S. Yeo, J. Kim, H.-G. Jeong, D.-Y. Kim, Y.-J. Noh, S.-S. Kim, B.-C. Ku, S.-I. Na, Solution-Processable Reduced Graphene Oxide as a Novel Alternative to PEDOT:PSS Hole Transport Layers for Highly Efficient and Stable Polymer Solar Cells, *Adv. Mater.* 23 (2011) 4923–4928. doi:10.1002/adma.201102207.